Linear Control Model of the Spinal Processing of Descending Neural Signals

by

Iahn Cajigas González

Submitted to the Department of Electrical Engineering and Computer Science
in partial fulfillment of the requirements for the degree of

Master of Engineering in Electrical Engineering and Computer Science

at the

MASSACHUSETTS INSTITUTE OF TECHNOLOGY

September 2003

Author .....
Department of Electrical Engineering and Computer Science
August 28, 2003

Certified by .....
Steve G. Massaquoi
Assistant Professor of Electrical Engineering and Computer Science
Thesis Supervisor

Accepted by .....
Arthur C. Smith
Chairman, Department Committee on Graduate Students

Linear Control Model of the Spinal Processing of Descending Neural Signals

by

Iahn Cajigas González

Submitted to the Department of Electrical Engineering and Computer Science
on August 28, 2003, in partial fulfillment of the
requirements for the degree of
Master of Engineering in Electrical Engineering and Computer Science

Abstract

This thesis develops a physiological-control model of the spinal processing of descending neural kinematic motor control signals in the bullfrog (*Rana Catesbeiana*). The model encompasses the full nonlinear skeletal dynamics of the femur/tibiofibula/tarsus system in the horizontal plane, its muscles, and spinal monosynaptic stretch reflexes. In addition, it incorporates recent findings of muscle synergies encoded within the spinal cord and demonstrates that these muscle synergies can be reorganized into a set of Kinematic Control Synergies (KCS), which have simple, orthogonal kinematic functions. Activating these KCS with simple pulse-like signals allows for the formation of a wide range of behaviors. It is hypothesized that such signals might come from higher-level Central Nervous System (CNS) structures such as the brainstem or cerebellum. Furthermore, KCS present a simple mechanism whereby sensory information could be used by spinal interneurons to recruit the muscle groups required to correct limb movement in real-time, or to learn the correct combination of muscle groups required to perform a movement correctly. Lastly, the experimental findings of convergent, position-invariant ankle force fields observed in the frog are discussed in light of the muscle synergies encoded within the spinal cord and KCS. It is concluded that the control of ankle movement using linear combinations of KCS-derived ankle force fields, may be equivalent to movement control via linear combinations of convergent, position-invariant ankle force fields. Further research, however, is required to concretely establish their equivalence.

Thesis Supervisor: Steve G. Massaquoi
Title: Assistant Professor of Electrical Engineering and Computer Science

Dedicado a mi familia con amor

Dedicated to my family with love

Acknowledgments

As I write this section, I don't think the fact that I have finished my thesis has sunk in yet. It seems as if there is always another section to add/modify/delete or a new figure to make. But there isn't! After almost two years (720 days; 17280 hours; 1,036,800 seconds) since I started to work on this research, it has finally come to an end! Over the course of that time, a great number of family, friends, and colleagues have played very important roles in my life, and to each I am forever indebted. Without even starting to write, I know that the current level of caffeine in my body will not allow me to adequately express (or remember) the countless ways in which so many individuals have helped me over the past years to grow both personally and intellectually, but I will try my best.

First, and foremost, I would like to thank my mother for all of her life's hard work in order to put my sister and I through school. Without her strength, character, and effort, there is no way I would be where I am today. I would also like to thank my father, who passed away before I even learn to walk, for without him I wouldn't be. I would like to thank my grandfather for sharing with me his love for nature and science, and for raising me as if I were his son. Then, there are my sister and my grandmother without whose love and home-cooking, it would have been impossible to make it this far through my higher education. For reasons that would be too numerous to list, I would also like to thank: my aunts, uncles, cousins, niece, and brother-in-law (you know who you are!) for everything they mean to me.

Next is Angela, who deserves an entire paragraph for herself for all the great things that she has brought into my life. Not only was she up all night tonight helping me proofread my thesis, she has actually read it over 5 times! Thank you for always being there for me, for making me smile, and for making my life so complete.

Then, there are all of my friends at MIT who have made my time here so memorable. In particular: Gustavo Santos, Carlos Gomez, Leonardo Villareal, Eric Hsieh, Richard

Prather, Joshua Lapan, Ezra Rosen, Elie Krevat, Rebeca Hwang, Nicole Salazar, Stephen Larson, Siobhan Walsh, Alex Artola, Carlos Armando Garcia, Armando Herrera, Anne Dreyer, Farinaz Edalat, Patrick Freuler, Federico Ardila, and Ian Garcia. Thanks especially to those who kept me company at Athena all of those late nights when I was working on this thesis!

While at MIT there have been a few Professors who have influenced me greatly with their individual teaching styles: Prof. Paul Gray, Prof. Roger Mark, Prof. George Verghese, and Prof. Munther Dahleh. In my mind, their love for engineering, passion for teaching, and extraordinary personalities exemplify the best things of academic life at MIT.

In terms of the research, I cannot even begin to thank Prof. Steve Massaquoi for all of his help, guidance, and patience throughout the course of my collaboration with him. His personal drive and love for his work are so evident they are contageous. I hope that I will have a better chance during the coming years to learn more from such a great teacher. I would also like to thank my officemate, Kazutaka Takahashi, for the numerous conversations we have had regarding my thesis and especially for taking the time to read through one of my numerous drafts. Additionally, I would like to thank Hugh Herr for his help obtaining information on the musculature of the frog hindlimb which was essential for assessing the accuracy my model.

Because most of the background and data for this thesis comes from the work of many individuals at the Bizzi Lab, I am extremely indebted to them for their help. Especially: Emilio Bizzi, Andrea D'Avella, Philippe Saltiel, Charlotte Potak, Vincent Cheung, Matt Tresch, Simon Giszter, Maureen Holden, Timothe Doutriaux, and Robert James Ajemian.

Last, but certainly not least, it would have been impossible to make it through several thesis related "issues" without the help of several Course VI Graduate and Undergraduate Administrative Staff members including: Linda Sullivan, Anne Hunter, Vera Sayzew, Marilyn Pierce, and Peggy Carney.

Iahn Cajigas González

Cambridge, Massachusetts

Thursday, August 28, 2003 - 8:22 am

Contents

List of Figures

List of Tables

Chapter 1

Introduction

Many reasons exist for studying the role of the spinal cord in movement control. First and most importantly, in clinical applications, an accurate model of the spinal processing of descending Central Nervous System (CNS) motor commands may suggest treatments and rehabilitation strategies for patients with spinal cord injury (SCI). Moreover, a functional understanding (both physiological and anatomical) of the spinal cord may help advance the design and engineering of spinal prosthetic devices. That is, with an accurate knowledge of the spinal motor system, spinal prosthesis may be designed to take advantage of the underlying structure of the system - leading to a reduction in device complexity, an improvement of device function, and an increased feasibility for real-time processing of physiological signals. For example, it may become possible to design spinal prosthetic devices that perform the functions of damaged spinal centers externally in a real-time physiological manner, effectively compensating for their damage by restoring lost motor function.

Furthermore, a detailed model of the spinal processing of descending CNS motor control signals may suggest methods whereby kinematic intent information can be inferred from easily accessible physiological signals such as EMGs [1]. These kinematic intent signals could then be used as inputs to neurally driven prothetic limbs

[1] electromyogram (EMG): the tracing of the electrical potentials (voltages) measurable at the skin surface as a result of the electric currents generated within muscles during their contraction.

and other robot motor control systems, which would behave in essentially the same fashion as real limbs from the patient's perspective since they would be controlled physiologically. Finally, an understanding of how the body controls movement will suggest principles for the design of robot motor control systems that are both well suited to be driven by brain-like devices and able to afford flexible, adaptable, and robustly stable environment interactions.

1.1 Overview of Spinal Cord Function

Although within the field of motor control the spinal cord is often thought of as being only a conduit for signals from the periphery of the body to the brain, or vice versa, this simplified interpretation is far from complete. Embedded within the spinal cord are circuits capable of producing a variety of kinematic adjustments and regulatory physiological functions in response to sensory and descending nerve activation. For example, even after having transected the cord below the brain stem, many basic behaviors can still be elicited via intraspinal or cutaneous stimulation. These include:

1. Walking movements;
2. Withdrawal Reflexes (drawing limbs away from painful stimuli);
3. Reflexes that stiffen the legs to support the body against gravity;
4. Reflexes that control local blood vessels and gastrointestinal movement.

The presence of these responses in the absence of higher-level motor structures serves to illustrate the hierarchical structure of the body's neurally controlled motor systems. As illustrated in Figure 1-1, the body's motor systems are organized into three primary levels - spinal cord, brain stem, and primary motor cortex - which are connected both serially and in parallel. Along with the connections present between the primary levels, each level is directly influenced by two independent subcortical systems, the basal ganglia and the cerebellum.

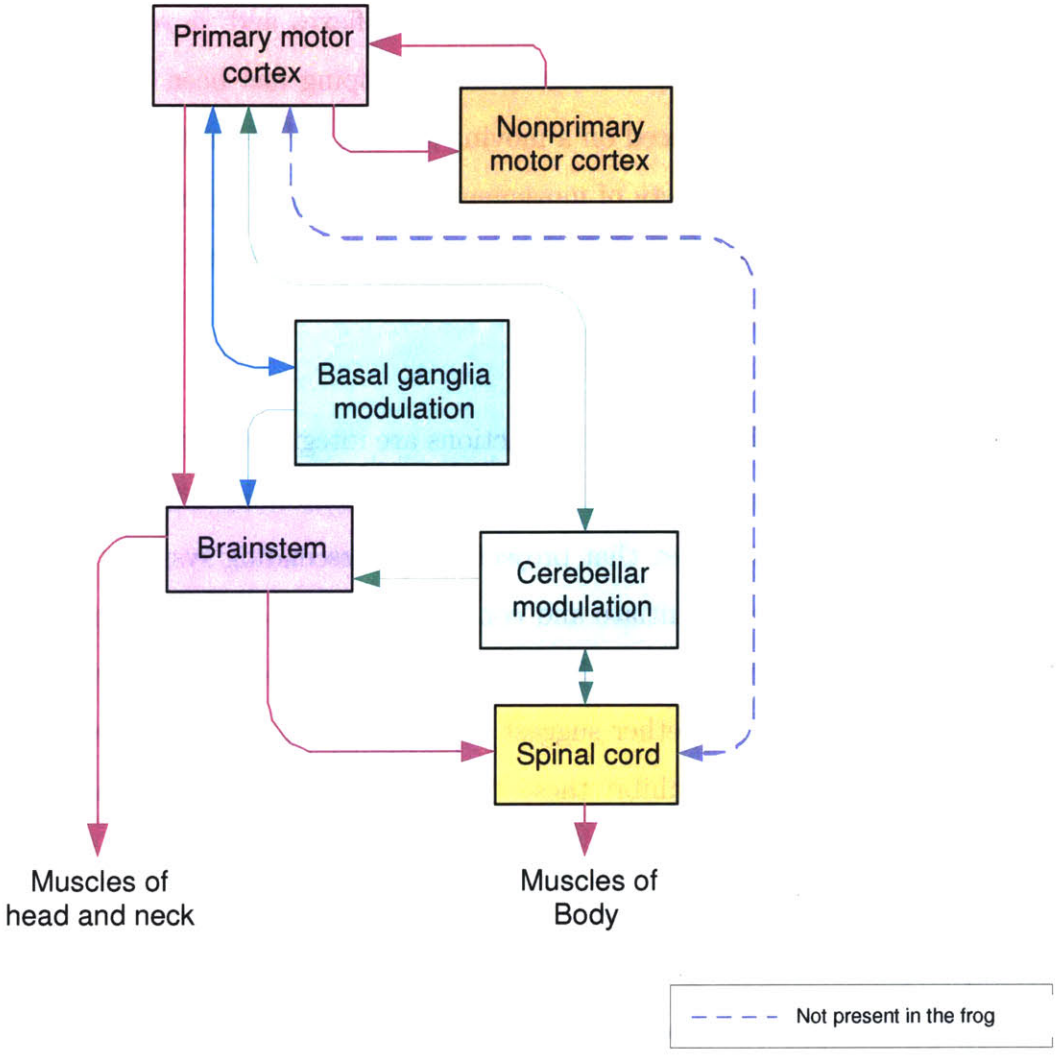

Figure 1-1: Parallel and serial connections between the body's neurally controlled motor systems. Note that the corticospinal tract and the gamma fusimotor system (not shown) are absent in the frog.

In terms of their effects on movement control, primary motor levels can be thought of as providing increasingly higher levels of motor abstraction beginning at the spinal cord and ending with the primary motor cortex. That is, the spinal cord performs many necessary physiological functions and integrates somatosensory information and descending nerve activation as a variety of spinal reflexes and movements. For example, diagonal stepping of all four limbs and galloping has been observed in the spinal cat when its feet are placed on a moving surface [15]. Similarly, the spinalized frog is known to display a variety of movements and complex kinematic adjustments including the rostrocaudal (front to back) wipe and scratch reflex [13] as a result of cutaneous or intraspinal stimulation.

At the level of the brain stem, spinal functions are integrated further into a variety of automated movements that control posture and locomotion. Likewise, several interconnected areas of the cortex that project to the descending systems of the brain stem and to the spinal cord initiate and control our more complex voluntary movements. Such observations illustrate how increasingly complex behaviors are formed by the motor system, and together suggest that one of the roles of descending nerve stimulation is to recruit or inhibit these "prepackaged" motor reflexes during the coordination of movement.

An important observation to be made from Figure 1-1 is that in order for any motor level to achieve direct control of any of the body's muscles (not including the muscles of the head and neck), that level must "go through" the spinal cord. Therefore the types of primitive motor functions encoded within the spinal cord directly influence how supraspinal levels coordinate and execute effective control of the body's muscles and resulting skeletal dynamics. That is to say, in cases where desired movements are realizable as a combination of spinal motor primitives, the corresponding control might be reduced to the sequential recruitment of a small number of spinal functions. However, in the opposite case, supraspinal levels would need to control individual muscles directly to achieve the desired movement.

1.2 Spinal Motor Control in the Frog

In an effort to begin to understand the role of the spinal cord in the control of locomotion, the spinal cord/hindlimb system of the bullfrog (*Rana Catesbeiana*) has been studied extensively. In general, the frog is chosen for the following reasons. First, the frog's spinal cord contains a subset of the full range of circuits present in the mammalian cord. For example, the gamma fusimotor system is completely absent in the frog, as is the corticospinal tract [13] (see Figure 1-1). Second, the frog's behavioral repertoire is much simpler. Therefore, an understanding of the frog's spinal circuits may yield insight into some of the basic circuits within the mammalian cord as well as an explanation for some locomotive implications of several spinal pathologies.

1.2.1 Spinally Encoded Ankle Force Fields

In order to gain insight into the structure and function of spinal circuits, Giszter, Bizzi and colleagues examined the organization of the ranine spinal cord by describing the movements evoked by electrical microstimulation of the spinal cord [13]. In these experiments, microelectrodes were placed in the lateral and intermediate neuropil zone, 500-1000 μm in depth and 200-500 μm from the midline. Stimulation of the spinal gray matter (central part of the cord) with 300 *msec* trains of anodal current impulses resulted in the activation of a set of muscles in the ipsilateral hindlimb. Throughout the experiment, the hindlimb configuration was fully constrained by a pelvis restraint and a force sensor so that no limb motion resulted from microstimulation (*i.e.* muscles were kept in isometric conditions). The isometric force produced by these activated muscles was then measured at the ankle with a force transducer. The resulting ankle forces rose to a plateau level and then declined to a baseline level at a variable period (300 ms to 2 sec) after the termination of stimulation. The ankle was then moved to a new configuration, the same site in the spinal cord was stimulated, and the evoked ankle force measured. As summarized in Figure 1-2, this procedure was repeated for several configurations of the ankle and the resulting

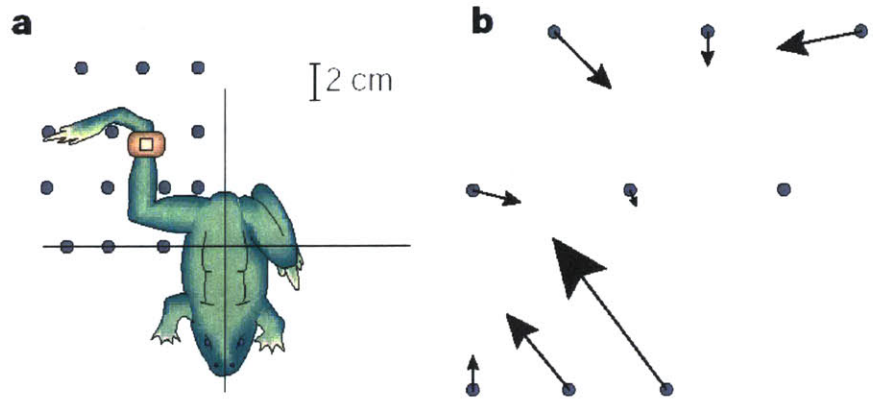

Figure 1-2: Movement characterization by the measurement of isometric force fields. **a)** The ankle of the frog was fixed in different locations of the workspace, indicated by the filled circles. Muscular actions were evoked by electrical stimulation of the spinal cord and the force produced by the pattern of muscle activations was then measured. **b)** The collection of forces measured at different ankle locations. This set of positiondependent forces is termed a force field. (Reprinted with permission from [1])

pattern of position-dependent forces summarized as a force field.

The resulting spatial force fields showed convergence to an equilibrium point, while the equilibrium paths calculated from the force fields with the leg clamped predicted free limb motion in 75% of the trials. These equilibrium paths, known as the limbs' "virtual trajectory", are defined as the trajectory of positions at which the leg would experience no net forces. More significantly, this is also the trajectory of spatial locations toward which the limb endpoint would be attracted at any instant in time if the limb were unconstrained. The observation that free limb movement was predicted by these virtual trajectories in 75% of the trials is, therefore, consistent with the hypothesis of Hogan *et al.* ([19],[20]) that movement of the limbs' equilibrium could be used by the CNS to generate postural transitions and movements. When the force fields were separated into *active* and *pre-stimulation* (passive) components, the active

force field responses showed a fixed position equilibrium. These active force fields were modulated in amplitude over time, although the balance and orientation of forces in the pattern remained fixed. The active fields were further divided into convergent and parallel fields. Convergent force fields (CFFs) were observed in deafferented preparations and found to be similar among different frogs.

It was concluded in this study that the small number of fixed-pattern force fields, $\mathbf{\Phi}_i(x, y)$, elicited from intraspinal stimulation might be viewed as movement primitives. That is, the repertoire of movements performed by the spinalized frog could be reconstructed as simple combinations of these fixed-pattern force fields. Further experiments with intraspinal NMDA iontophoresis [37] [36], cutaneous hindlimb stimulation [42], and supraspinal stimulation [7] have provided further evidence for the existence of movement primitives encoded within the spinal cord.

Subsequent studies by Mussa-Ivaldi *et al.* [24] and Lemay *et al.* [31] found that the simultaneous co-activation of two spinal sites in the frog resulted in a force field equal to the vector sum of the two individual fields. Figure 1-3 illustrates this finding. Two examples of force fields, **a** , **b**, evoked by stimulation of different sites in the spinal cord of a frog are shown. The force field in **c** is that predicted by a simple summation of the force vectors measured at each position in the separate force fields shown in **a** and **b**, while the force field in **d** is that actually produced by costimulation of the two spinal sites illustrated in **a** and **b**. The force field produced by costimulation of two sites in the spinal cord was very similar to the force field predicted by a simple summation of each separate force field (compare **c** and **d**).

More recently, Lemay *et al.* demonstrated in [31] that the magnitude of the individual fields also scaled linearly with activation over the low-force range studied[2]. Taken together these results imply that the active force vector (ankle force field mi-

[2]It should be noted that because the force range studied in [31] was constrained to values less than 20 % of the maximum muscle force, it is possible that this finding does not hold for larger variations of activation.

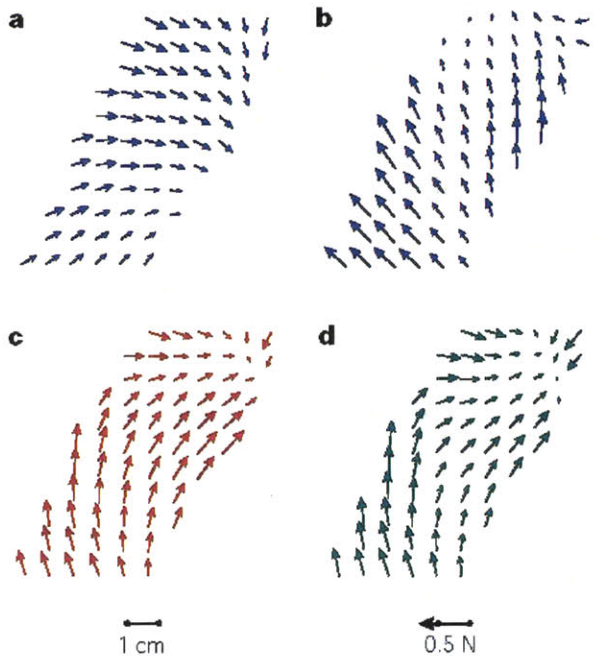

Figure 1-3: Summation of force fields by costimulation of sites in the frog spinal cord. (Reprinted with permission from [1])

nus passive field evaluated at a given workspace location) recorded during a given response, $\mathbf{F}(x, y, t)$, can be written as:

$$\begin{aligned} \mathbf{F}(x,y,t) &= \sum_{i=1}^{N} \mathbf{\Phi}_i(x,y)c_i(t) = \begin{pmatrix} \mathbf{\Phi}_1(x,y) & \dots & \mathbf{\Phi}_N(x,y) \end{pmatrix} \begin{pmatrix} c_1(t) \\ \vdots \\ c_N(t) \end{pmatrix} \\ \mathbf{F}(x,y,t) &= \mathbf{\Phi}(x,y)\mathbf{c}(t) \end{aligned} \tag{1.1}$$

where the pair (x, y) is the cartesian coordinate of the ankle, each $\mathbf{\Phi}_i(x, y)$ is a vector corresponding to the ith primitive force field evaluated at the current ankle location ($\mathbf{\Phi}(x, y)$ is the matrix whose columns are the primitive force fields), and $c_i(t)$ is an amplitude scaling waveform for the ith primitive field. The vector of scaling waveforms, $\mathbf{c}(t)$, has length corresponding to the number of primitive force fields, N. However, it is not yet understood how the spinal stimulation signals, $\mathbf{s}(t)$, are converted into the primitive force field activation signals, $\mathbf{c}(t)$. Additionally, no claim is made in these studies as to how the signal $\mathbf{c}(t)$ is actually generated by the the

nervous system. The number of primitive force fields, N, typically varies from one study to the next but is in general small. Theoretical studies by Mussa-Ivaldi *et al.* [22] [23] have shown that such summation and scaling of a few force field types could be used to generate a large range of force field structures and might underlie movement synthesis.

Kargo and Giszter [27] have confirmed that both force-field summation and scaling occur during real limb behavior by examining the organization of correction responses that circumvent path obstacles during hindlimb wiping trajectories. Correction responses were triggered in real-time during wiping by cutaneous feedback, signaling obstacle collision. The correction response activated a force field that summed with an ongoing sequence of force fields activated during wiping. Both impact force and time of impact within the wiping motor pattern scaled the evoked correction response amplitude. However, the duration of the correction response was constant and similar to the duration of other muscles activated in different phases of wiping. Their results, thus, were consistent with the idea that both force field summation and scaling occur during real limb behavior, that force fields represent fixed-timing motor elements (*i.e.* that force fields can be shifted in time but the timing within the field remains fixed), and that the combination of these motor elements is contingent on the interaction of afferent feedback and central motor programs. The observation of constant duration corrective responses can be understood as an additional constraint on Equation (1.1) where each of the components $\mathbf{c}(t)$ is taken to be of a fixed length of time. The time shifting of the jth primitive force field could be interpreted as a corresponding time-shift of the fields activation waveform,$c_j(t)$ (*i.e.* $c_j(t) \Longrightarrow c_j(t - t_{shift})$.

Lemay *et al.*, in [31], also verified what had been hypothesized by Galagan *et al.* in [12], that the summation of force output is achieved via the summation of the individual drives to muscles (*i.e.* rectified and integrated EMG). EMGs of each muscle at each position were rectified and integrated over time. The rectified and integrated EMGs produced by activation of the individual spinal sites (for each muscle

at each position) were then summed and compared with the rectified integrated EMGs (of each muscle at each position) produced during costimulation of the spinal sites. The average correlation coefficient for the 16 costimulation stimuli pairs studied was 0.87 ± 0.07.

Mathematically, the observation made by Lemay *et al.* can be stated as follows: let $m_i(t)_A$ and $m_i(t)_B$ represent the rectified integrated EMG of muscle i resulting from stimulation of spinal sites A and B respectively. Then, the findings of Lemay *et al.* imply that the rectified integrated EMG of muscle i during costimulation of sites A and B, $m_i(t)_{A+B}$, is

$$m_i(t)_{A+B} = m_i(t)_A + m_i(t)_B \tag{1.2}$$

Or alternatively, written in vector form

$$\mathbf{m}(t)_{A+B} = \begin{pmatrix} m_1(t)_{A+B} \\ \vdots \\ m_n(t)_{A+B} \end{pmatrix} = \begin{pmatrix} m_1(t)_A \\ \vdots \\ m_n(t)_A \end{pmatrix} + \begin{pmatrix} m_1(t)_B \\ \vdots \\ m_n(t)_B \end{pmatrix} = \mathbf{m}(t)_A + \mathbf{m}(t)_B \tag{1.3}$$

where n represents the number of muscles being considered. Note that because of the experimental protocol used in [31], Equation (1.3) holds at each of the workspace locations where the ankle was held fixed.

Given the linearity of ankle force field summation verified by Mussa-Ivaldi *et al.* [24], the observation made by Lemay *et al.* suggests that stereotypic force patterns, or primitives, are likely to be associated with stereotypic EMG patterns. Such a characterization of stereotypic ratios of muscular activations are termed muscle synergies. More importantly, the above observation of EMG summation during costimulation of two spinal sites has an interesting suggestion for how EMG is apparently converted to ankle force by the musculoskeletal system. To see this, let us denote abstractly the functional mapping from EMG to ankle force by $\mathbf{\Gamma} : \mathbf{m}(x, y, t) \longrightarrow \mathbf{F}(x, y, t)$. Then the observed linearity of ankle forces suggests that

$$\begin{aligned} \mathbf{F}_{A+B} &= \mathbf{F}_A + \mathbf{F}_B = \mathbf{\Gamma}(\mathbf{m}_{A+B}) \\ \mathbf{\Gamma}(\mathbf{m}_{A+B}) &= \mathbf{\Gamma}(\mathbf{m}_A) + \mathbf{\Gamma}(\mathbf{m}_B) \\ \mathbf{\Gamma}(\mathbf{m}_A + \mathbf{m}_B) &= \mathbf{\Gamma}(\mathbf{m}_A) + \mathbf{\Gamma}(\mathbf{m}_B) \end{aligned} \tag{1.4}$$

where for notational convenience $\mathbf{F}(x, y, t)$ and $\mathbf{m}(x, y, t)$ have been written as $\mathbf{F}$ and $\mathbf{m}$ respectively. Moreover, Lemay *et al.* demonstrate in [31] that the magnitude of the individual fields also scaled linearly with activation over the low-force range studied. This implies that

$$\mathbf{F}_{cA} = c\mathbf{F}_A \tag{1.5}$$

where c is an arbitrary positive constant, and A is the spinal site being stimulated. Equation (1.5) states that if the activation at a particular spinal site is scaled in amplitude by a factor of c, then the corresponding ankle force also increases by the same factor. If one assumes that EMGs also scale linearly with spinal activation, *i.e.*

$$\mathbf{m}_{cA}(t) = c\mathbf{m}_A(t) \tag{1.6}$$

Equations (1.4) and (1.5) have a very important implication. Here c is the intensity of stimulation at spinal site A. If Equation (1.6) can be shown to be true experimentally, then Equation (1.5) implies that

$$\begin{aligned} \mathbf{F}_{cA} &= \mathbf{\Gamma}(\mathbf{m}_{cA}) \\ \mathbf{\Gamma}(c\mathbf{m}_A) &= c\mathbf{F}_A = c\mathbf{\Gamma}(\mathbf{m}_A) \\ \Longrightarrow \mathbf{\Gamma}(c\mathbf{m}_A) &= c\mathbf{\Gamma}(\mathbf{m}_A) \end{aligned} \tag{1.7}$$

Together Equations (1.4) and (1.7) demonstrate that the mapping relating EMGs and ankle forces must necessarily be linear (in the strict mathematical sense) over the range of activations considered in the experiment by Lemay *et al.*.

This observation can be taken one step further by realizing that at each workspace location the hindlimb joint angles and muscle moment arms were held fixed during

the experiments, and therefore the transformation from muscle forces to ankle forces is also linear, *i.e.*

$$\mathbf{F} = (\mathbf{J}(\mathbf{\Theta}_o)^\top)^{-1}\tau = (\mathbf{J}(\mathbf{\Theta}_o)^\top)^{-1}\mathbf{M}(\mathbf{\Theta}_o)\mathbf{F}^m \tag{1.8}$$

where $\mathbf{F}$ is the force measured at the ankle, $\mathbf{\Theta}_o$ is the vector of joint angles at the current workspace location, $\mathbf{J}(\mathbf{\Theta}_o)$ is the jacobian relating changes in ankle position (x, y) to changes in the joint angles $(\mathbf{\Theta})$, τ is the vector of joint torques, $\mathbf{M}(\mathbf{\Theta}_o)$ is the matrix of muscle moment arms, and $\mathbf{F}^m$ is the vector of muscle forces. Note that both the jacobian and moment arm matrices are evaluated at the current workspace location, so that at each location the transformation $\mathbf{F}^m$ to $\mathbf{F}$ is indeed linear. The effect of Equations (1.4) and (1.8) is that the mapping relating muscle EMGs to muscle force, $\mathbf{\Gamma}'$, must be linear over the range of muscle activations studied in [31]. Given the known nonlinear relation between EMG and muscle force (described in Chapter 2), the linearity constraint on $\mathbf{\Gamma}'$ most likely arises from the low force range used by Lemay *et al.* in their experiments. That is, even though the transformation from EMG to muscle force is actually nonlinear, over small variations of activation it appears substantially linear. However, if Equation (1.6) is found not to hold, then it is possible that spinal networks make the transformation from spinal activations to muscle force appear linear, even though the transformation from EMG to muscle force is nonlinear.

1.2.2 Spinally Encoded Electromyographic Motor Synergies

Recent experiments by Saltiel *et al.* and Tresch *et al.* [36] [42] have sought to identify the existence of muscle synergies encoded within the spinal cord and to quantify the ratios of muscular activation observed within a synergy. In particular, by choosing to define a synergy as a fixed group of muscles whose activity scales together, Saltiel *et al.* attempted to reconstruct observed EMG patterns from 12 hindlimb muscles as linear combinations of synergies. That is to say, in the case of j

muscles and N synergies,

$$\begin{aligned}
\mathbf{m}(t) &= \sum_{i=1}^{N} d_i(t) \begin{pmatrix} w_{1,i} \\ \vdots \\ w_{j,i} \end{pmatrix} = \sum_{i=1}^{N} d_i(t)\mathbf{w}_i \qquad d_i, w_{j,i} \geq 0 \qquad \forall i, j \\
\mathbf{m}(t) &= \begin{pmatrix} \mathbf{w}_1 & \dots & \mathbf{w}_N \end{pmatrix} \begin{pmatrix} d_1(t) \\ \vdots \\ d_N(t) \end{pmatrix} \\
\mathbf{m}(t) &= \mathbf{W}\mathbf{d}(t) \qquad (1.9)
\end{aligned}$$

where $\mathbf{m}(t)$ is the observed EMG vector, $d_i(t)$ is the positive weighting coefficient of the ith muscle synergy, $\mathbf{w}_i$ is the ith muscle synergy, and $w_{j,i} \in [0, 1]$ is the ratio of activation relative to its maximum for muscle j within synergy i. By performing a gradient descent on the error between the reconstructed and actual EMGs recorded in these experiments, Saltiel *et al.* found a set of seven synergies whose linear combinations accounted for more than 90% of the variance of the pooled EMG data. Figure 1-4 illustrates the reconstruction of a sequence of rectified, averaged, and normalized EMGs reconstructed as a linear combination of the seven extracted synergies. The experiments of Tresch *et al.* have a similar experimental paradigm except that cutaneous stimulation was used in order to recruit muscle activations.

Although the above studies elicited EMG responses via two different stimulation methods (intraspinal NMDA [36] and cutaneous stimulation [42]), it is interesting to note that the synergies extracted with both methods were similar but not identical. However, in [41], Tresch *et al.* demonstrated that the responses from spinal stimulation could be well described in terms of the responses from cutaneous stimulation, and vice versa. He also found that the relationship between cutaneous and spinal responses appeared to follow the somatotopy of spinal cutaneous systems, such that the response produced from stimulating a site in the spinal cord tended to be similar to the response produced from stimulating the region of skin surface represented at that site. These results support the idea that responses evoked from electrical microstimulation of the cord and cutaneous stimulation share a similar neural substrate.

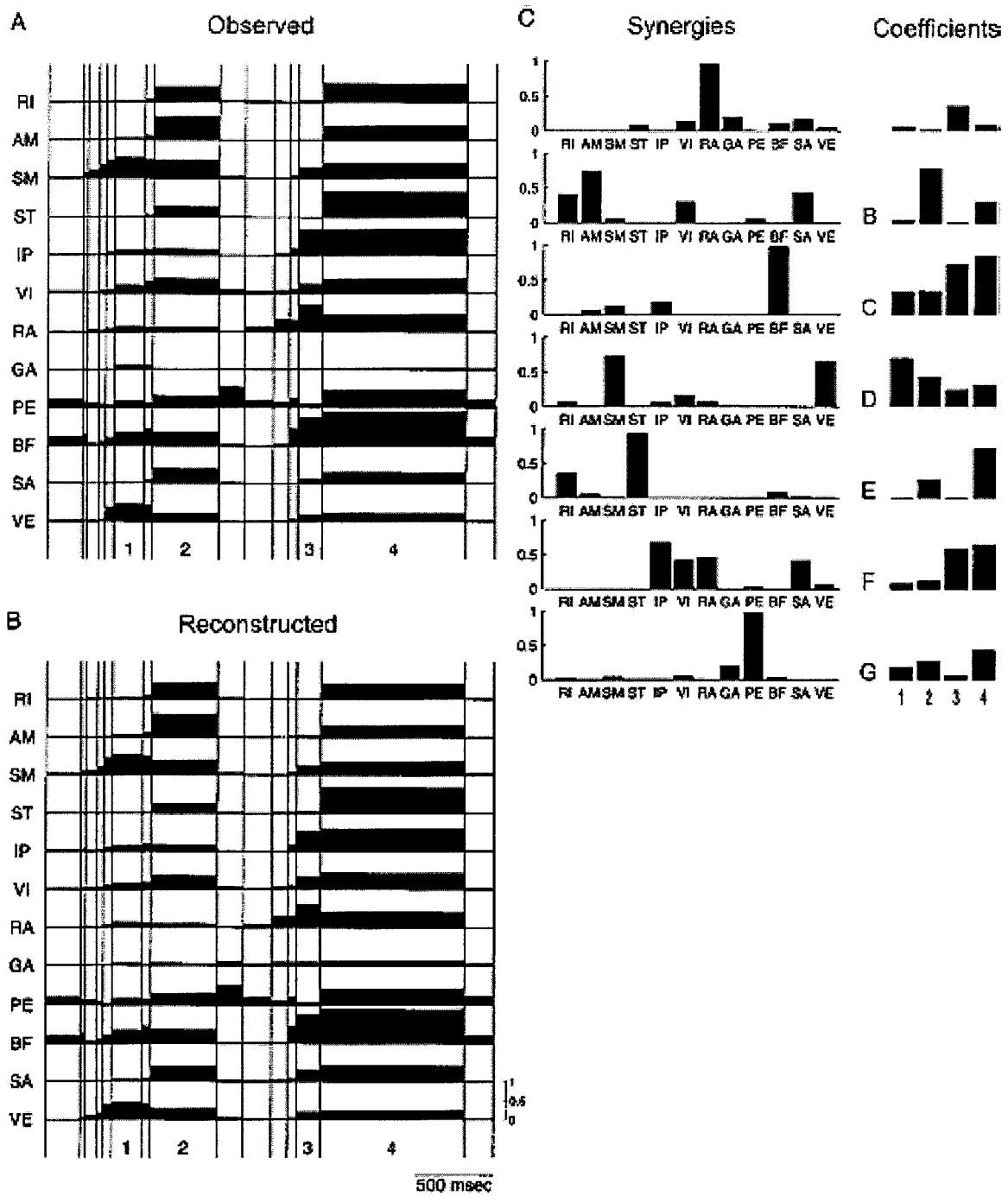

Figure 1-4: EMG sequence elicited via NMDA reconstructed with 7 extracted synergies, $\mathbf{w}_i$, and their coefficients of activation,$d_i(t)$. **A**) EMG sequence rectified, averaged, and normalized ($\mathbf{m}(t)$) for each muscle to its maximum activity observed in that frog. Vertical lines indicate how the sequence was actually parsed. **B**) the same EMG sequence reconstructed. **C**) the 7 synergies utilized in the reconstruction. (Reprinted with permission from [36])

1.2.3 Unification of Primitive Ankle Force Fields and Spinally Encoded Electromyographic Motor Synergies

Given that experiments characterizing both ankle force fields and EMGs arising from intraspinal or cutaneous stimulation found the dimensionality of these to be low, it is natural to ask if there is a direct relation between both Equation (1.1) and (1.9). That is, whether the primitive force fields, $\phi_i(x, y)$, from Equation (1.1) can be described in terms of the observed muscle synergies, $\mathbf{w}_i$, in Equation (1.9). Do muscle synergies encoded within the spinal cord give rise to the small number of force fields observed? To derive the relationship between the two, we begin with Equation (1.8) below.

$$\begin{aligned}
\mathbf{F}(x,y,t) &= (\mathbf{J}(\boldsymbol{\Theta})^{\top})^{-1}\mathbf{M}(\boldsymbol{\Theta})\mathbf{F}^{m} \\
\mathbf{F}(x,y,t) &= (\mathbf{J}(\boldsymbol{\Theta})^{\top})^{-1}\mathbf{M}(\boldsymbol{\Theta})\boldsymbol{\Gamma}'\mathbf{m}(t) \\
\mathbf{F}(x,y,t) &= (\mathbf{J}(\boldsymbol{\Theta})^{\top})^{-1}\mathbf{M}(\boldsymbol{\Theta})\boldsymbol{\Gamma}'\mathbf{W}\mathbf{d}(t) \\
\mathbf{F}(x,y,t) &= (\mathbf{J}(\boldsymbol{\Theta})^{\top})^{-1}\mathbf{M}(\boldsymbol{\Theta})\boldsymbol{\Gamma}'\mathbf{W}\mathbf{Z}(s)\mathbf{c}(t) \\
\mathbf{F}(x,y,t) &= \boldsymbol{\Phi}(x,y)\mathbf{c}(t) \\
\Longrightarrow \boldsymbol{\Phi}(x,y) &= (\mathbf{J}(\boldsymbol{\Theta})^{\top})^{-1}\mathbf{M}(\boldsymbol{\Theta})\boldsymbol{\Gamma}'\mathbf{W}\mathbf{Z}(s) \qquad (1.10)
\end{aligned}$$

where $\boldsymbol{\Phi}(x, y)$ and $\mathbf{c}(t)$ are indeed the same as that in Equation (1.1). The transfer function matrix $\mathbf{Z}(s)$ maps the coefficients, $\mathbf{c}(t)$, from Giszter *et al.* [13] to the coefficients, $\mathbf{d}(t)$, of Saltiel *et al.*. $\mathbf{Z}(s)$ therefore consists of n columns and m rows where n is the number of primitive force fields, $\boldsymbol{\Phi}_i(x, y)$, and m is the number of muscle synergies, $\mathbf{w}_i$. The relationship between $\mathbf{c}(t)$ and $\mathbf{d}(t)$ depends specifically on whether the same number of spinal sites were being activated in both experiments, and on the nature of the spinal circuits that the spinal stimulation recruited in each. Because at this time it is not known how $\mathbf{c}(t)$ and $\mathbf{d}(t)$ are related, we will assume that the number of primitive fields is equal to the number of spinal synergies so that $\mathbf{Z}(s)$ is square. Additionally, for simplicity, it will be assumed that both the force field and synergy experiments stimulated identical neural circuitry so that $\mathbf{Z}(s)$ equals the

identity matrix. Therefore each spinally encoded muscle synergy has a corresponding primitive ankle force field, and the signals $\mathbf{c}(t)$ and $\mathbf{d}(t)$ will be considered equivalent (*i.e.* $\mathbf{c}(t) = \mathbf{d}(t)$).

Note also that in Equation (1.10) the linear mapping relating muscle EMGs to muscle force, $\mathbf{\Gamma}'$, described previously has been represented here by its equivalent matrix. Furthermore, note that $\mathbf{\Gamma}'$ must be diagonal since an EMG $m_i(t)$ only leads to the production of force by muscle i. However, if Equation (1.6) is shown to be false experimentally, $\mathbf{\Gamma}'$ may not necessarily be linear. In this case, the primitive force fields, $\mathbf{\Phi}(x, y)_i$, from Equation (1.1) can still be described in terms of the observed muscle synergies, $\mathbf{w}_i$, as

$$\mathbf{F}(x, y, t) = (\mathbf{J}(\mathbf{\Theta})^\top)^{-1}\mathbf{M}(\mathbf{\Theta})\mathbf{\Gamma}_{exp}(\mathbf{WZ}(s)\mathbf{c}(t)) \tag{1.11}$$

where $\mathbf{\Gamma}_{exp}$ is now the experimentally derived mapping between $\mathbf{m}(x, y, t)$ and $\mathbf{F}(x, y, t)$. Note that $\mathbf{\Gamma}_{exp}$ is now a vector valued function which takes an EMG vector $\mathbf{m}(t) = \mathbf{WZ}(s)\mathbf{c}(t)$ and produces as output the resulting muscle force vector, $\mathbf{F}^m$. Therefore, by either Equation (1.10) or (1.11), the experimentally derived muscle synergies can be transformed into their corresponding force field primitive.

1.3 Toward a Control Engineering Approach to Spinal Cord Motor Control Function

1.3.1 Need for an Integrated Physiological-Control Engineering Model

In order to develop an understanding of how the experimental results outlined above are related to anatomy and physiology of the frog, it is necessary to develop an integrated physiological control model of the spinal/musculoskeletal system (the physiological plant). Through the process of model development, it becomes necessary to explicitly state the anatomical details being modelled along with their intended

physiological function. Once all of the model's components have been implemented and tested to ensure that the model mimics reality in an accurate manner, a number of important hypothesis can be tested.

First, it will become possible to understand how the observed experimental findings arise from the individual anatomical components of the spinal cord and hindlimb. For example, how do the convergent force fields (CFFs) observed by Giszter *et al.* [13] arise from the recruitment of individual muscles? Does activation of the Saltiel *et al.* synergies lead to the production of these CFFs? Do the Saltiel *et al.* synergies capture the entire range of kinematic behaviors that the frog performs? Along with possibly providing answers to these questions, an integrated physiological model may help to demonstrate that certain experimental results are only valid when certain conditions hold, or suggest that the physiology of certain anatomic systems are not well understood. Also, the failure of models to predict observed experimental findings may suggest future experiments that must be carried out in order to gain a better understanding of the spinal/musculoskeletal system.

From a control perspective, an integrated physiological-control engineering model places the physiological system in a precise mathematical framework suitable for system analysis and description in terms of stability, performance, efficiency, and robustness criteria. Moreover, the results of such control engineering analysis can be directly connected to the underlying motor physiology, potentially leading to new insights into motor function and anatomy. Finally, a quantitative model of spinal motor function may suggest treatment and rehabilitation strategies for patients with spinal cord injury, or lead to advances in the design of spinal prosthetics.

1.3.2 Problem Statement

In this thesis, we develop and assess a physiological-control engineering model of the spinal cord/hindlimb system of a frog which includes three skeletal segments, twelve hindlimb muscles, and spinal reflexes. Using the synergy set derived in [36], it

is demonstrated that effective kinematic control of the frog hindlimb can be achieved using linear combinations of the Saltiel *et al.* muscle synergies. Moreover, the relation between muscle synergies and convergent ankle force fields is explored.

Additionally, a new functional reorganization of the Saltiel *et al.* synergies is presented by which muscle synergies are combined to obtain a set of four simple, orthogonal Kinematic Control Synergies (KCS). Using KCS, hindlimb control is reduced to the specification of four independent control signals specifying the azimuthal and radial extent of the hindlimb on the horizontal plane. Surprisingly, even though a 7:4 reduction in dimensionality is achieved, it appears that both the observed kinematics and recorded EMGs from intact bullfrogs during a variety of kicking tasks can be closely reconstructed using only a set of simple pulse-like signals. It is also shown that force fields generated from activation of the Saltiel *et al.* synergies and KCS are convergent. Even with a reduced order muscle model, the KCS force fields show neither a fixed-position equilibrium nor linear scaling with spinal activation. However, if our model is constrained to a small range of ankle forces, then it is consistent with the linearity findings of Mussa-Ivaldi *et al.*. Because the output forces predicted by our model scale as the square of the spinal activations, it behaves linearly over a small range of ankle forces and spinal activations. Our model may also be consistent with Giszter *et al.* in that the KCS force fields, when evaluated at their maximum activation levels, are convergent and show a fixed-position equilibrium.

1.3.3 Thesis Outline

The main work of this thesis can be divided into two logical sections. First, an accurate model of the spinal cord circuits and musculoskeletal components of the frog hindlimb is developed (Chapter 2). Unknown model parameters are obtained via a parameter estimation method (Chapter 3), and the accuracy of the model is assessed (Chapter 4). The performance of the spinal/musculoskeletal model is assessed by testing its ability to reproduce realistic limb kinematics when driven with EMG signals recorded in vivo from intact bullfrogs during kicking tasks. Second, a reorganization

of the synergies identified by Bizzi *et al.* into a set of Kinematic Control Synergies is presented (Chapter 5). The formation of complex behaviors such as swimming and kicking is demonstrated using the developed KCS. Lastly, Chapter 6 concludes with a discussion of some of the implications of this work along with suggestions for future research.

Chapter 2

Spinal-Musculoskeletal Plant Model Structure

In this chapter, we describe the formulation of each of the major components in our bullfrog spinal cord/hindlimb model. First, the skeletal forward dynamic model is described. Then, a brief overview of common muscle model types is presented along with the description of the reduced order muscle model used herein. A summary of spinal cord anatomy follows, illustrating a few of the common cell types and circuits known to be encoded within the spinal cord. Finally, we conclude with a possible hypothesis of how muscle synergies might be encoded within the spinal cord in light of the types of neurons in the cord. Figure 2-1 summarizes the structure of our model.

2.1 Skeletal Forward Dynamic Model

The ranine hindlimb, detailed in Figure 2-2, is a complex skeletal structure, which consists of five major segments: femur, tibiofibula, tarsus (calcaneum and astragalus), metatarsals, and phalanges. However, because the first three segments (femur, tibiofibula, and tarsus) are the longest, most massive, and most heavily actuated by the musculature, the resulting limb dynamics are largely determined by their effects alone. As a result, the frog hindlimb is modelled as a three-link rigid body with the masses and lengths of each link corresponding to those of the femur, tibiofibula,

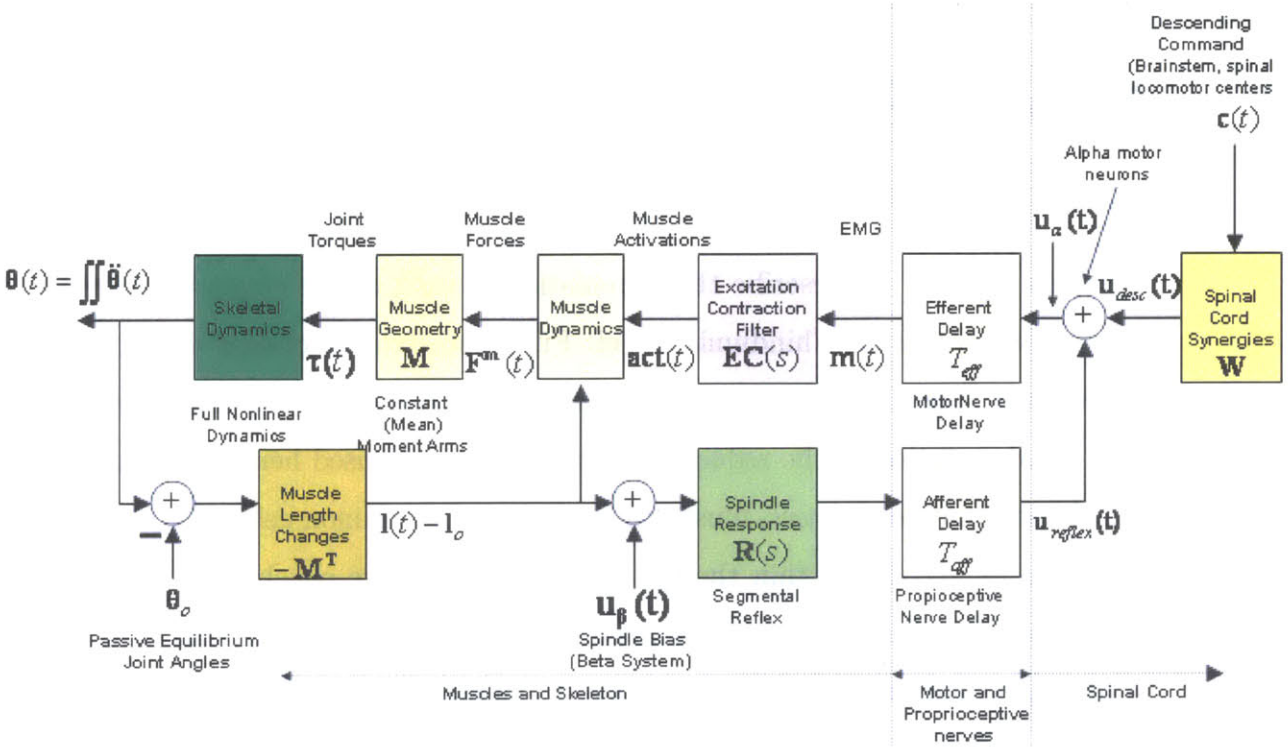

Figure 2-1: Structure of the Spinal Cord/Hindlimb Model

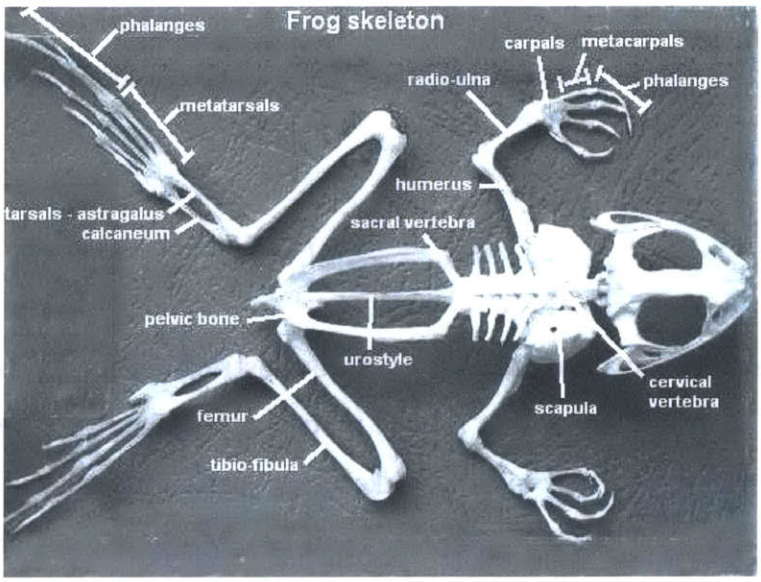

Figure 2-2: Frog Skeleton. Note the contributions of the femur, tibiofibula, and tarsus to the total length and mass of the hindlimb.

Physical Parameters	Femur	Tibiofibula	Tarsus
$mass = m_i\ [grams]$	17.1	12.00	3.40
$length = l_i\ [cm]$	5.48	6.28	3.15
$inertia = I_i\ [grams \cdot cm^2]$	42.9	39.4	2.8

Table 2.1: Physical Parameters for the Three Hindlimb Segments.

and the tarsus respectively. The mass and length values in Table 2.1 were estimated for the bullfrog from values reported in [28] for the *Rana Pipiens*, as described in Appendix A. Segment inertias were computed from the segment masses and lengths using Equation (2.1).

Consistent with previous experimental procedures of Bizzi *et al.* and available kinematic data for the bullfrog, we constrain hindlimb movement to the horizontal plane. Constraining the motion to a plane (not necessarily horizontal) reduces the number of parameters that must be estimated per link from three moments of inertia per segment to one, which is about an axis through the center of mass of each link

and perpendicular to the plane of motion. Therefore, assuming uniform density for each of the links, the moment of inertia of each link, I_i, about its center of mass, becomes

$$I_i = \frac{1}{12} m_i l_i^2 \tag{2.1}$$

While at first it might seem too restrictive to constrain the model solely to motions in the horizontal plane, recall that a large percentage of the frog's behavioral repertoire, such as swimming and kicking, take place predominantly within this plane. To the authors' knowledge, only jumping requires movements that are substantially out of the plane in order to generate the vertical forces necessary to propel the frog upward. Thus, it is our belief that a large part of the frog's kinematic ability can be understood despite this constraint. Furthermore, the equations of motion derived here for the hindlimb hold in any plane. Therefore, if the musculature is able to orient the leg's plane more vertically (by rotating the spherical hip joint to a different pitch angle) and compensate for the effect of gravity, the results shown here should be valid for limb orientations in which the plane of motion has a significant vertical component.

With the model dynamics constrained to a plane, the resulting equations of motion are of straightforward derivation (see Appendix B-1 for the full derivation). One important simplification that arises from our horizontal motion constraint is that the effects of gravity on the rigid body can be neglected, since its effect on each of the segments is uniform and perpendicular to the direction of movement. The resulting dynamic equations of motion can be expressed in matrix form as

$$\tau = \mathbf{H}(\Theta)\ddot{\Theta} + \mathbf{C}(\Theta, \dot{\Theta})\dot{\Theta} \tag{2.2}$$

where τ is the vector of applied joint torques, Θ is the vector of joint angles, $\mathbf{H}(\Theta)$ is the matrix relating angular accelerations to torques (also known as the system inertia matrix), and $\mathbf{C}(\Theta, \dot{\Theta})$ is the matrix consisting of the Coriolis and

centrifugal terms. Terms in the product of the $\mathbf{C}$ matrix and $\dot{\mathbf{\Theta}}$ of the type $\dot{\theta}_i^2$ are called centrifugal, while those involving a product of the type $\dot{\theta}_i\dot{\theta}_j$ where $i \neq j$ are called Coriolis terms. Equation (2.2) can be solved for $\ddot{\mathbf{\Theta}}$ as illustrated in Equation (2.3).

$$\ddot{\mathbf{\Theta}} = \mathbf{H}(\mathbf{\Theta})^{-1}\tau - \mathbf{H}(\mathbf{\Theta})^{-1}\mathbf{C}(\mathbf{\Theta}, \dot{\mathbf{\Theta}})\dot{\mathbf{\Theta}} \tag{2.3}$$

Once in this form, Equation (2.3) can be integrated to obtain the set of joint angle time-waveforms, $\mathbf{\Theta}(t)$, resulting from the applied joint torques, $\tau(t)$.

2.1.1 Endpoint Forces

In order to make our results directly comparable with the force field experiments of Giszter *et al.* [13], Mussa-Ivaldi *et al.* [24], and Lemay *et al.* [31], it is necessary to compute the ankle forces generated by our model. Since the femur-tibia system constrained on the horizontal plane is non-redundant, it is possible to compute the ankle forces, $\mathbf{F}$, generated by an arbitrary set of joint torques, $\tau(t)$. Focusing on ankle force instead of endpoint force results in a square full-rank Jacobian matrix from angular to cartesian ankle coordinates, which can be inverted to obtain the desired ankle forces.

Let us define the 2×2 Jacobian matrix, $\mathbf{J}$, as

$$\mathbf{J} \equiv \frac{\partial \mathbf{x}}{\partial \mathbf{\Theta}} \tag{2.4}$$

where $\mathbf{x}$ is the Cartesian coordinate vector of the ankle, and $\mathbf{\Theta}$ is the vector of joint angles as determined from Equation (2.3). Next, noting that the differential work done on a system must be the same within any coordinate frame, we obtain

$$\mathbf{F}^\top \partial \mathbf{x} = \tau^\top \partial \mathbf{\Theta} \tag{2.5}$$

where $\mathbf{F}$ is the vector of ankle forces, $\mathbf{x}$ is the ankle coordinate vector, τ is the vector of joint torques, and $\mathbf{\Theta}$ is the vector of joint angles. Combining Equations (2.4) and

(2.5) we derive the relation between ankle forces and joint torques, namely that

$$\begin{aligned} \mathbf{F}^\top \mathbf{J} \partial\Theta &= \tau^\top \partial\Theta \\ \mathbf{F}^\top \mathbf{J} &= \tau^\top \\ \mathbf{J}^\top \mathbf{F} &= \tau \\ \mathbf{F} &= (\mathbf{J}^\top)^{-1} \tau \end{aligned} \tag{2.6}$$

Using Equation (2.6) it is possible to reconstruct both the isometric force field at the ankle resulting from any set of joint torques, as well as the real-time ankle forces generated during free limb movement. Chapter 4 contains various examples of these which were used in validating the model.

2.2 Muscle Actuators

In order to maintain consistency between this study and the work of Bizzi *et al.* described in Chapter 1, the twelve muscles listed in Table 2.2 were included. Note that flexion is defined as movement toward the body for both hip and knee, while plantar flexion is defined as movement toward the ground (away from the body). Extension is defined as the complement of flexion in all cases.

2.2.1 Model Types

Three structurally different types of models have evolved over the years to describe muscle-joint systems [45]. The first, based on an input-output analysis of a given task, results in simple second-order differential equation descriptions that are adequate over a certain range of movement. The second, based on the classic structural model of Hill [18], results in highly nonlinear models described by ordinary differential equations. The third, based on analysis of the biophysical contractile mechanism, results in complex partial differential equation descriptions. Of the three, it has been found that an eighth-order Hill-type model is the simplest type of model that adequately

Muscle Name	Abbreviation	Function
Rectus Internus (Gracilis Major)	RI	hip extensor/knee flexor
Adductor Magnus	AM	mono hip extensor
Semimembranous	SM	hip extensor/knee flexor
Semitendinosus	ST	hip extensor/knee flexor
Iliopsoas (Iliacus Internus)	IL	hip flexor
Vastus Internus (Cruralis)	VI	hip flexor/knee extensor
Rectus Anterior (TFL)	RA	hip flexor/knee extensor
Gastrocnemus (Plantarus)	GA	knee flexor/plantar extensor
Peroneus	PE	knee extensor/plantar flexor
Biceps Femoris (Ilio-fibularis)	BF	hip extensor/knee flexor
Sartorius	SA	hip flexor/knee flexor
Vastus Externus (Gluteal)	VE	hip flexor/knee extensor

Table 2.2: Muscle Names, abbreviations, and respective kinematic functions.

simulates most fundamental types of movement without having to modify the model's parameters for different tasks [45] [1].

Hill-type models are typically structured along anatomical lines as connective tissue and contractile tissue. Connective tissue includes both the tendon and aponeurosis. These two tissues have nonlinear spring-like properties that are similar to each other [2], and, therefore, these two anatomically separate tissues are usually grouped into a single component (the series elastic element (SE) in Figure 2-3). The fascicles are classified as contractile tissue. It is generally assumed for simplicity that fibers within a muscle are identical and act together so that a single component (the fascicles)

[1]Interestingly, in spite of the high degree of nonlinearity present at the muscular level, much evidence suggests that entire spinomuscular-joint systems are not as nonlinear as would be expected from the concatenation of several nonlinear elements. Quite to the contrary, recent evidence (as described in Chapter 1) suggests that spinal-musculoskeletal system may behave in a linear fashion from descending neural stimulation in the spinal cord to output muscle force.

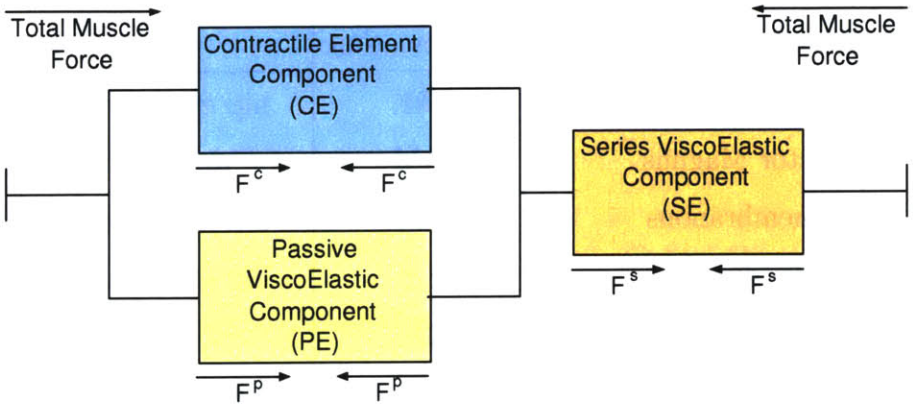

Figure 2-3: Conceptual Model of Muscle Force Production. The tendon and aponeurosis are combined to form the series elastic (SE) components, while the fascicles are composed of the parallel elasticity (PE) and the contractile element (CE).

may be used to represent them. The fascicles themselves can be broken into two smaller mechanical subcomponents: the parallel elastic element (PE) and the active contractile element (CE) (see Figure 2-3). In the passive state (no neural activation) fascicles behave much like a nonlinear spring. This property can be modelled and included as a passive component of the fascicles. When fascicles are neurally activated, they produce (active) force in parallel with and adding to the passive force.

The active contractile component (CE) of muscle force can be divided even further into three smaller subcomponents. The force-length (FL) component arises because of the change in actin/myosin overlap as the length of the fasicles (and hence sarcomeres) changes. As the overlap between the myofilaments changes, the number of cross-bridge sites available for force generation also changes. The force-velocity component (FV) is thought to arise because of cross-bridge dynamics (Huxley [21]). As muscles change length, cross-bridges complete their cycles, detach and reattach. The dynamics of attachment and detachment thus affect the shape of the FV relationship. The activation component (*act*) is associated with calcium kinetics. The variable *act* represents the percentage of myosin binding sites on the thin filament that are available for cross-bridge formation, which depends upon sarcoplasmic cal-

cium concentration. Thus, *act* consists of a function of time that relates motoneuron activity to calcium release and reuptake by the sarcoplasmic reticulum as well as sarcoplasmic calcium concentrations to myosin binding site availability [44](p. 152-153). Equation (2.7), modified from [5], shows the typical form of a Hill-type model, while Figure 2-4 graphically summarizes Equation (2.7).

$$\begin{aligned} F^{pe}(l, act) &= F^{pe1}(l) + F^{pe2}(l)act \\ F^{ce}(l, \dot{l}, act) &= FL(l)FV(v = \dot{l}, l)act \\ F^{m}(l, \dot{l}, act) &= F^{pe}(l, act) + F^{ce}(l, \dot{l}, act) \end{aligned} \tag{2.7}$$

where F^m is the total muscle force, l is the total length of the muscle, $v = \dot{l}$ is the muscle lengthing/shortening velocity, and *act* is the level of neuromuscular activation. Here, along with the components outlined above, the passive elasticity has been further divided into two components. F^{pe1} represents the elastic recoil due to stretching of connective tissue between muscle fibers, while F^{pe2} represents the elastic resistance due to the compression of thick filaments within muscle fibers during active muscle shortening below a certain length.

2.2.2 Reduced Order Muscle Model

Motivated by the fact that extending the Hill model to the total muscle-joint systems immediately creates fairly high-order models [45], a quasi-linear approximation to the full Hill-type model is used for our simulations. The model presented here is similar to the Kelvin-Voight model used by Katayama and Kawato in [30]. One aspect of the model presented here worth pointing out before presenting all of its details is that the series element (SE) is not included. This simplifying assumption is in part justified by the relatively high stiffness (typically 10:1 SE:(PE+CE) stiffness ratio) of the the tendons and aponeuroses when compared to the passive element (PE) and contractile element (CE) stiffness (so that the SE effectively does not change length much as the total muscle length changes). As a result of this assumption, the developed muscle force can be separated into just two components corresponding

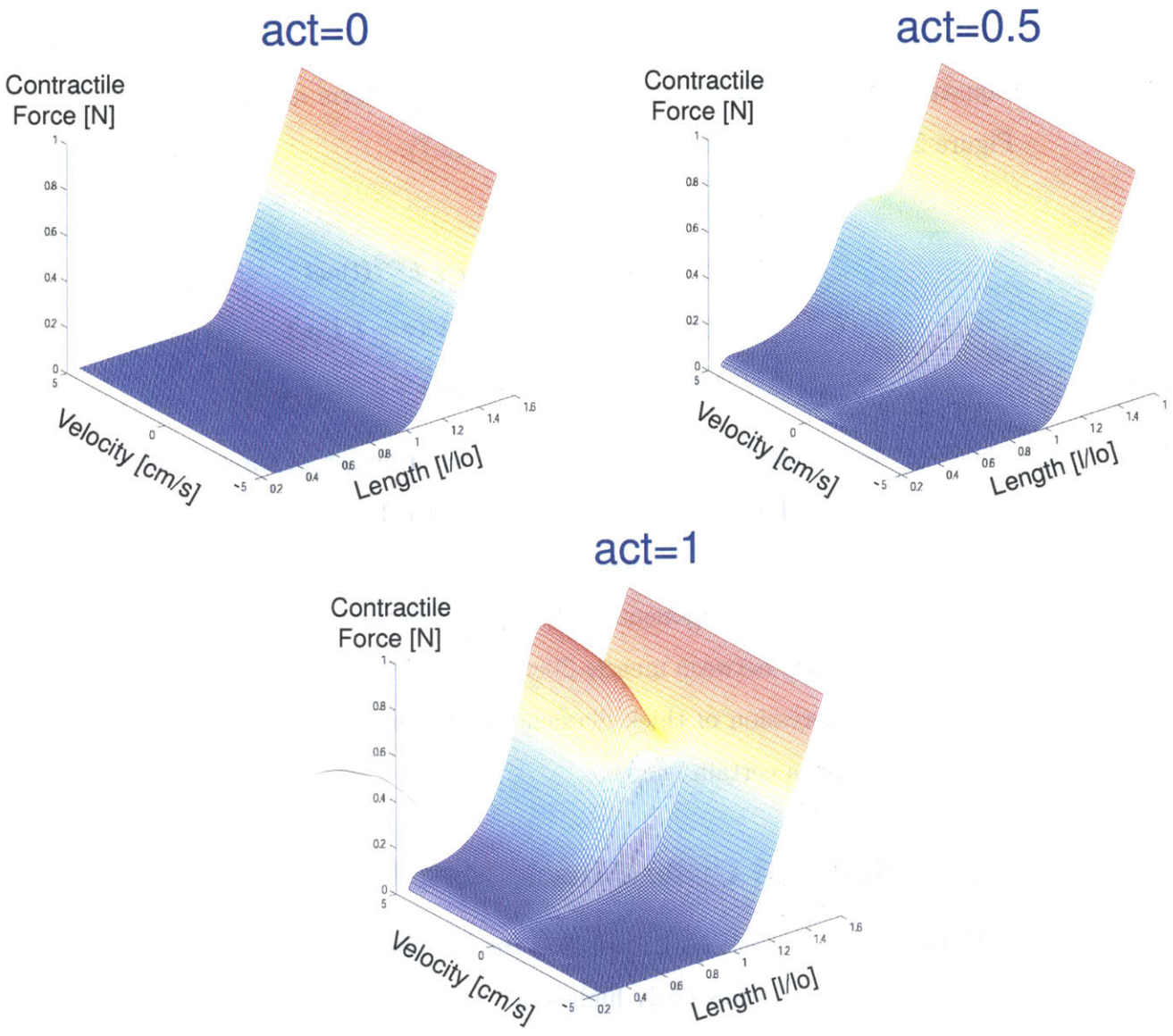

Figure 2-4: Hill-based muscle model Force-Length-Velocity Curve. The three images demonstrate the effects of increased neuromuscular activation on the output muscle force. Model parameter values were obtained from [5]. Note that muscle contractile force (*i.e.* the force that leads to a reduction of muscle length) is defined as being positive.

to PE and CE. Throughout the following section, forces in the direction of muscle contraction will be defined as positive and will be referred to as muscle contractile force.

The passive element force, $F^{pe}(l, \dot{l})$, is represented as arising from an elastic element and a viscous element arranged in parallel, *i.e.*

$$F^{pe}(l, \dot{l}) = K_{pe}(l - l_o) + B_{pv}\dot{l}_i \tag{2.8}$$

where l is the length of muscle, l_o is the rest length of the muscle (defined as the length of the muscle at passive equilibrium $\mathbf{\Theta}_o$), K_{pe} is the linear passive stiffness, and B_{pv} is the linear passive viscosity of the muscle. Thus the passive element is modelled to behave as a linear viscoelastic actuator around the limbs passive equilibrium, defined by l_o.

The change in muscle viscoelasticity together with the increasing output muscle tension resulting from an increase in neural activation (attributed to CE) are modelled by Equation (2.9).

$$F^{ce}(act, l, \dot{l}) = K_{ce}act\lfloor C_{atl}act - (l_o - l)\rfloor_+ + B_{cv}act\lfloor \dot{l} \rfloor_+ \tag{2.9}$$

where $\lfloor arg \rfloor_+ = max(arg, 0)$. Here K_{ce} is a linear contractile element stiffness, C_{atl} is a unit conversion constant relating neuromuscular activation to muscle length with units of millimeters per unit activation, and $act \in [0, 1]$ is the level of neuromuscular activation. Variables l and l_o are the same as those in Equation (2.8). Note that the contractile element is only actively viscous when the muscle is lengthening. This property is derived from the FV relation in the Hill model (see Figure 2-4). In addition, as a result of neglecting the series elastic element, the lengths of the contractile and parallel elastic elements are assumed to be the same and equal to the total length of the muscle, l.

The total muscle force generated, similarly to Equation (2.7), is given by the sum of the passive and contractile element force components, *i.e.*

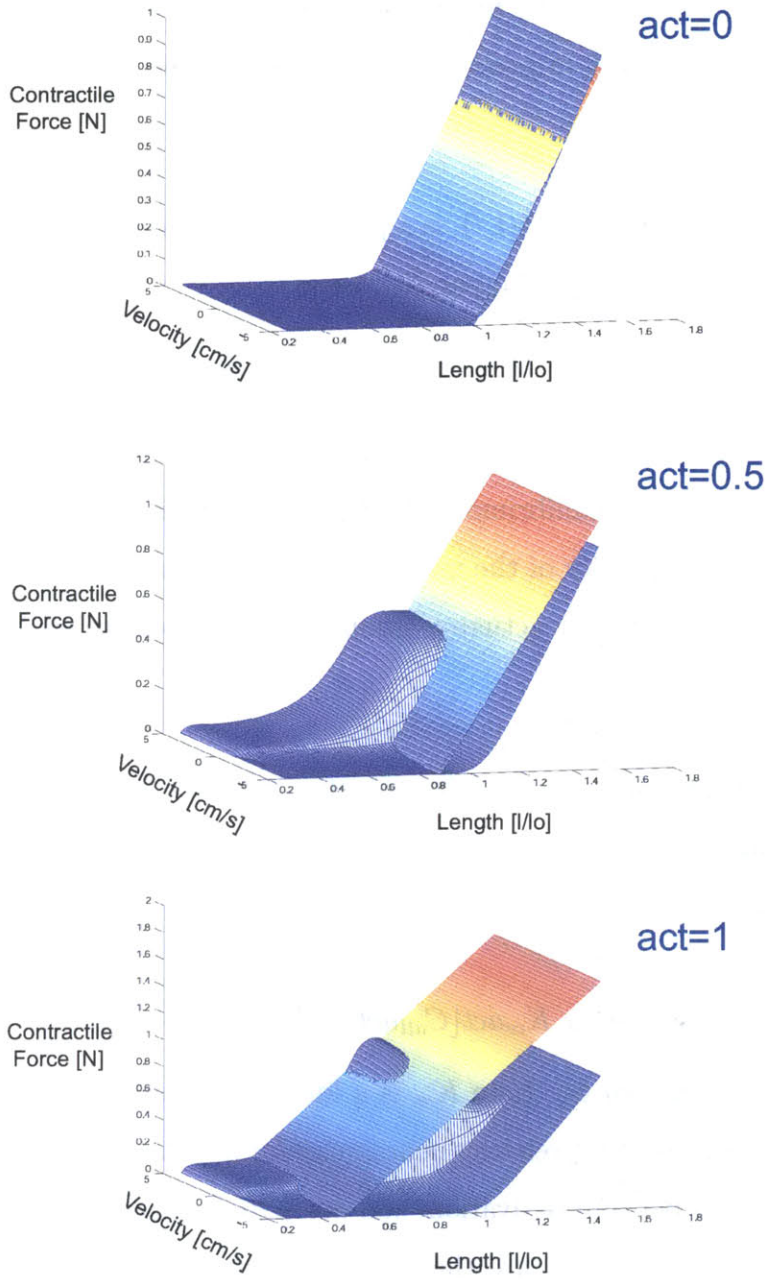

Figure 2-5: Comparison of the Force-Length-Velocity Curves (Contractile Element plus Passive Element Forces) for the Hill Model from Equation (2.7) and the reduced order model presented in Equations (2.8) and (2.9). Note that the total force (PE+CE) is labelled as Contractile Force because muscles *always* produce forces which work to decrease their lengths. Therefore, in order to plot the forces as positive, we define Contractile Force as positive in the direction of decreasing muscle length.

$$F^m(act, l, \dot{l}) = F^{ce}(act, l, \dot{l}) + F^{pe}(l, \dot{l}) \tag{2.10}$$

or alternatively, for a system of n muscles,

$$\mathbf{F}^m(\mathbf{act}, \mathbf{l}, \dot{\mathbf{l}}) = \begin{pmatrix} F_1^{ce}(act_1, l_1, \dot{l_1}) + F_1^{pe}(l_1, \dot{l_1}) \\ \vdots \\ F_n^{ce}(act_n, l_n, \dot{l_n}) + F_n^{pe}(l_n, \dot{l_n}) \end{pmatrix} \tag{2.11}$$

Figure 2-5 plots Equation (2.10) alongside the Hill-type model from Figure 2-4 for different levels of neuromuscular activation. It should be evident from Equation (2.10) that the most significant limitation of the reduced order model occurs in the region of large shortening velocities ($\dot{l_n} \ll 0$) where muscle contractile forces go to zero. In this region, the reduced order model will overestimate the contractile force produced by the muscle. However, for a moderate range of shortening velocities (*i.e.* slower movements), the reduced order model and the full Hill model will predict similar muscle forces.

The primary motivation for adopting the model developed above stems from the absence of complete morphological data for all of the included muscles (see Table 2.2). In the absence of such data, the use of a full Hill model would have increased the number of unknown model parameters dramatically and would have therefore complicated the parameter estimation method presented in Chapter 4.

2.2.3 Neuromuscular Transmission and Excitation-Contraction Coupling

The level of muscular activation (*act* in Equation (2.9)) is controlled by the rate at which action potentials (voltage impulses [26]) are sent from the muscles' corresponding alpha motor neurons (located in the anterior horns of the spinal cord) to the muscle fibers. An increase in the rate of signaling commands a corresponding increase in the muscle's level of contraction, whereas a decrease commands the opposite. The rate of these action potentials in represented in Figure 2-1 by the signal

$\mathbf{u}_\alpha(t)$. Large myelinated nerve fibers originating from these motor neurons carry the action potentials to the muscle. On the way, each nerve fiber branches many times so that a single action potential from one motor neuron stimulates anywhere from three to several hundred skeletal muscle fibers (within a single muscle). The ensemble of muscle fibers innervated by a single motor neuron is called a muscle unit, and that ensemble together with its motor neuron is called a motor unit. The collection of all motor units corresponding to a particular muscle is termed a motor nucleus. In the case of our model, we assume (as is done in most muscle models) that fibers within a muscle are identical and that they act in synchrony. Therefore, each muscle is represented as having only one motor neuron associated with it. Physiologically, the activity of this single motor neuron would represent the net activity (*i.e.* net rate of action potentials) being commanded to a muscle by its entire motor nucleus.

Each nerve branch terminates at the neuromuscular junction (near the fiber's mid-point). Once the action potential reaches the junction, it begins to travel towards the muscle fiber ends (in both directions). The transmission of the action potential from the nerve into the muscle by way of the neuromuscular junction is mediated by the secretion of acetylcholine into the synaptic space between the nerve and the muscle membrane. The time elapsed between the point when the action potential leaves the motor neuron to the point it reaches the neuromuscular junction and is propagated into the muscle varies from 3-10 ms depending on the length of the nerve and the conduction velocity of the nerve [33]. Within our model, this neuromuscular transmission delay is modelled by the time-delay (T_{eff} in Figure 2-1). Assuming that the length of the average efferent fiber is half the length of the frog limb (7.45 cm) and that the conduction velocity of the fibers is (25 m/s), then $T_{eff} \approx 3$ ms.

Once the postsynaptic membrane of the neuromuscular junction (*i.e.* the muscle membrane) is depolarized to its threshold, an action potential propagates along the membrane of the muscle fiber (the sarcolemma). Because a single action potential in a motor neuron can activate hundreds of muscle fibers in synchrony, the resulting

transmembrane currents sum to generate an electrical signal that is readily detectable outside the muscle itself. When more than minimal force is required, many motor neurons generate an asynchronous barrage of action potentials with overlapping action potentials arising in each motor unit. The result is a complex pattern of electrical potentials (typically on the order of 100 μV in amplitude) that can be recorded as an electromyogram (EMG) using simple electrodes on the surface of the overlying skin. The relative timing and amplitude of these patterns recorded over particular muscles reflect the closely aggregate activity of motor neurons that innervate each muscle. The rectified and integrated EMG (a rough estimate of the power of muscular activation) is represented by the symbol $\mathbf{m}(t)$ in Figure 2-1.

The skeletal muscle fiber is so large that action potentials spreading along its surface membrane cause almost no current flow deep within the fiber. To cause contraction, these electrical currents must penetrate to the vicinity of all the separate myofibrils. This is achieved by transmission of the action potentials along transverse tubules (T tubules) that penetrate all the way through the muscle fiber from one side to the other. The T tubule action potentials in turn causes the release of calcium ions into the immediate vicinity of the myofibrils, and these calcium ions in turn cause the muscles' contraction. The level of muscular activation, *act* in Figure 2-1, is then directly related to the strength of the muscle contraction caused by this release of calcium. This overall process is called excitation-contraction (EC) coupling.

Over a range of neural excitations the net behavior of this EC coupling has been found to be substantially linear and can be approximately represented by a critically damped low-pass filter with corner frequency from ρ=11 to 33 radians per second [10]. The transfer function from neural excitation to muscle contraction is represented here as

$$EC(s) = \frac{\rho^2}{(s+\rho)^2} \tag{2.12}$$

where $\rho = 33[radians/sec] \approx 5[Hz]$, and s is the Laplace variable [33]. Equation

(2.12) can be rewritten in matrix notation as follows

$$\mathbf{EC}(s) = \begin{pmatrix} EC_1(s) & 0 & \dots & 0 & 0 \\ 0 & EC_2(s) & 0 & 0 & 0 \\ \vdots & 0 & \ddots & 0 & \vdots \\ 0 & 0 & 0 & EC_{n-1}(s) & 0 \\ 0 & 0 & \dots & 0 & EC_n(s) \end{pmatrix} \tag{2.13}$$

such that

$$\mathbf{act}(t) = \mathbf{EC}(t) * \mathbf{m}(t) \tag{2.14}$$

where $*$ is the convolution operator and $\mathbf{EC}(t)$ is impulse response of the system function matrix $\mathbf{EC}(s)$. The input signal to $\mathbf{EC}(s)$ is the EMG vector $\mathbf{m}(t)$, and the output is the muscle activation vector, $\mathbf{act}(t)$, in Equation (2.10).

2.2.4 Muscle Geometry

Recall from Equations (2.8) and (2.9) that the passive and contractile element forces in our model are functions of both the muscle length, l, and rate of lengthening, $\dot{l}$, while the output of the skeletal forward dynamic model is the vector of joint angles, $\mathbf{\Theta}$. It is therefore necessary to relate angular changes in our kinematic model to the corresponding muscle length changes in our muscle model. Clearly, muscle length changes are dependent on the geometry of a particular muscle's origin and insertion, and their relation is, in general, a nonlinear function of the joint angles. We make the simplifying assumption that muscles have a constant moment arm at each joint. This assumption is motivated by the fact that, within a limited range of the workspace, muscle moment arm values do not change very much, such that they may be taken to be constant to first order. Additionally, if this assumption were not made, the parameter estimation method described in Chapter 4 would further complicated. That is, since a number of moment arm curves were not available, it would have been necessary to obtain estimated curves for each unknown moment arm as opposed to just a single scalar value.

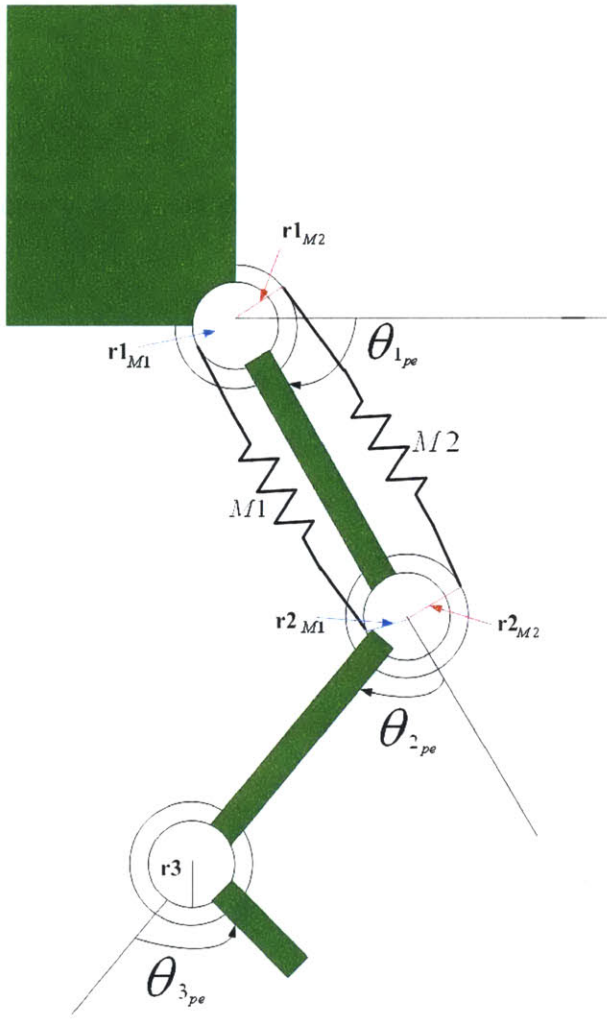

Figure 2-6: Example to demonstrate the relationship between angular changes and muscle length changes. Angles θ_i are defined as positive in the counterclockwise direction (standard robotic manipulator convention).

Employing the constant moment arm assumption makes the relation between angular changes, $\triangle\boldsymbol{\Theta}$, and muscle length changes, $\triangle\mathbf{l}$, very simple. To illustrate, consider muscles $M1$, a biarticular hip-extensor and knee flexor, and $M2$, a biarticular hip flexor and knee extensor, in Figure 2-6. At angles θ_{1_o} and θ_{2_o} the muscle is at length l_{1_o}. At angles θ_1 and θ_2 the muscle's change in length is:

$$l_1 - l_{1_o} = +r_{1_{M1}}(\theta_1 - \theta_{1_o}) + r_{2_{M1}}(\theta_2 - \theta_{2_o}) \tag{2.15}$$

Similarly, for muscle $M2$, at angles θ_1 and θ_2 the muscle's change in length is:

$$l_2 - l_{2_o} = -r_{1_{M2}}(\theta_1 - \theta_{1_o}) - r_{2_{M2}}(\theta_2 - \theta_{2_o}) \tag{2.16}$$

where we have defined θ_i in accordance with the robotic manipulator convention such that θ_i increases in the counter-clockwise direction. This causes hip flexion and ankle plantar extension to be associated with an increase in the hip and ankles joint angles respectively, while knee flexion produces a reduction of the knee joint angle.

Extending Equations (2.15) and (2.16) for the case of n muscles acting about the three joints, we can write the length changes resulting from corresponding angular changes in matrix format, as follows:

$$\mathbf{l} - \mathbf{l}_o = \begin{pmatrix} l_1 - l_{1_o} \\ l_2 - l_{2_o} \\ \vdots \\ l_n - l_{n_o} \end{pmatrix} = \begin{pmatrix} r_{1_{M1}} & r_{2_{M1}} & 0 \\ -r_{1_{M2}} & -r_{2_{M2}} & 0 \\ \vdots & \vdots & \vdots \\ \pm r_{1_{Mn}} & \pm r_{2_{Mn}} & \pm r_{3_{Mn}} \end{pmatrix} \begin{pmatrix} \theta_1 - \theta_{1_o} \\ \theta_2 - \theta_{2_o} \\ \theta_3 - \theta_{3_o} \end{pmatrix} = -\mathbf{M}^\top(\boldsymbol{\Theta} - \boldsymbol{\Theta}_o) \tag{2.17}$$

where n is the number of muscles being considered. Here $\mathbf{M}$ is the muscle moment arm matrix representing the geometry of the n muscles acting on the hindlimb. Consistent with the standard definition of muscle moment arms, we define entry j, k of $\mathbf{M}$ to be positive if the forces generated by muscle j tend to increase θ_k, and negative otherwise. Adopting this definition, it is clear that if muscle j works to increase θ_k, its length decreases – hence the minus sign on the right-hand side of Equation (2.17).

Muscle	MA about Hip [mm] (r1)	MA about Knee [mm] (r2)	MA about Ankle [mm] (r3)
RI	-6.1011	-1.5349	0
AM	-4.1747	0	0
SM	-5.6510	-11.1481*	0
ST	-4.0151	-3.6232	0
IL	3.2987	0	0
VI	2.0958	4.2567	0
RA	7.4820	4.2567	0
GA	0	-2.9897*	-4.1101*
PE	0	4.2160*	3.6533*
BF	-24.9584*	-2.2842*	0
SA	4.4885	-3.0122	0
VE	0.8845	4.2567	0

Table 2.3: Muscle Moment Arms about the Hip, Knee, and Ankle. The three columns in this table correspond to the three columns of $\mathbf{M}^\top$ in Equations (2.17) and (2.18).

The relation between $\dot{\mathbf{l}}$ and $\dot{\mathbf{\Theta}}$ can be obtained by differentiating Equation (2.17) with respect to time and noting that $\mathbf{l}_o$ and $\mathbf{\Theta}_o$ are both constant. Thus,

$$\dot{\mathbf{l}} = -\mathbf{M}^\top \dot{\mathbf{\Theta}} \tag{2.18}$$

Using Equations (2.17) and (2.18), it is possible to fully define the passive and contractile element forces in Equations (2.8) and (2.9) in terms of the hindlimb joint angles, $\mathbf{\Theta}(t)$, and the vector of muscle activations, $\mathbf{act}(t)$.

Table 2.3 summarizes the individual muscle moment arms at each joint. The values included were obtained by taking the average value of the muscle moment arm curves in [29]. A moment arm of zero denotes that the corresponding muscle has no net action at a given joint. Parameters denoted with an asterisk (*) were obtained via the estimation method described in Chapter 4.

2.3 Sensory Feedback

The proper control of muscle function requires not only excitation of the muscle by the anterior motor neurons but also continuous sensory feedback of information from each muscle to the spinal cord giving the status of the muscle at each instant in time. To provide just this type of information, the muscles and their tendons are supplied abundantly with two special types of sensory receptors: muscle spindles and Golgi tendon organs. Muscle spindles are distributed throughout the belly of the muscle and send information to the nervous system about both muscle length, l, and the rate of change of length, $\dot{l}$. Golgi tendon organs, on the other hand, are located in the muscle tendons and transmit information about tendon tension, F^m, and the rate of change of tension, $\dot{F^m}$. For the purpose of our simulation, which only implements the segmental stretch reflex, it will be sufficient to focus on how muscle spindles encode muscle length and and rate of change of length.

2.3.1 The Muscle Spindle

Spindle Structure

Each spindle is 3 to 10 millimeters long. It is composed of 3 to 12 very small intrafusal muscle fibers that are pointed at their ends and attached to surrounding large extrafusal skeletal muscle fibers. Structurally, the spindle can be thought of as tiny muscle embedded within the larger skeletal muscle. In contrast to the extrafusal fibers, however, the central region of each of the intrafusal fibers has either no or few actin and myosin filaments. Therefore, this central portion does not contract when the ends do. Instead, it functions as a sensory receptor. The end portions that do contract are excited by small gamma motor nerve fibers that originate from the small gamma motor neurons in the anterior horns of the spinal cord. These fibers are also called the gamma efferent fibers, in contradistinction to the large alpha efferent fibers that innervate the extrafusal skeletal muscle.

The receptor portions of the spindle, from where sensory fibers originate, are stimulated by the stretching of the spindle's midportion. One can readily see that the muscle spindle receptor can be excited in two ways. First, if the whole muscle (intrafusal and extrafusal fibers) is stretched, the midportion of the spindle will also stretch and excite the receptor. Alternatively, even if the length of the entire muscle does not change, contraction of the ends of the spindle's intrafusal fibers will also cause the spindle's midportion to stretch and, therefore, excite the receptor.

Two types of sensory endings are found in the receptor area of the muscle spindle. The first called the primary ending is a large sensory fiber (averaging 17 micrometers in diameter) that encircles the very central portion of the receptor area. This large diameter fiber transmits sensory signals from the spindle to the spinal cord at velocities of 70 to 120 m/sec. Alternatively, the secondary endings are smaller diameter fibers (averaging 8 micrometers in diameter) that mainly encircle the intrafusal fibers on one side of the primary ending. Although there is usually but one secondary ending per spindle, it is not uncommon for one spindle to have two.

The spindle itself is composed of two types of intrafusal fibers: nuclear bag fibers and nuclear chain fibers. Nuclear bag fibers are characterized by having a large number of nuclei congregated in an expanded bag in the central portion of the receptor area. Nuclear chain fibers are about half as large in diameter and half as long as the nuclear bag fibers and have nuclei aligned in a chain throughout the receptor area. The primary nerve ending innervates both the nuclear bag and nuclear chain fibers, while the secondary ending usually innervates only the nuclear chain fibers.

Spindle Function

When the receptor portion of the muscle spindle is stretched slowly, the number of impulses transmitted from both the primary and secondary ends increase almost in direct proportion to the stretch. Conversely, when the spindle is contracted slowly, the number of impulses decreases. This is called the static response since the primary

and secondary endings continue to transmit their signals for as long as the receptor itself remains stretched or contracted. Because the nuclear chain type of intrafusal fibers is innervated by both the primary and secondary endings it is believed that these nuclear chain fibers are mainly responsible for the static response. The static response, therefore, encodes information relating to length, l, of the muscle.

In contrast, when the length of the spindle receptor is increased or decreased suddenly, the primary ending (but not the secondary ending) is stimulated especially powerfully. The primary ending responds extremely actively to a rapid rate of change of the spindle length, $\dot{l}$. Because only the primary endings transmit the dynamic response and almost all nuclear bag intrafusal fibers have only primary endings, it is assumed that the nuclear bag fibers are responsible for this powerful response. By way of both the static and dynamic responses, the muscle spindle sends the spinal cord information encoding both the current muscle length, l, and its rate of change, $\dot{l}$.

Spindle Control

The gamma motor nerves, which connect the motor neurons to the muscle spindle, can be divided into two types: gamma-dynamic (γ-d) and gamma-static (γ-s). For the frog, which lacks the gamma motor system, we will assume that the beta motor neurons can be divided in the same manner. The first of these, γ-d, excites mainly the nuclear bag fibers, and the second, γ-s, mainly the nuclear chain fibers. When the γ-d fibers excite the nuclear bag fibers, the dynamic response of the muscle spindle becomes tremendously enhanced, whereas the static response is hardly affected. On the other hand, stimulation of the γ-s fibers, which excite the nuclear chain fibers, enhances the static response while having little influence on the dynamic response.

To emphasize the importance of the gamma efferent system, one needs to recognize that 31 percent of all motor nerve fibers to the muscle are gamma efferent fibers rather than large alpha motor fibers. Whenever signals are transmitted from the

motor cortex or from any other area of the brain to the alpha motor neurons, in most instances, the gamma motor neurons are stimulated simultaneously, an effect called alpha-gamma coactivation. This causes both the extrafusal and intrafusal muscle fibers to contract at the same time.

The purpose of contracting the muscle spindle fibers at the same time as the large skeletal muscle fibers contract is twofold. First, it decreases the length of the spindle in unison with the muscle. This prevents sensory information from the spindle from opposing the muscle contraction being commanded to the muscles by way of the alpha motor neurons. Second, it maintains the spindle biased so the information it is encoding is always relative to currently "commanded" muscle length. For instance, if the muscle spindle should not contract and relax along with the large muscle fibers, the receptor portion of the spindle would sometimes flail and at other times be overstretched, in neither case operating under optimal condition for the muscle spindle.

The rate of firing of the muscle spindle as a function of both muscle length, $l(t)$, and rate of change of length, $\dot{l}(t)$, can be summarized as follows. Let $Z(t)$ be the elongation of the spindle sensory zone as a function of time and $R(t)$ be the instantaneous rate of discharge of the spindle, then

$$R(t) = K(Z(t) + p\dot{Z}(t)) \tag{2.19}$$

where K and p are both constants. In Equation (2.19) (modified from [16]) the constant p reflects the rate sensitivity of the encoder process which is the same for primary and secondary endings. This constant is therefore not altered by fusimotor activity. Hasan in [16] finds that for the case of sinusoidal variations, the constant p equals 0.1. Therefore in the frequency domain, Equation (2.19) becomes

$$R(s) = K(1 + 0.1s)Z(s) \tag{2.20}$$

where s is the Laplace variable, K is the reflex gain (controlled by the gamma system), and $R(s)$ and $Z(s)$ correspond to the Laplace transform of $R(t)$ and $Z(t)$ respectively.

When $Z(s)$ is an impulse function, we obtain the impulse response of the spindle, $R(s) = K(1 + 0.1s)$. $R(s)$ can be written in matrix form as was done for $EC(s)$ in Equation (2.13). This system function matrix will be denoted $\mathbf{R}(s)$. The length of the spindle sensory zone is given by

$$Z(t) = l - (l_o - C_{atl}act(t)) \tag{2.21}$$

where l, l_o, C_{atl}, and act are as defined in Equation (2.9).

Putting Equations (2.20) and (2.21) together in matrix format, we obtain the spindle responses for a system of n muscles. We shall denote this response as $\mathbf{u}_{reflex}(\mathrm{t})$ for reasons that will become obvious when we discuss the monosynaptic stretch reflex later. For now,

$$\mathbf{u}_{reflex}(t) = \mathbf{R}(t) * (\mathbf{l}(t) - (\mathbf{l}_o - C_{atl}\mathbf{act}(t))) \tag{2.22}$$

where, as before, $*$ is the convolution operator and $\mathbf{R}(t)$ is the impulse response of the system function matrix $\mathbf{R}(s)$. The term $C_{atl}\mathbf{act}(t)$, denoted as $\mathbf{u}_\beta(t)$ in Figure 2-1, represents the effects of alpha-gamma coactivation, so that the spindle rest length $(\mathbf{l}_o - \mathbf{u}_\beta(t))$ changes in synchrony with that of the extrafusal muscle (see Equation (2.9)).

2.3.2 Proposed Functions of Sensory Feedback

One of the most well accepted functions of sensory feedback is its role in the reinforcement of descending motor commands. For example, stretching of muscle produces an increase in spindle discharge, leading to muscle contraction and consequent shortening of the muscle. But this muscle shortening leads to a decrease in spindle discharge, a reduction of muscle contraction, and a lengthening of the muscle. Thus, this stretch reflex loop (see Section 2.4.2 below) acts continuously, tending to keep muscle length close to a desired or reference value, specified by $\mathbf{u}_{desc}(t)$. Therefore, the stretch reflex pathway provides a mechanism for the rejection of disturbances

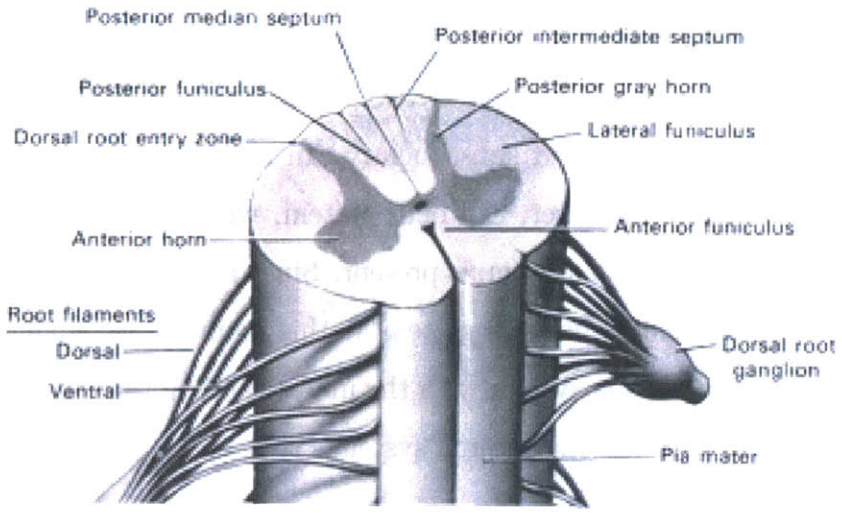

Figure 2-7: Transverse section of the spinal cord in the lower cervical region

arising either from unknown variations in external loads or intrinsic irregularities in the contraction of muscle. Other types of reflexes (such as long-loop cortical reflex pathways and force feedback from Golgi tendons) are employed by the nervous system to aid in the control of muscle as well, with the relative contribution of each reflex pathway dependant on the particular muscle and the task.

2.4 Spinal Cord Circuitry

A detailed discussion of spinal cord anatomy is beyond the scope of this thesis. A brief introduction is provided here to enable a more concise description of basic motor functions. For further background and details, the reader is referred to several useful texts [26] [15]. Figure 2-7 illustrates some of the most important anatomical features of the cord, which will be helpful in understanding the following section.

2.4.1 Types of Neurons within the Cord

Located in each segment of the anterior horns of the cord gray matter are several thousand neurons called the anterior motor neurons. These neurons, which are 50 to

100 percent larger than most of the surrounding neurons, give rise to the nerve fibers that leave the cord by way of the anterior roots and innervate the skeletal muscle fibers. Anterior motor neurons come in two types – the alpha and gamma motor neurons, which will be described subsequently. In actuality, the gamma system is absent in the frog [13]. However, the beta system, which is thought to work in a manner similar to the gamma system, is present. Since relatively little research exists on the functional details of the beta system at this moment, we shall proceed with the description of the gamma system with the understanding that the beta system in the frog most likely parallels the gamma system's role.

The alpha motor neurons give rise to large nerve fibers (averaging 14 micrometers in diameter) that innervate the skeletal muscle fibers. Stimulation of a single nerve fiber excites from a few to as many as several hundred skeletal muscle fibers, which are collectively termed the motor unit. In addition to the alpha motor neurons that excite contraction of the skeletal muscle fibers, about one half as many much smaller gamma motor neurons are located in the spinal cord anterior horns. These gamma motor neurons transmit impulses through smaller fibers (averaging 5 micrometers in diameter) to intrafusal fibers. These fibers are part of the muscle spindle discussed previously.

Along with these two types of motor neurons, the spinal cord has a multitude of smaller interneurons [15] which constitute the basic building block of most spinal reflex circuits. Interneurons are present in all areas of the cord gray matter in the dorsal horns, the anterior horns, and the intermediate areas between these two. These cells are numerous – about 30 times as numerous as the anterior motor neurons. They are small and highly excitable, often exhibiting spontaneous activity and capable of firing as rapidly as 1500 times per second. They have many interconnections with one another, and many of them directly innervate the anterior motor neurons (see Figure 2-8). The interconnections among the interneurons and anterior motor neurons are responsible for most of the integrative functions of the spinal cord that are discussed

in Chapter 1 and the remainder of this chapter.

Only a few incoming sensory signals from the spinal nerves or signals from the brain terminate directly on the anterior motor neurons. Most of these signals are transmitted first through interneurons, where they are appropriately processed. For example, also located in the ventral horns of the spinal cord in close association with the motor neurons are a large number of small interneurons called Renshaw cells. Almost immediately after the axon leaves the body of the anterior motor neuron, collateral branches from the axon pass to the adjacent Renshaw cells. These in turn are inhibitory cells that transmit inhibitory signals back to the nearby motor neurons, an effect called recurrent inhibition. The primary effect of recurrent inhibition is to regulate motor neuron excitability and stabilize motor neuron firing. Figure 2-8 illustrates an example of recurrent inhibition by a Renshaw cell.

The potential processing power of interneurons in the spinal cord becomes readily apparent when one notes that more than one half of all the nerve fibers that ascend and descend in the spinal cord are propiospinal fibers. These fibers run from one segment of the cord to another, transmitting the 'result' from interneuronal circuits at one level to the next. This allows spinal circuits to take the outputs of a variety of interneuronal circuits and further process them to extract more detailed information. In addition, as sensory fibers enter the cord from the dorsal cord roots, they also bifurcate and branch both up and down the spinal cord. While some of these branches transmit signals only a segment or two, others transmit the signals for many segments. These ascending and descending fibers of the cord provide the pathways for the integration of both interneuronal signals and sensory information into multisegmental reflexes. One example of such a multisegmental reflex coordinates simultaneous movement of the forelimbs and hindlimbs when they are placed in direct contact with the ground (as would be experienced during normal walking)[26].

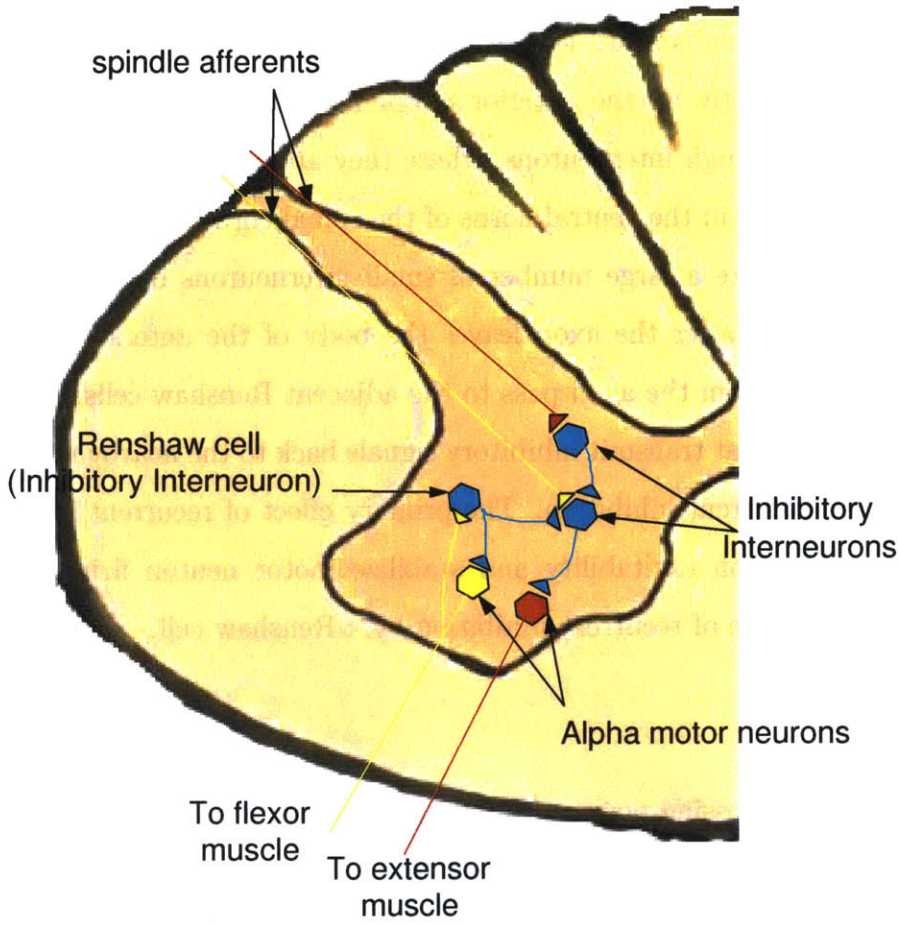

Figure 2-8: Example of recurrent inhibition by a Renshaw cell. Renshaw cells also send collaterals to synergist motor neurons (not shown) and inhibitory interneurons (shown). Thus, descending inputs that modulate the excitability of the Renshaw cell adjust the excitability of all the motor neurons around a joint. This figure also shows how inhibitory interneurons in the spinal cord send inhibitory signals to antagonist (extensor) motor neurons when muscle spindles in the agonist (flexor) are activated. (Adapted from [26])

2.4.2 Monosynaptic Muscle Stretch Reflex

The simplest manifestation of the muscle spindle function is the muscle stretch reflex (also called the myotatic or segmental reflex) – that is, whenever a muscle is stretched, excitation of the spindles causes reflex contraction of the large skeletal muscle fibers of the same muscle and closely allied muscles with similar mechanical action.

Figure 2-9 demonstrates the neuronal circuit which implements the muscle stretch reflex. It shows a nerve fiber which originates in a muscle spindle entering the dorsal root of the spinal cord. In contrast to most other nerve fibers entering the cord, one nerve branch passes directly to the anterior horn of the cord gray matter and synapses directly with anterior motor neurons. These neurons then send nerve fibers back to the same muscle from whence the muscle spindle fiber originated. Thus, this is a monosynaptic pathway that allows a reflex signal to return with the shortest possible delay back to the muscle after excitation of the spindle. The transmission delay incurred by the spindle afferent signals on their way back to the spinal cord is represented by T_{aff} in Figure 2-1. For simplicity, we assume that T_{aff} equals $T_{eff} = 3ms$.

Modelling the recruitment of anterior motor neurons as linear (*i.e.* their rate of firing is directly proportional to the sum of the rates of all its synaptic inputs) we are able to implement the effect of this monosynaptic reflex as,

$$\mathbf{u}_{\alpha}(t) = \mathbf{u}_{desc}(t) + \mathbf{u}_{reflex}(t) \tag{2.23}$$

where $\mathbf{u}_{\alpha}$(t) is the total firing rate of the alpha motor neurons, $\mathbf{u}_{reflex}$(t) is the vector of spindle responses from Equation (2.22), and $\mathbf{u}_{desc}$(t) represents the signals descending from higher motor centers towards the alpha motor neurons. It should be noted that there are potentially important nonlinear effects associated with the recruitment of motor units within the spinal cord [11]. For example, motor units tend to be activated (recruited) in order of increasing size (and strength) – as dictated by the

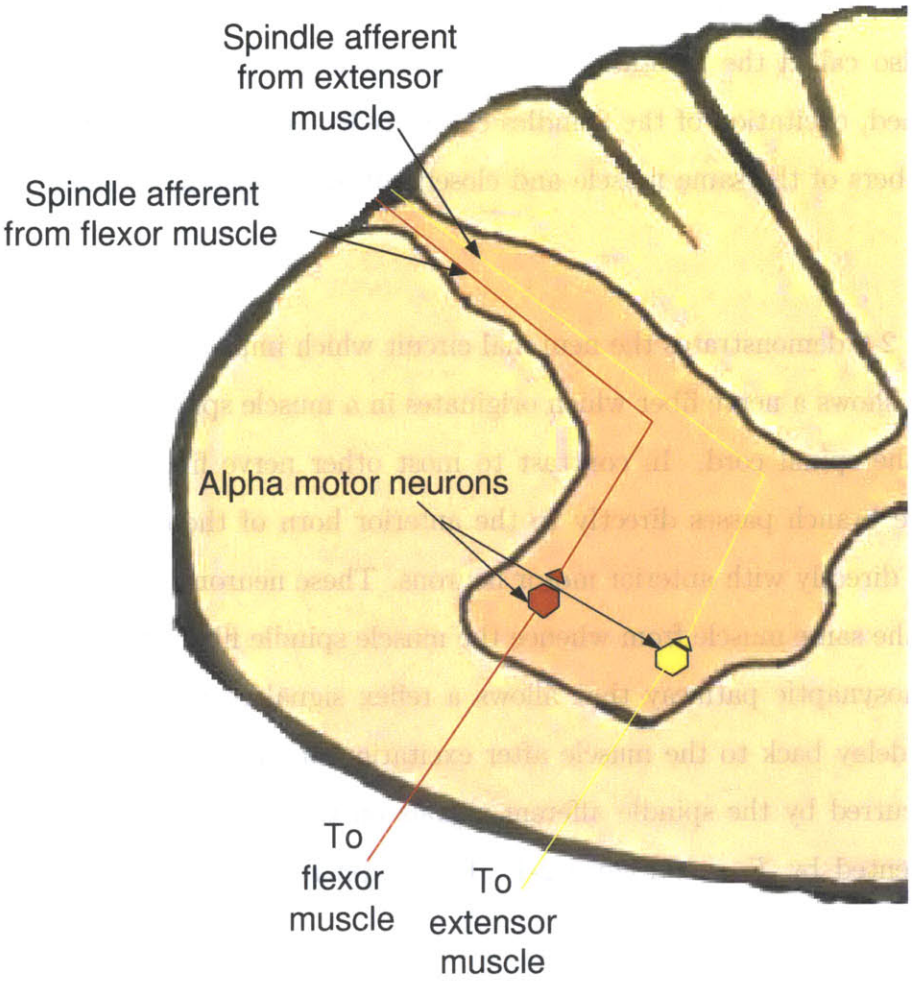

Figure 2-9: Monosynaptic Stretch Reflex. In this example, suppose that the flexor muscle is stretched by an external disturbance (the extensor muscle will be shortened correspondingly). The spindle receptor within the flexor muscle would be vigorously activated and increase its firing rate. This increased rate of firing would in turn cause the flexor muscle to contract – correcting for the external stretch. Simultaneously, the extensor's spindle would decrease its rate of firing (because of the extensor's shortening) and cause the extensor to "give in" to the flexor's contraction. In this way, the stretch reflex helps the muscles to maintain their current length.

Henneman size principle. It is also common that all or most of the available motor neurons become recruited, so there is also a saturation of the motor signal (when no motor neurons can be recruited). However, these effects are strongest at the extremes of motor neuron recruitment, and we therefore treat them as second order effects. Equation (2.23) neglects these second order effects and treats the recruitment of motor neurons as linear.

2.4.3 Representation of Muscle Synergies Encoded within the Spinal Cord

As discussed in Chapter 1, Saltiel *et al.* found seven muscle synergies whose linear combination accounted for more than 91% of the variance of the pooled EMG data from 12 hindlimb muscles [36]. These studies therefore suggest that the rectified and integrated EMG, $\mathbf{m}(t)$, can be written as

$$\mathbf{m}(t) = \mathbf{W}\mathbf{d}(t) \tag{2.24}$$

where $\mathbf{W}$ is the matrix whose columns are the muscle synergy vectors, w_i ; $i = 1..7$, and $\mathbf{d}(t)$ is the vector of synergy scaling coefficients as explained in Chapter 1. For reference, the synergies are numerically summarized in Table 2.4, and graphically represented in Figure 2-10.

Although experiments have not yet been carried out to verify how the muscle synergies are actually implemented within the spinal cord, the findings of [36] demonstrate the net effect of interneuronal networks within the spinal cord can be represented as groups of static muscle ratios (muscle synergies, w_i). These static muscle synergies in turn can be recruited in a linear fashion by directly stimulating within the spinal cord, resulting in the (linear) recruitment of alpha motor neurons (over a range of activation) and the production of muscle EMG. The signal $\mathbf{d}$(t) in Equation (2.24) captures the effects of both the intraspinal stimulation (as performed in [36]) and the effects of higher interneuronal circuits that might integrate descending command

Muscles Names	A	B	C	D	E	F	G
Rectus Internus (RI)	0	0.4060	0	0.0881	0.3412	0	0.0320
Adductor Magnus (AM)	0	0.6673	0.0102	0.0683	0.1218	0	0
Semimembranosus (SM)	0.0009	0.2135	0.1226	0.5737	0	0	0
Semitendinosus (ST)	0.0095	0	0.0772	0	0.8992	0	0
Iliopsoas (IP)	0	0	0	0.2605	0.2449	0.6280	0
Vastus Internus (VI)	0	0.0983	0	0	0	0.3145	0.4469
Rectus Anterior (RA)	0.2418	0	0.1929	0.0486	0	0.6013	0
Gastrocnemus (GA)	0.9541	0.0282	0	0	0	0	0.0338
Peroneus (PE)	0.1654	0	0.0011	0.1140	0.0013	0	0.8861
Biceps Femoris (BF)	0	0.1081	0.9704	0	0.0104	0	0.0622
Sartorius (SA)	0.0472	0.5675	0	0	0	0.3715	0.0119
Vastus Externus (VE)	0.0387	0	0	0.7584	0	0.0844	0.0940

Table 2.4: Synergies Vectors, w_i, from [36]. The columns of this table correspond to the columns of the **W** matrix in Figure 2-1. The labels above each column correspond to the rows of Figure 2-10.

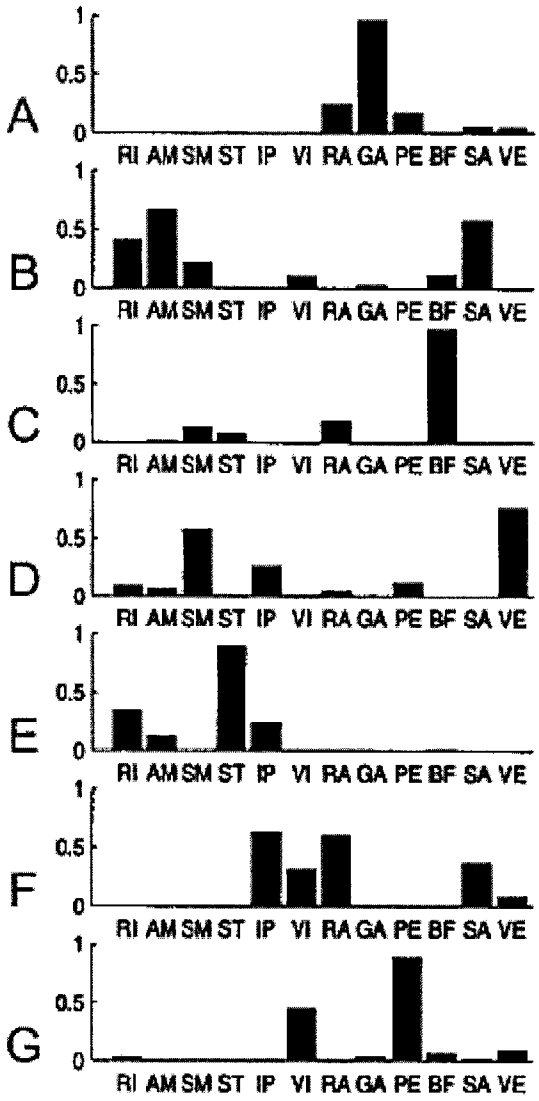

Figure 2-10: Graphical representation of the columns of Table 2.4. This collection of synergies is used for this simulation study because it constitute the constituted the best solution (in terms of data variance explained) as described in [36]. (Reprinted with permission from [36])

information and sensory feedback to recruit muscle synergies. Note that interpreting the signal $\mathbf{d}(t)$ in this manner is entirely consistent with the findings of Kargo and Giszter [27], which observed that the recruitment of corrective force fields were triggered on-line during wiping by cutaneous feedback signaling obstacle collision. Given our demonstration in Chapter 1 that every muscle synergy, w_i, has a corresponding endpoint force field, the corrective force field can be thought of as arising from the recruitment of a set of muscle synergies by corrective interneuronal circuits activated by afferent feedback from the limb.

Furthermore, this conceptual interpretation of muscle synergies is also consistent with the findings of convergent force fields (CFFs) observed within deafferented preparations by Giszter *et al.* [13]. That is, since deafferentation would only affect the generation of the monosynaptic stretch reflex, $\mathbf{u}_{reflex}$, along with any components of $\mathbf{d}(t)$ arising from interneuronal sensory circuits, the underlying force fields (arising from the static muscle synergies) would still persist.

Figure 2-11 demonstrates an example of how three muscle synergies between eight muscles may be implemented by an interneuronal network. The static muscle synergies, w_i, are encoded by the strengths of the synaptic connections, $w_{j,i}$, between the input and output interneurons. The rate of firing specified by $c_1(t)$, for example, is scaled down by factors w_{11},w_{61},and w_{81}, upon passing through the neuron w_1 to become u_{desc_1}, u_{desc_2}, and u_{desc_3}. Assuming that the output neurons (in red) are recruited in a linear fashion (*i.e.* their output firing rates are the sum of their input firing rates), the descending command can be written as arising from a linear combination of static muscle synergies (w_1, w_2, and w_3).

Note that in Figure 2-11, we interpret the descending command to be equal to

$$\mathbf{u}_{desc}(t) = \mathbf{W}\mathbf{d}(t) \tag{2.25}$$

This is done with the understanding that the net effect of alpha-gamma (alpha-beta) coactivation is to help the muscular system track the descending command while

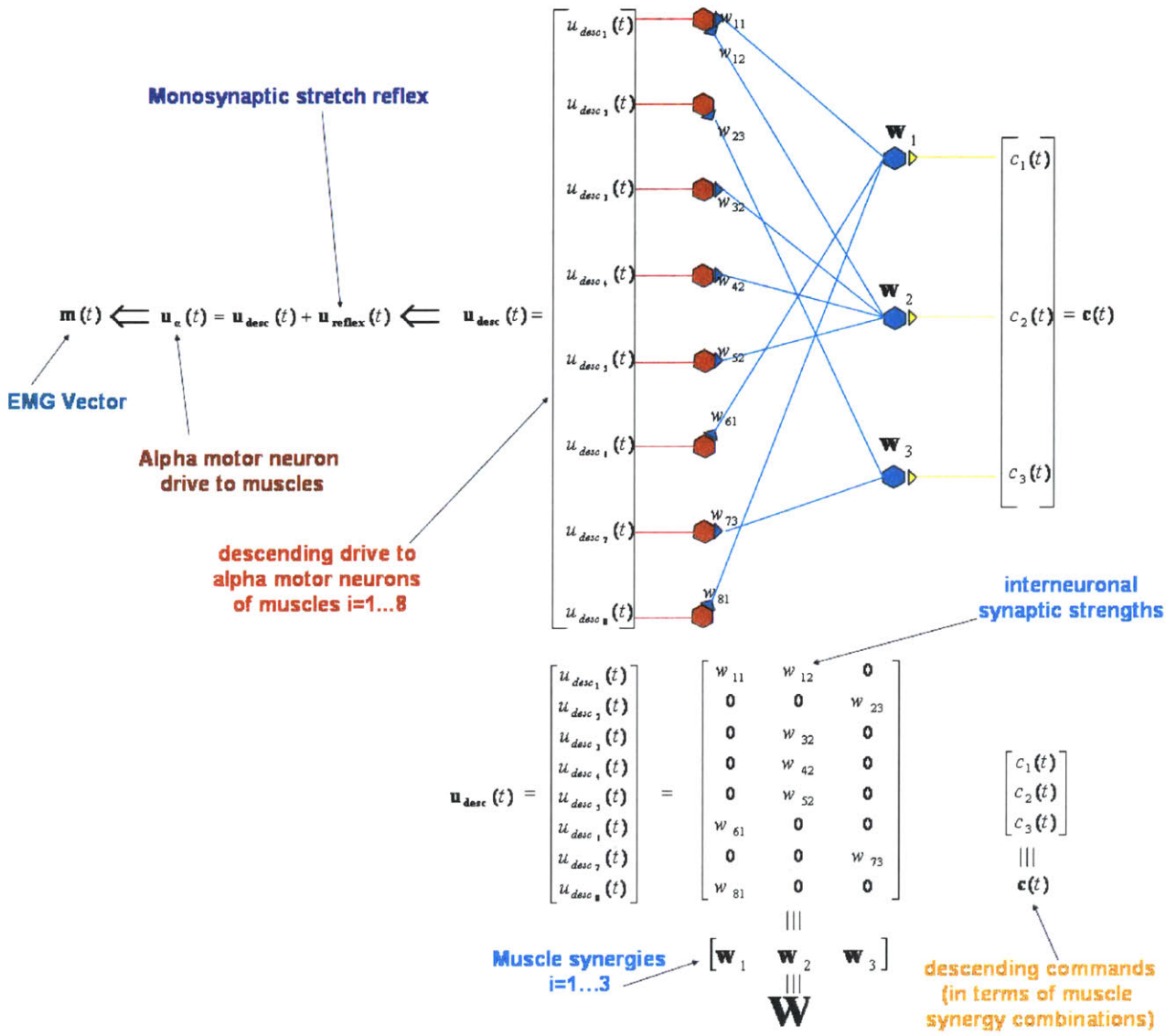

Figure 2-11: Example demonstrating how static muscle synergies may be implemented within the spinal cord. In Chapter 5, an alternative representation in terms of Kinematic Control Synergies will be presented.

correcting any deviations that may occur from it. Therefore, the role of $\mathbf{u}_{reflex}$ is to assure that the descending command, $\mathbf{u}_{desc}$(t), is appropriately modified so that the resulting alpha motor neuron drive and EMG are those required to drive the muscular system as specified by $\mathbf{u}_{desc}$(t). This partitioning has the implied assumption that interneuronal networks at higher levels of the spinal cord contribute to the formation of the signal, $\mathbf{d}(t)$. Interneuronal circuits only control movement via the recruitment of muscle synergies and not via the direct interaction with motor neurons. However, because only the spinal reflex is included in this model, there are no interneuronal contributions to the signal $\mathbf{d}(t)$ in the model.

Chapter 3

Plant Model Identification

As mentioned in Chapter 2, a small number of unavailable physiological parameters – muscle model parameters and unknown muscle morphological parameters – required estimation. In order to obtain parameter estimates that were both physiologically plausible and resulted in a model that recreated realistic kinematics when driven with actual EMG signals, a parameter estimation was performed. This section presents the details of the developed estimation algorithm and presents the resulting parameters. The chapter concludes with a short discussion of the physiological plausibility of the parameters obtained via estimation.

3.1 Paritioning of Model Parameters for Estimation

In order to reduce the total number of parameters requiring estimation, the muscle model presented in Chapter 2 is partitioned in the following manner. Instead of finding the corresponding values of K_{ce}, K_{pe}, B_{cv}, and B_{pv} for each individual muscle (4×12=48 parameters), these parameters are made the same for each muscle so that only four muscle parameters need to be found via estimation. The physiological reason behind this partitioning is that individual muscles are structurally very similar and the difference in the forces they generate is largely a result of their different sizes.

Therefore, once the model is partitioned in this fashion, the vector of muscle forces, $\mathbf{F}^M$, can be determined from the unscaled muscle forces, $\mathbf{F}_u^M$, simply by scaling each by a measure of the relative strength of the individual muscles (represented by a diagonal scaling matrix S). This is summarized by Equation (3.1).

$$\mathbf{F}^M = \mathbf{S}\mathbf{F}_u^M \tag{3.1}$$

As a measure of the relative muscle strengths both muscle physiological cross-sectional area (PCSA) ratios and maximum isometric force (MIF) ratios from [29] were used. Table 3.1 summarizes the values for the two types of ratios used. Note that both the PCSA and MIF ratios were unavailable for muscles GA,PE, and BF (from Table 2.4) and were found via estimation as well. All the ratios are computed relative to the value of Vastus Internus (VI) which was the muscle with the largest PCSA and MIF values in [29].

The estimation algorithm described below was run with both PCSA and MIF ratios. In both cases, the estimation results were very similar. Therefore, for brevity, the results presented will be those obtained with the PCSA values in Table 3.1 with the understanding that the results with MIF values are essentially identical.

3.2 Parameter Estimation Procedure

3.2.1 Preprocessing of Raw EMG and Kinematic Signals

Raw EMGs from all twelve hindlimb muscles of intact bullfrogs during a variety of kicking tasks at rate of $1KHz$ were obtained from Dr.Andrea D'Avella (data from [8]). Each raw EMG was then full-wave rectified and filtered offline with a fifth-order Butterworth filter with a corner frequency of $5Hz$ (Winter suggests in [43] a value of $3Hz$, although this number varies from $3 - 50Hz$ from one researcher to the next). This filtering provides a moving average of the raw EMG signal that can be better related to kinetic data because it follows a similar trend to the tension at the tendon

Muscle	Physiological Cross-sectional Area	Estimated Maximum Isometric Force
RI	.4554	.4553
AM	.2748	.1455
SM	.3389	.3390
ST	.2094	.2093
IL	.1147	.1047
VI	1.0000 (51.96 $[mm^2]$)	1.0000 (14.19 $[N]$)
RA	.0837	.0839
GA	.4088*	.3524*
PE	.2126*	.1754*
BF	.4046*	.4614*
SA	.0706	.0712
VE	.2748	.2740

Table 3.1: Muscle Physiological Cross-sectional Area (PCSA) and Estimated Maximum Isometric Force (MIF) Ratios from [29]. (*) denotes values unavailable in [29] and estimated via parameter estimation.

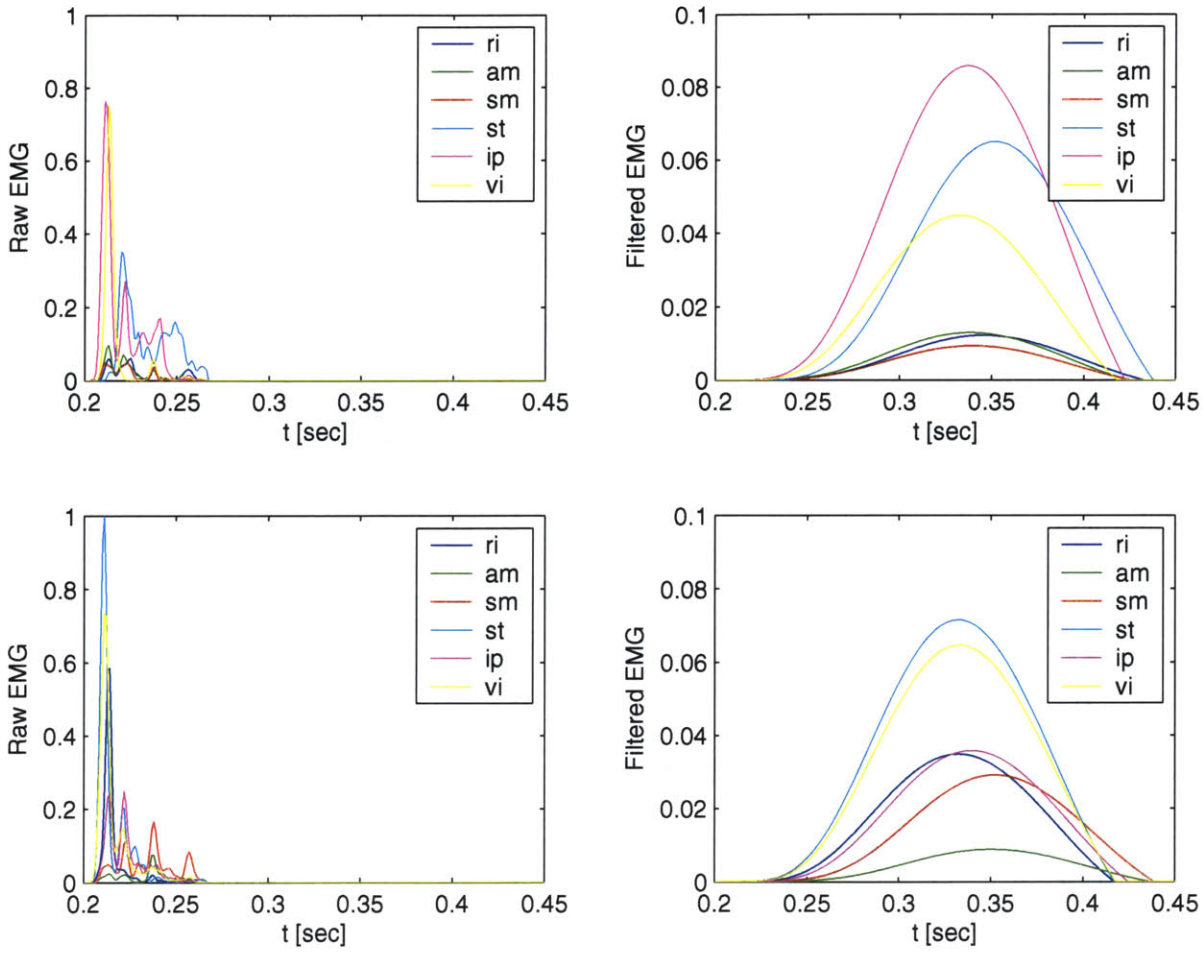

Figure 3-1: Comparison of Raw EMG to Filtered EMG

in both patterning and timing [43]. Once the raw EMG has been processed in this manner, and all the negative components of the filtered signal have been set to zero, it is treated as equivalent to the $\mathbf{m}(t)$ vector described in Chapter 2. The negative components of the filtered EMG signal are set to zero in order to keep the muscle activation signals, $\mathbf{act}(t)$, in the range of zero to one. Joint kinematics ($\mathbf{\Theta}(t)$), also obtained from Dr. D'Avella, were derived from videotape recordings of the motion using a digital video camera (29.97 frames/s, Sony TRV-9) as described in [8].

Figure 3-1 illustrates the effects of filtering the rectified raw EMGs with a fifth-order butterworth, followed by zeroing of the signals negative components. Although the raw and filtered EMG look very different (in both their time duration and amplitude),

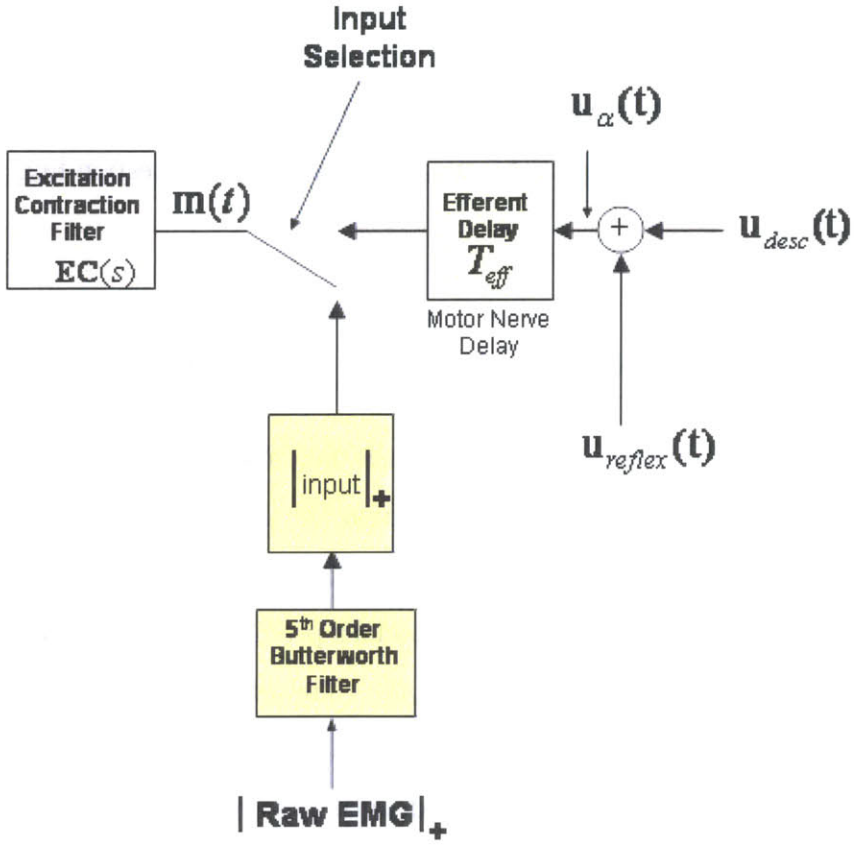

Figure 3-2: Graphical representation of raw EMG processing and its relation to the model described in Chapter 2. Compare with Figure 2-1

it will be demonstrated in Chapter 4 that the resulting kinematics from both are very similar. The reason for their similarity can be attributed to the low-pass filtering effects of the Excitation-Contraction Coupling filter ($\mathbf{EC}(s)$) whose corner frequency is also $5Hz$. Therefore, the activation signal vector, $\mathbf{act}(t)$ received by the muscles in either case is qualitatively very similar. In order to correct for the amplitude difference observed in Figure 3-1, the filtered signal was scaled to the same amplitude as the original.

Figure 3-2 demonstrates how the raw EMGs were processed and input to the model described in Chapter 2. Once the raw EMGs have been filtered, they are held to be equivalent to the EMG vector signal, $\mathbf{m}(t)$. In terms of notation, whenever it is necessary to differentiate between the two sources of EMG, the result of the raw EMG processing will be denoted by $\mathbf{m}_{actual}(t)$, and the corresponding joint kinematics by $\mathbf{\Theta}_{actual}(t)$.

3.2.2 Parameter Estimation Algorithm Description

A gradient descent algorithm on the kinematic error, summarized in Figure 3-3, was used in order to obtain the optimal (in the least squared error sense) unknown model parameters for our model. Using the filtered EMGs, $\mathbf{m}_{actual}(t)$, as input to the hindlimb model (Figure 3-2), the model's predicted kinematics, $\mathbf{\Theta}(t)$, were compared to the recorded kinematics, $\mathbf{\Theta}_{actual}(t)$. The unknown model parameters (K_{ce}, K_{pe}, B_{ce}, B_{pe}, C_{atl}, moment arms for SM, GA PE, and BF, and relative strengths for GA,PE, and BF) were then varied until the resulting squared kinematic error was minimized.

3.3 Parameter Estimates

Table 3.2 summarizes the muscle model parameter values obtained via estimation. Tables 2.3 and 3.1 summarize the values obtained for both the estimated moment arms and the relative muscles strength (PCSA and MIF) ratios respectively.

3.3.1 Physiological Plausibility of the Parameter Estimates

In order to determine if the muscle parameter values obtained from the parameter estimation were within physiological ranges, we begin by comparing the model-predicted and actual stress generated by one of the muscles in our model, the Sartorius.

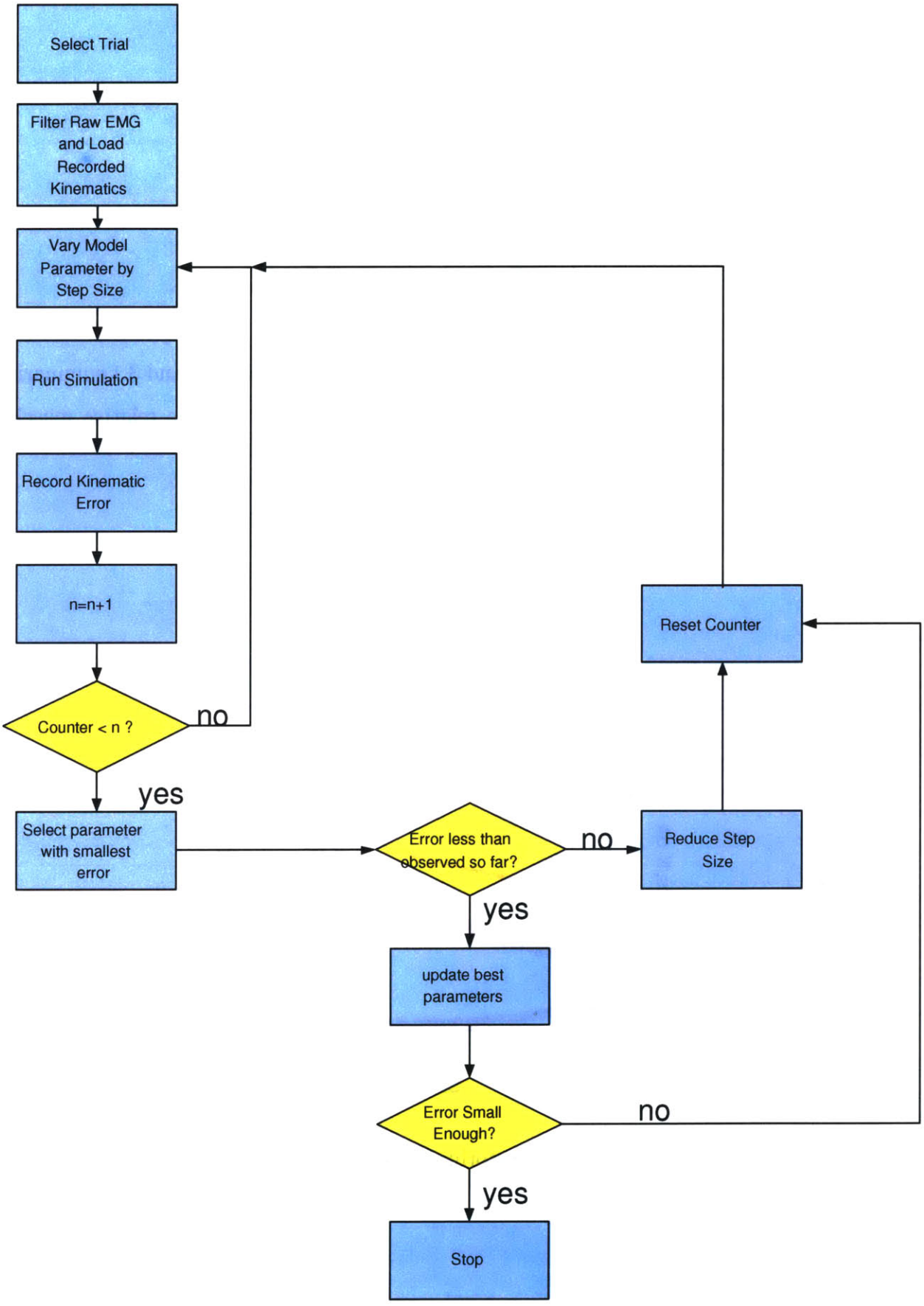

Figure 3-3: Graphical summary of parameter estimation algorithm

Parameter	Value
K_{ce}	$2.20[\frac{N}{mm}]$
K_{pe}	$0.26[\frac{N}{mm}]$
B_{cv}	$0.22[\frac{N \cdot s}{mm}]$
B_{pv}	$4.07 \cdot 10^{-3}[\frac{N \cdot s}{mm}]$
C_{atl}	$36.9960[mm]$

Table 3.2: Muscle Model Parameter Estimation Results.Tables 2.3 and 3.1 summarize the values obtained for both the estimated moment arms and the relative muscles strength (PCSA and MIF) ratios respectively.

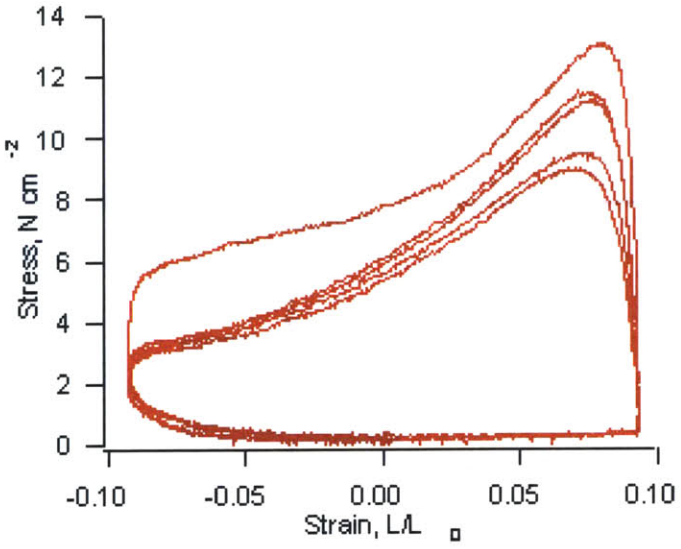

Figure 3-4: Sartorius Stress Strain Curve [17]

Figure 3-4 shows the stress versus strain for the Sartorius muscle of frog (20^o C) [17]. To assess the potential for power output a cyclical work protocol was used here with a sinusoidal length trajectory, with a total strain of 16% or 20% and a frequency of 5 Hz. The average power (averaged over the entire cycle) is $94 \pm 7W/kg$, with a peak power of $333 \pm 19W/kg$.

In order to determine the stress developed by the Sartorius muscle in our model as a function of its length, we divide the muscle stiffness, K_{ce}, by the physiological cross sectional area of the Sartorius, A_{cs}, as shown in Equation (3.2).

$$\frac{K_{ce}}{A_{cs}} = \frac{2.2\frac{N}{mm} \times 7.06\%}{51.96mm^2 \times 7.06\%} = 42.34\frac{N}{cm^3} \tag{3.2}$$

Assuming that the rest length of the Sartorius is $l_o = 6cm$ (similar to the size of the femur) then at $\frac{l}{l_o} = 0.025, l = 0.15[cm]$, the stress developed by the Sartorius, according to our muscle model, is $42.34\frac{N}{cm^3} \times 0.15cm = 6.35\frac{N}{cm^2}$. This value matches quite closely with that observed in Figure 3-4. It should be noted, however, that at higher fractional length changes, $\frac{l}{l_o}$, the discrepancy between the predicted and actual stress values becomes much larger. Therefore, our model makes accurate prediction of the generated muscle stress for small muscle length changes about equilibrium. At $\frac{l}{l_o} = 0.1, l = .6cm$, the predicted Sartorius stress is $25.4\frac{N}{cm^2}$

Along with the similarity between the predicted and actual muscle stress values for the Sartorius, the estimated values for moment arms and physiological cross-sectional areas are well within the range of both known parameter values and agree (to first order) with the values that would be expected from visual inspection of these hindlimb muscles. However, because the actual physiological values for the estimated parameters are unavailable for the bullfrog at this time, this argument based on the qualitative anatomical correspondence and similar parameter ranges is far from rigorous. One particular value which needs to be verified is the estimated moment arm value for biceps femoris at the hip, since it was $2.4cm$, slightly over twice as high as any other muscle moment arm in the model.

Chapter 4

Plant Model Assessment

In this chapter we demonstrate the performance of the model presented in Chapter 2 with the parameter values obtained via the algorithm described in Chapter 3. Throughout this section, the results presented are those obtained when the model input's were the filtered EMGs, $\mathbf{m}_{actual}(t)$. Surprisingly, as mentioned in Chapter 3, the estimation results using both PCSA and MIF ratios yielded qualitatively similar results (explained by the similarity between PCSA and MIF values in Table 3.1). Therefore, for brevity, this section only presents the results obtained when utilizing the PCSA ratios.

4.1 Reproduction of Recorded Kinematics

Figures 4-1 through 4-4 illustrate the similarities between the actual joint kinematics, $\mathbf{\Theta}_{actual}(t)$, and those predicted by the model, $\mathbf{\Theta}(t)$, when the model was driven with the filtered EMGs, $\mathbf{m}_{actual}(t)$.

4.1.1 Effect of Raw EMG Filtering

As mentioned in Section 3.2.1, although the filtered and unfiltered EMGs look very different, the resulting kinematics are indeed very similar. Figure 4-5 presents the actual joint kinematics, the model predicted kinematics resulting from the raw EMG,

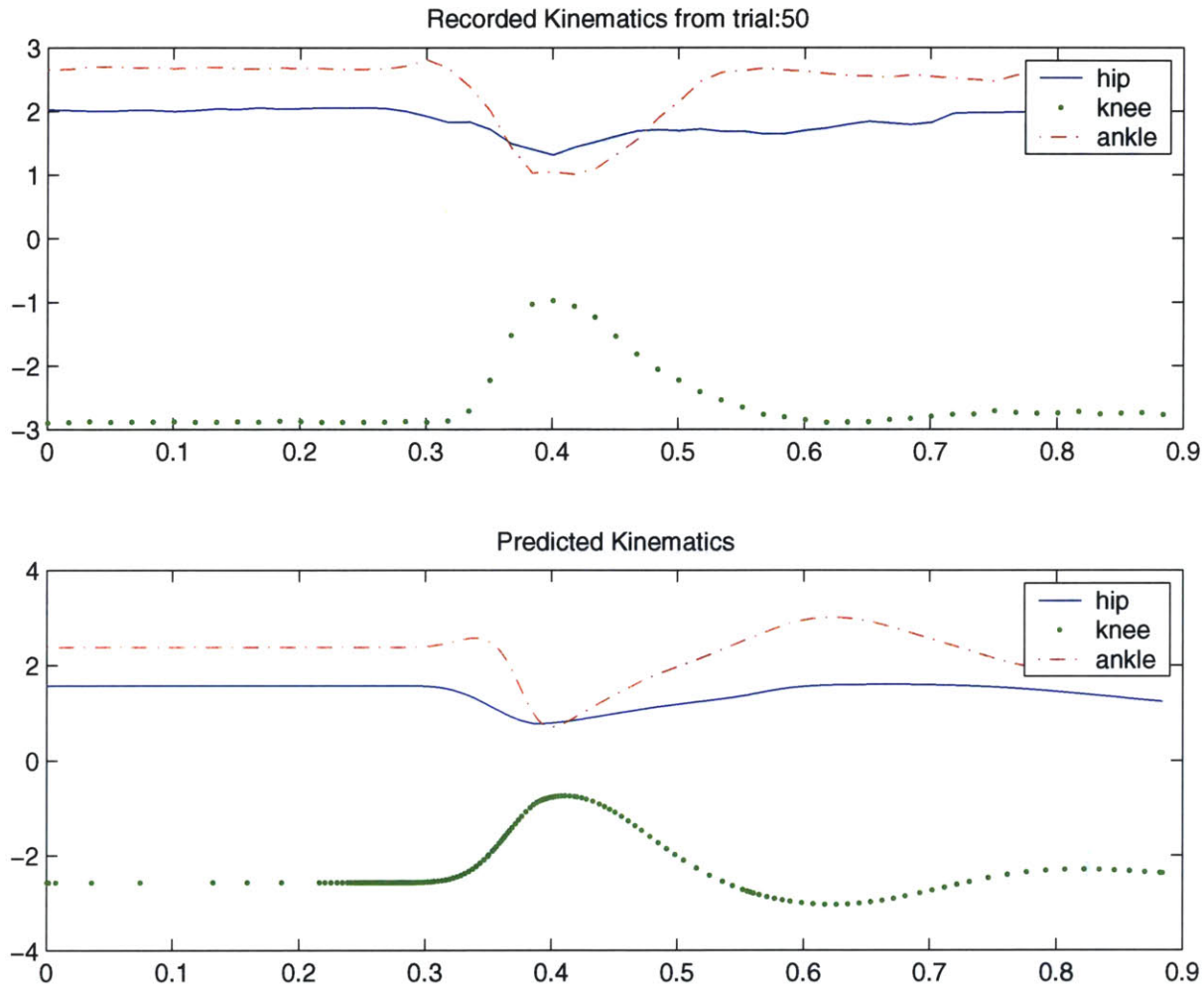

Figure 4-1: Trial 50-Simulated vs. Actual Kinematics.

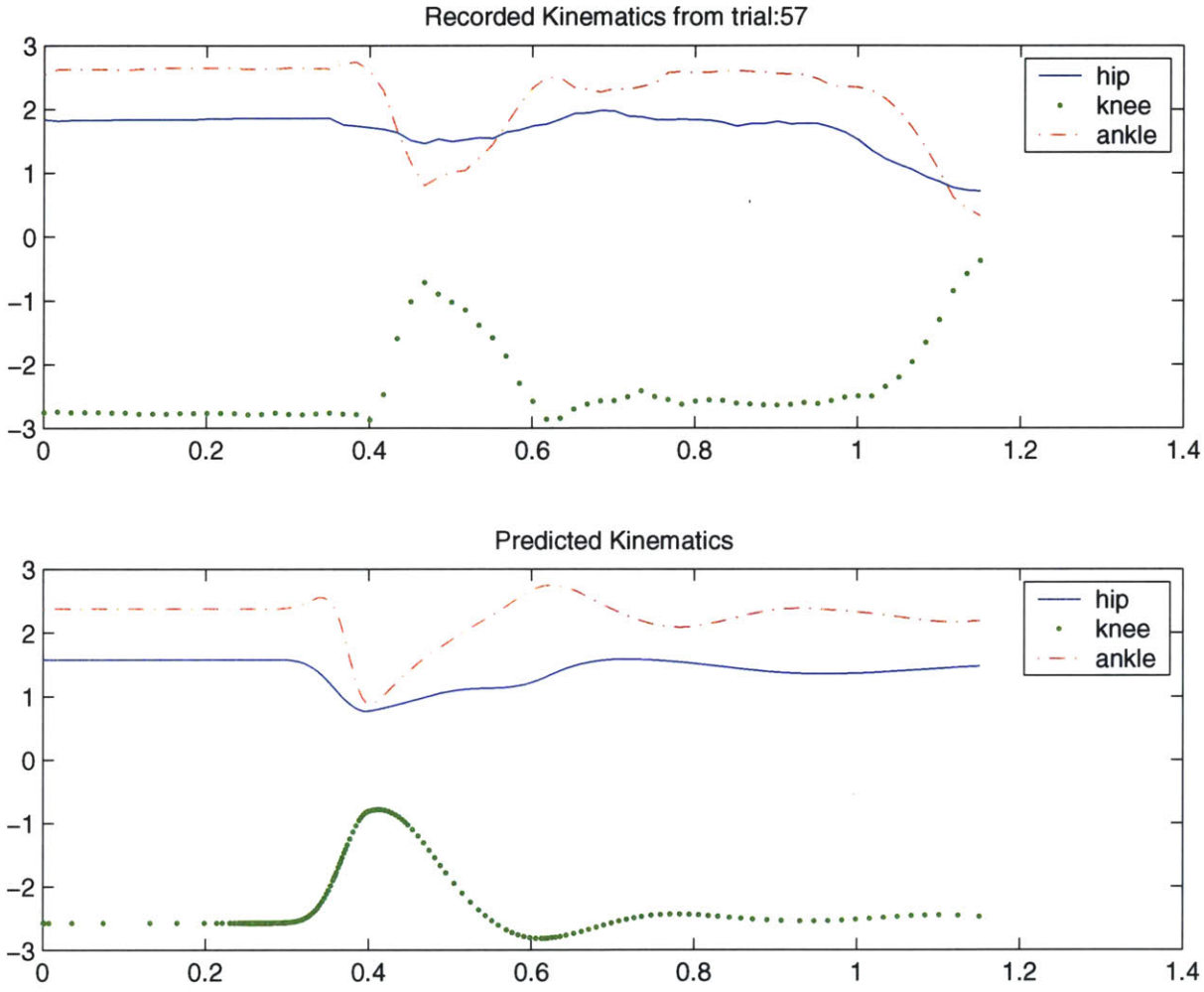

Figure 4-2: Trial 57-Simulated vs. Actual Kinematics.

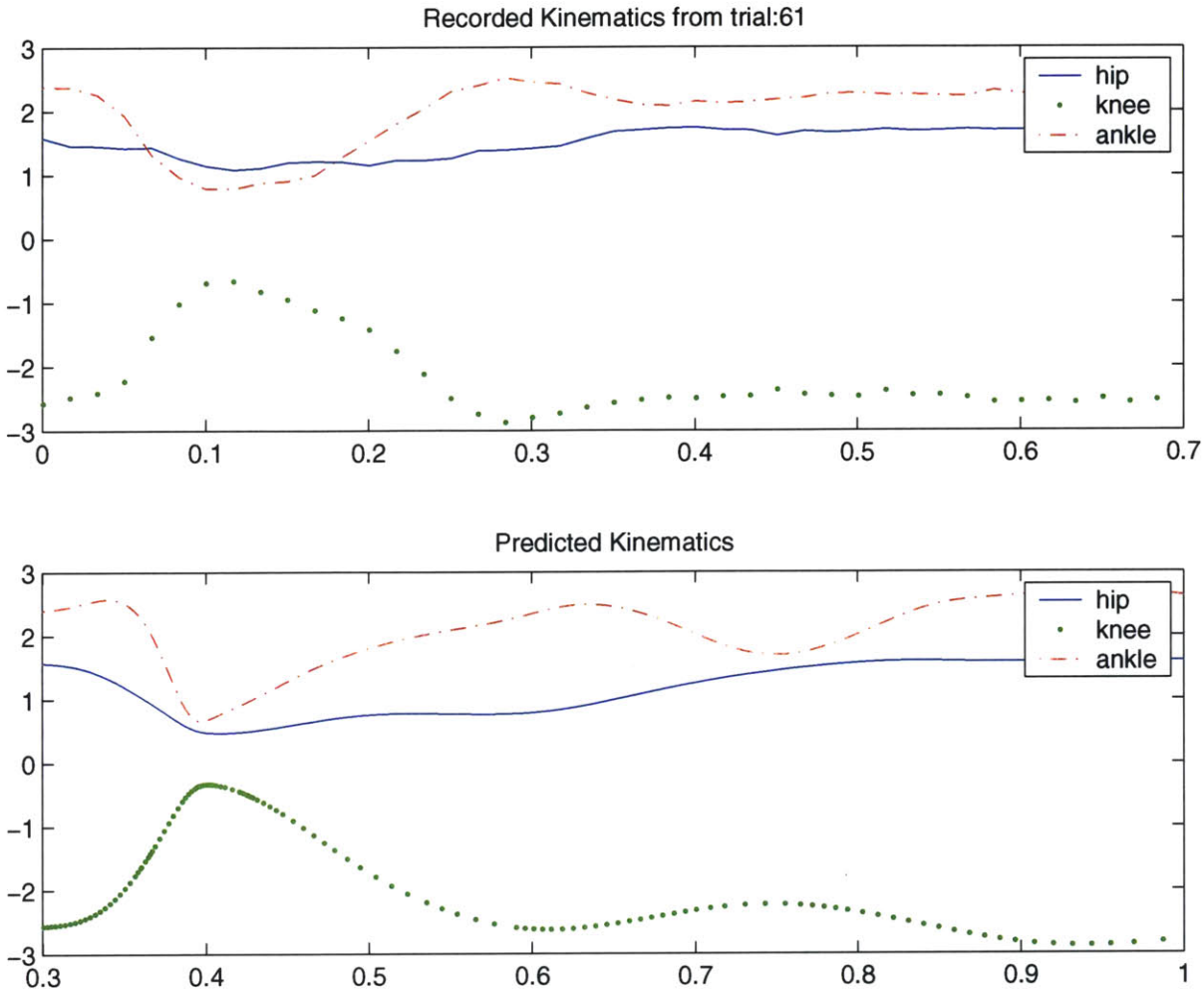

Figure 4-3: Trial 61-Simulated vs. Actual Kinematics. Note that because of the way in which the EMG and kinematic information were recorded for this trial, both images have been aligned manually. However, the signal duration and amplitude are very similar.

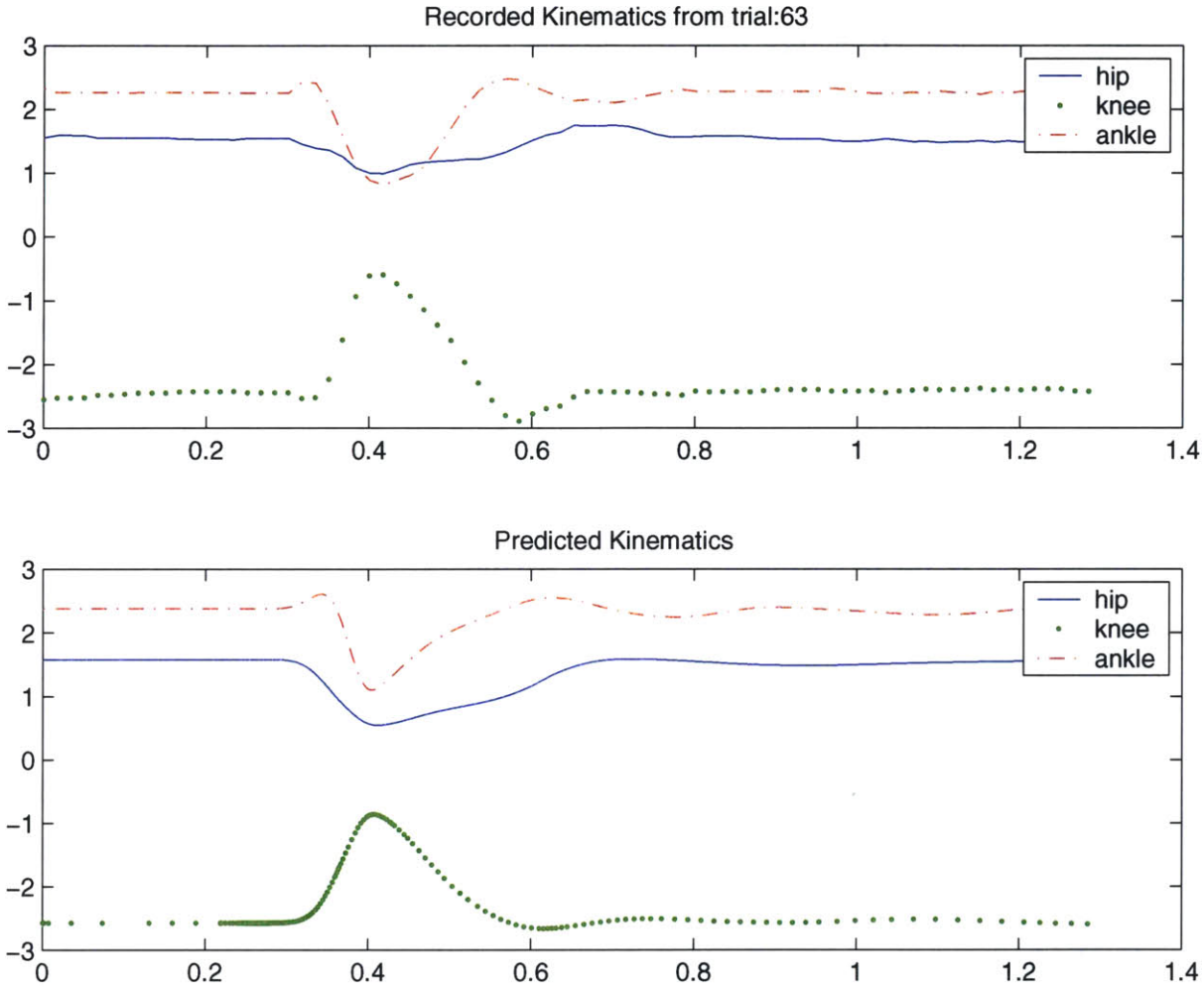

Figure 4-4: Trial 63-Simulated vs. Actual Kinematics

and the model predicted kinematics resulting from the filtered EMG. Both the filtered and unfiltered EMGs produce very similar joint kinematics. The largest qualitative difference between the two is the time-shift arising from the fifth-order butterworth filter (so that the unfiltered signal produces the kinematics slightly earlier than the filtered kinematics). The reason why the kinematics arising from the unfiltered EMG appear to lead the actual kinematics is that the raw EMGs were manually shifted in time so that the kinematics from the filtered EMG were aligned with the recorded kinematics. Therefore, the delay between the raw and filtered EMGs results from time-delay induced by the EMG filtering.

The finding that both raw and filtered EMGs lead to the production of similar kinematics suggests that much of the important kinematic information within the EMG is actually encoded within the low frequency components of the EMG. Additionally, the low frequency component of the EMG consists of sets of simple pulse-like signals for each muscle (see Figure 3-1). This shape of the low frequency EMG components will be used in the development of KCS in Chapter 5.

4.2 Ankle Force Fields

In order to compute the passive (no neural activation) isometric ankle force field (*i.e.* the passive stiffness component of the ankle field), we hold the limb fixed at distinct locations of the workspace and sample the restoring joint torques applied by the limbs musculature. Equation (2.6) is then applied to the joint torques, τ, to determine the corresponding ankle forces, $\mathbf{F}$. Figure 4-6 shows a reconstruction of the hindlimb's passive stiffness field about passive equilibrium using this method.

4.2.1 Ankle Forces During Limb Movements

As described in Chapter 2, it is also possible to reproduce the ankle forces generated during limb movement using Equation (2.6). Figure 4-7 demonstrates the computation of ankle forces generated during the kick in Trial 63 (see limb kinematics in

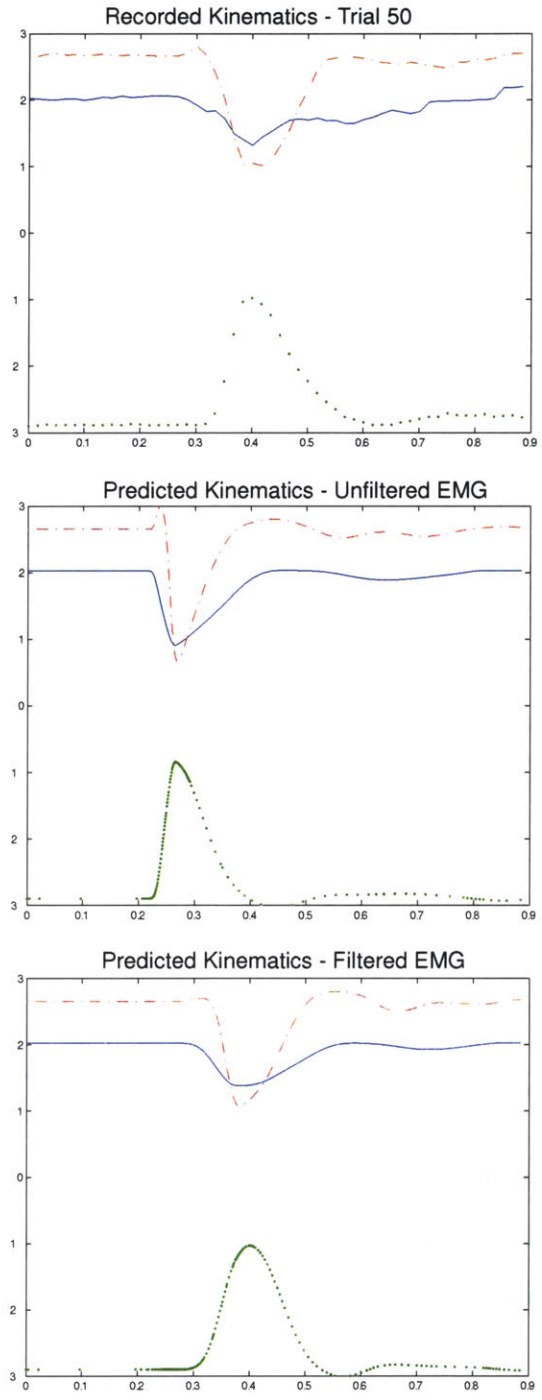

Figure 4-5: Comparison of recorded kinematics to model-generated kinematics using both filtered and unfiltered EMGs. The reason that the kinematics arising from the unfiltered EMG appear to lead the actual kinematics is that the raw EMGs were manually shifted in time so that the kinematics from the filtered EMG were aligned with the recorded kinematics.

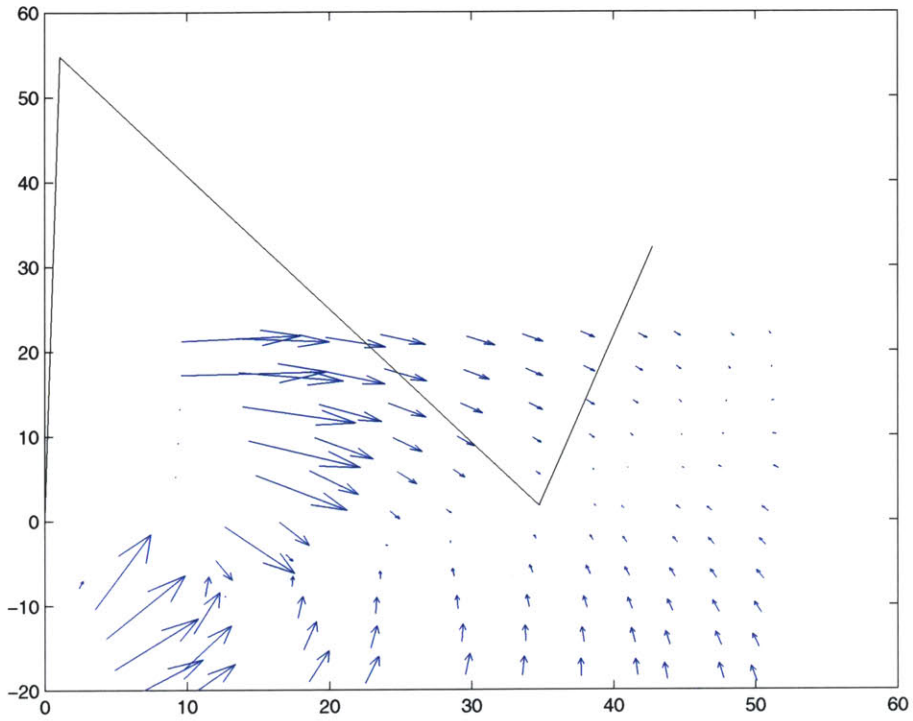

Figure 4-6: Reconstruction of the ankle's stiffness field using Equation (2.6). The frog hindlimb is shown at its equilibrium position determined by limbs' starting position in the recorded joint kinematics, $\mathbf{\Theta}_{actual}(t)$).

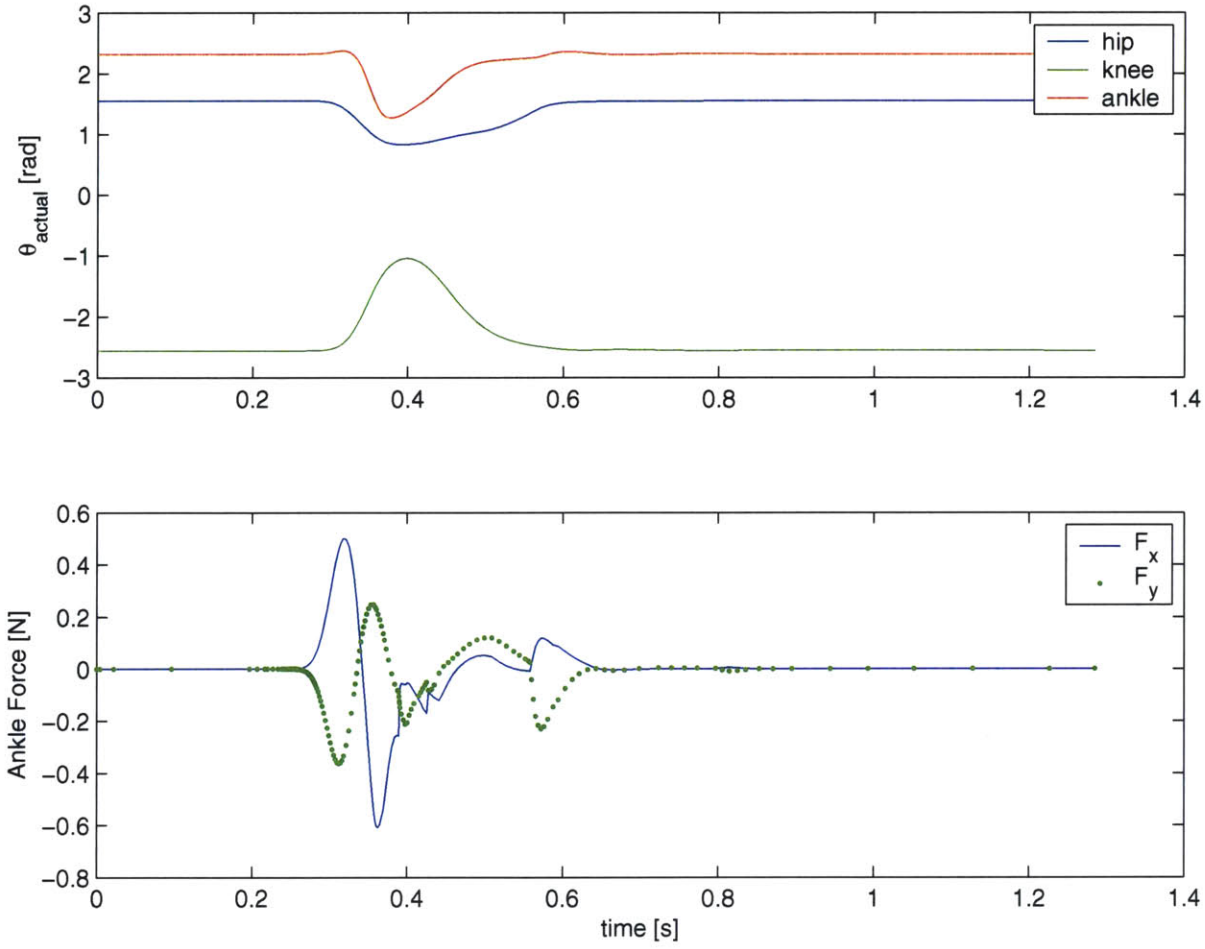

Figure 4-7: Computation of ankle forces generated during a kick (Trial 63)

Figure 4-4). An important feature of Figure 4-7 is that, as noted in [31], the ankle forces generated by the frog rarely exceed $2N$. For this particular kick, the ankle forces do not even exceed $.6N$.

4.2.2 Muscle Synergy Force Fields

In Chapter 1 it was pointed out that each muscle synergy vector has an associated ankle force field given by either Equation (4.1) or (4.2) depending on whether the mapping from EMG to muscle force was approximately linear. In the case that the mapping is linear, the ankle force field can be computed as

$$\mathbf{F}(x,y,t) = \mathbf{J}(\boldsymbol{\Theta})^{\top -1}\mathbf{M}(\boldsymbol{\Theta})\boldsymbol{\Gamma}'\mathbf{W}\mathbf{c}(t) \tag{4.1}$$

where $\boldsymbol{\Gamma}'$ is the linear operator relating muscle EMGs to muscle force, represented here by its equivalent matrix. Alternatively, if the mapping is experimentally found to be nonlinear, the ankle force field can be computed as

$$\mathbf{F}(x,y,t) = \mathbf{J}(\boldsymbol{\Theta})^{\top -1}\mathbf{M}(\boldsymbol{\Theta})\boldsymbol{\Gamma}_{exp}(\mathbf{W}\mathbf{c}(t)) \tag{4.2}$$

where $\boldsymbol{\Gamma}_{exp}$ is now the experimentally derived mapping between $\mathbf{m}(x,y,t)$ and $\mathbf{F}(x,y,t)$. Because at this time it is not known whether the mapping between EMG and muscle force is indeed approximately linear, results pertaining to both types of transformations will be presented here. In fact, recalling our discussion in Chapter 2, it is quite likely that the mapping is indeed nonlinear (see Hill Model Force-Length-Velocity curve in Figure 2-4). Then, the most likely reason why ankle forces where found to scale linearly with spinal activation in [31] is due to a small range of activation levels tested. Further experiments will be required to establish whether the linearity of muscle force field scaling with activation holds for larger values of spinal activations. However, if such experiments demonstrate that force fields still scale linearly with spinal activation over the entire physiological range, it would be suggested that spinal networks are linearizing the mapping from spinal activation to muscle force.

As will be seen in the following sections, a nonlinear mapping will, in general, cause the ankle force field vectors to change orientation as a function of activation – a result inconsistent with the findings of invariant force fields by Giszter *et al.* in [13]. However, in this case, the resulting force fields will be convergent. If $\boldsymbol{\Gamma}'$ is linear, however, it will be shown that the resulting force field shapes are indeed activation invariant and scale linearly with activation as observed by Giszter *et al.*, yet not convergent. These points will be discussed further in Chapter 6.

Nonlinear EMG to Force Mapping

Figure 4-8 demonstrates the results of treating the mapping from EMG to muscle force as a nonlinear one. We represent this mapping by the full equation describing the muscle contractile element in our muscle model. That is,

$$F^m(act, l, \dot{l} = 0) = F^{ce}(act, l, 0) = K_{ce} act \lfloor C_{atl} act - (l_o - l) \rfloor_+ \tag{4.3}$$

where the viscosity terms are neglected because the ankle is held fixed at each workspace location where the force field is being computed. Also, the passive force component is not included in order to make these fields equivalent to the *active* force fields described by Giszter *et al.* in [13]. Lastly, because the limb is not in motion, $\mathbf{act}(t) = \mathbf{m}(t)$, as a result of the unity DC (s=0) gain of the EC filter.

Figure 4-10 demonstrates that the force fields arising from Equation (4.3) actually change orientation as a function of activation, while Figure 4-9 demonstrates that each of the fields has a convergent equilibrium point. The location of this equilibrium point depends on the magnitude of *act*, while the amplitude of the force fields scales as the square of *act*. For very high levels of *act* (such as in Figure 4-8) the equilibrium point has moved so far from passive equilibrium that the fields begin to look like parallel fields.

Linear Mapping

Figure 4-11 shows the force fields corresponding to each of the seven synergies, w_i, when the mapping from EMG to muscle force is represented as linear. For this linear mapping we use,

$$\mathbf{F}^m(act) = \mathbf{F}^{ce}(act) = \mathbf{K}_{ce} C_{atl} \mathbf{act} = \mathbf{\Gamma}' \mathbf{act} = \mathbf{\Gamma}' \mathbf{m} \tag{4.4}$$

where both the contractile element length dependance, and the second order term in *act* have been neglected. When $\mathbf{\Gamma}'$ is represented as such a linear transformation, the shape of the force field remains invariant with synergy activation. Increased activation only causes a linear increase in the magnitude of the force field vectors,

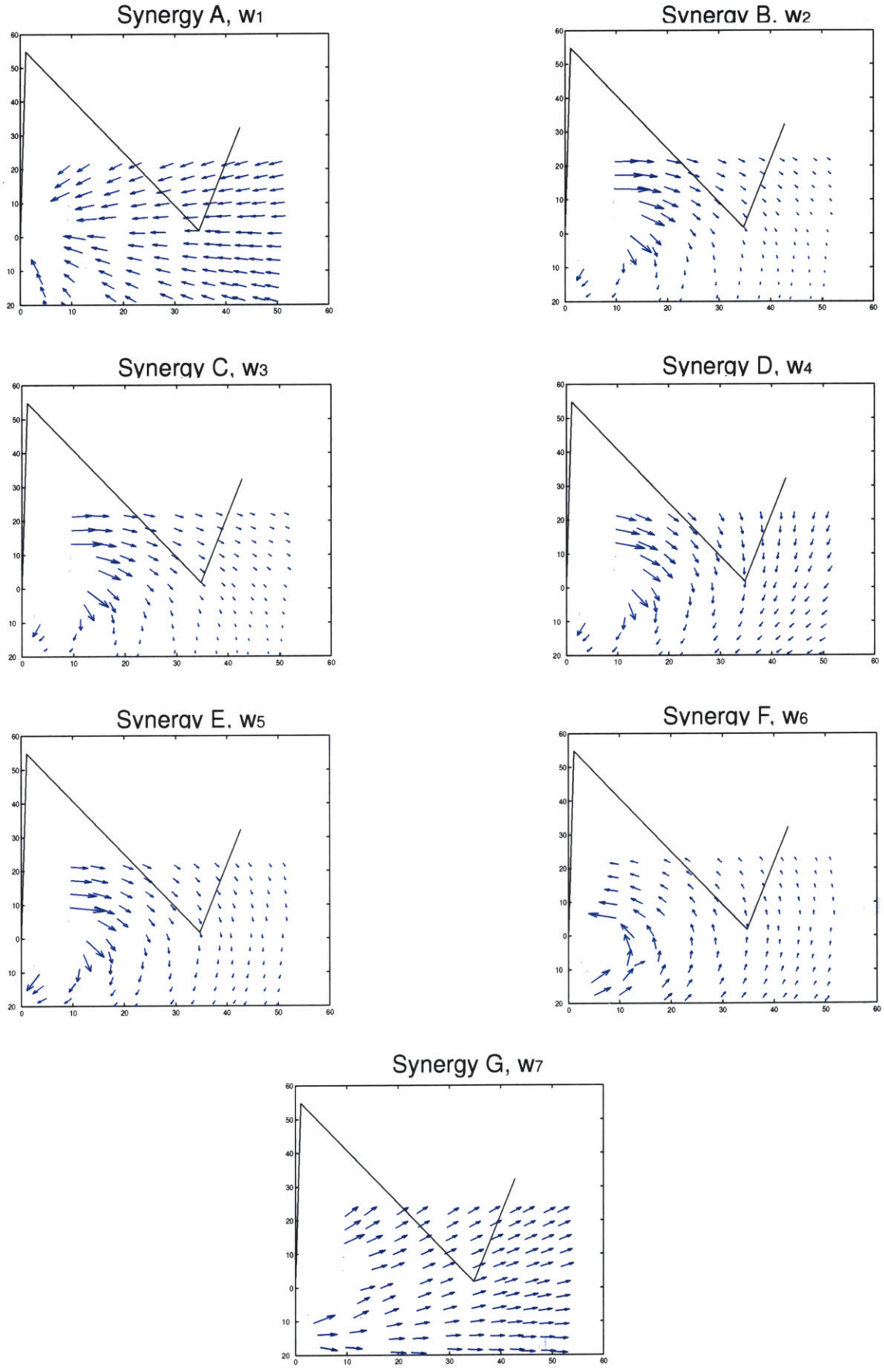

Figure 4-8: Computation of ankle force field primitives arising from each muscle synergy. The mapping from EMG to muscle force was computed with Equation (4.1). Each synergy was activated to its maximum ($c_i(t) = 1$) for the force fields seen here.

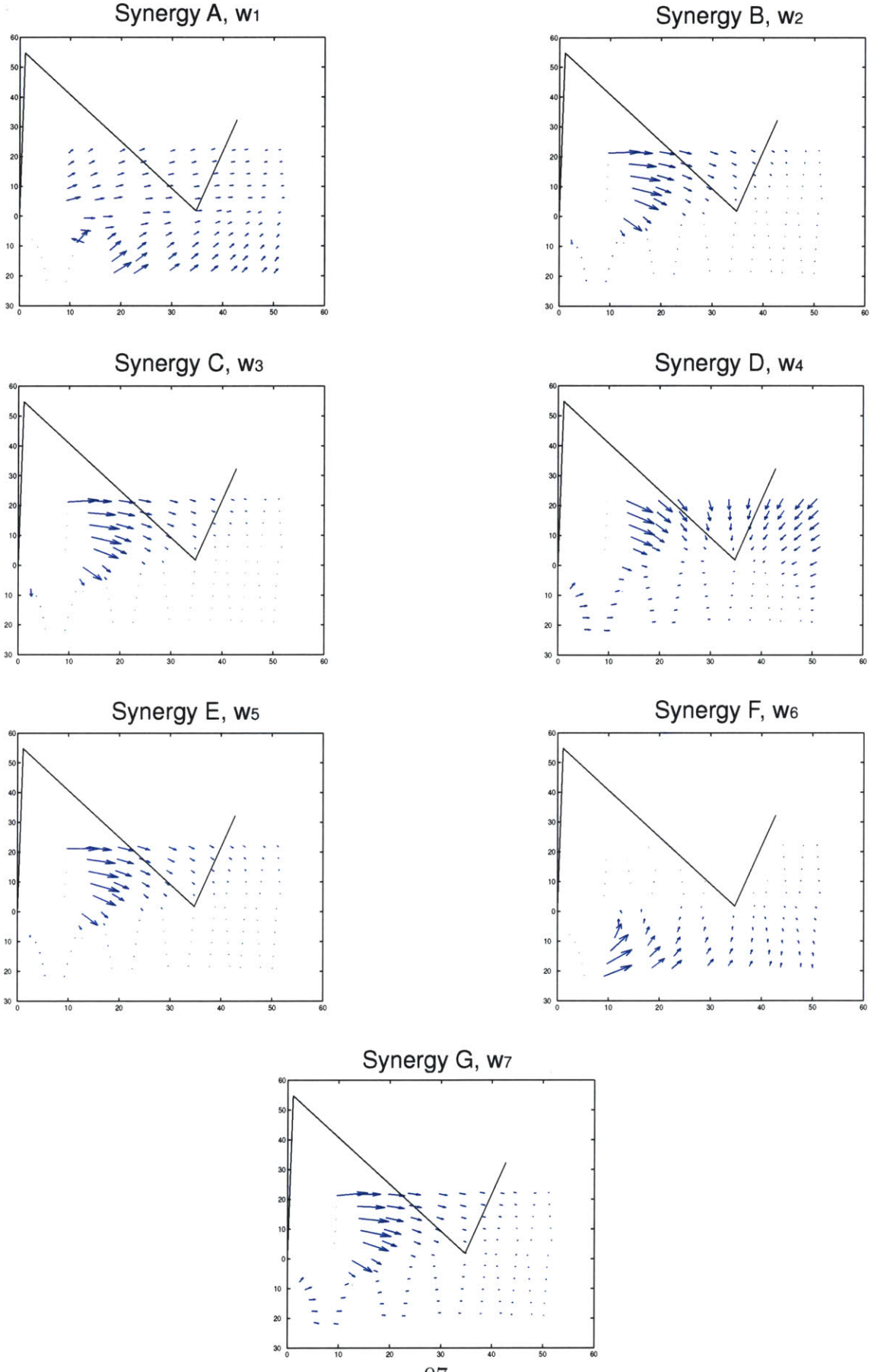

Figure 4-9: Muscle synergy primitive force fields computed with Equation (4.3) show a fixed position which begins at passive equilibrium when act=0, and moves as act is increased. $c_i(t) = .01$ for the fields shown here.

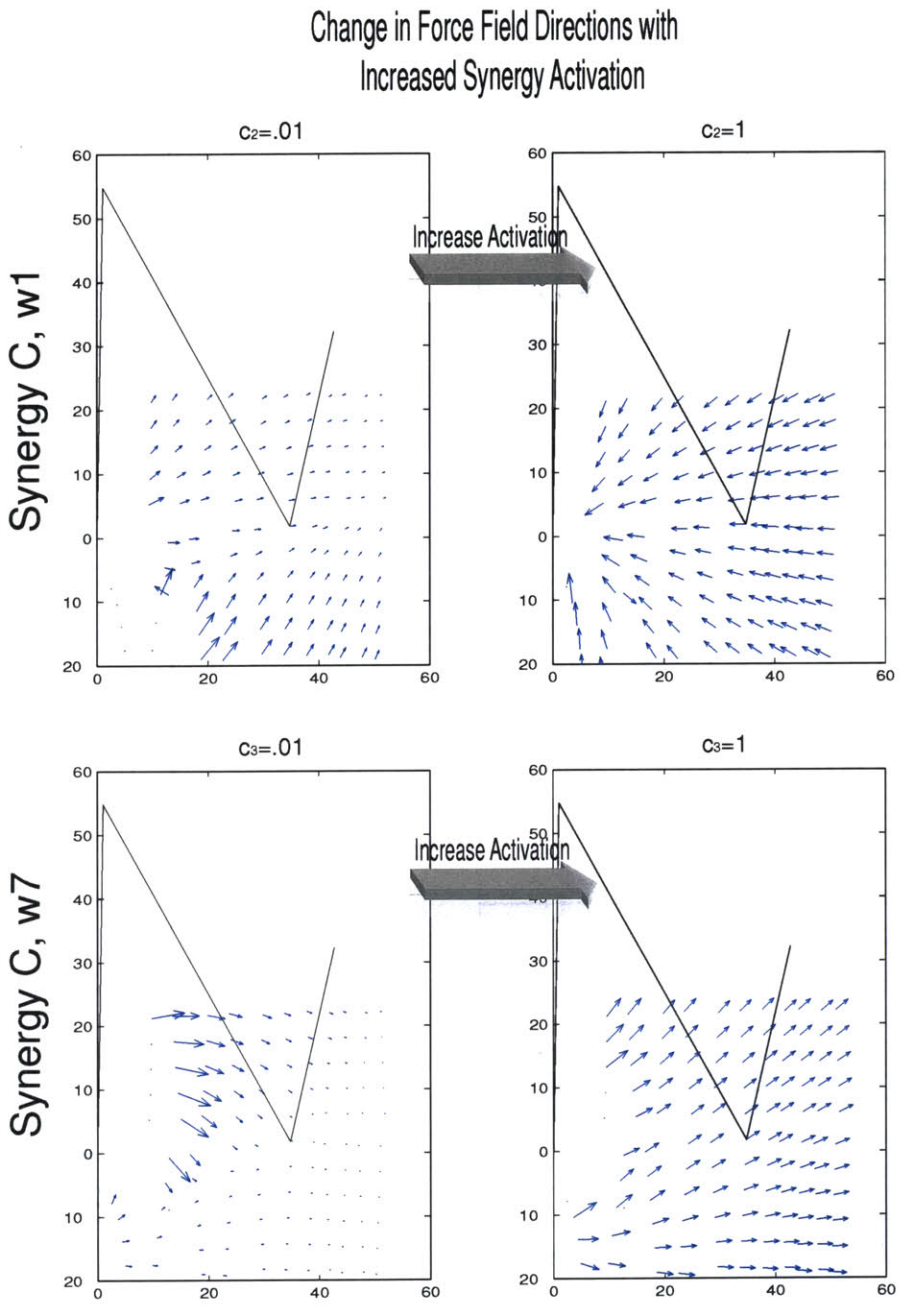

Figure 4-10: The nonlinear relation between synergy activation and ankle forces causes the ankle force field vectors to change direction as the level of activation is increased. This is due primarily to the activation dependant scaling of the contractile element stiffness in Equation (4.3).

and no net change in the orientation of the force field vectors. Each synergy was activated to its maximum ($c_i(t) = 1$) for each of the force fields in Figure 4-11. Although the force fields in Figure 4-11 are consistent with both the magnitude scaling and orientation invariance properties observed by Giszter *et al.*, they do not show a convergent equilibrium point for any level of activation.

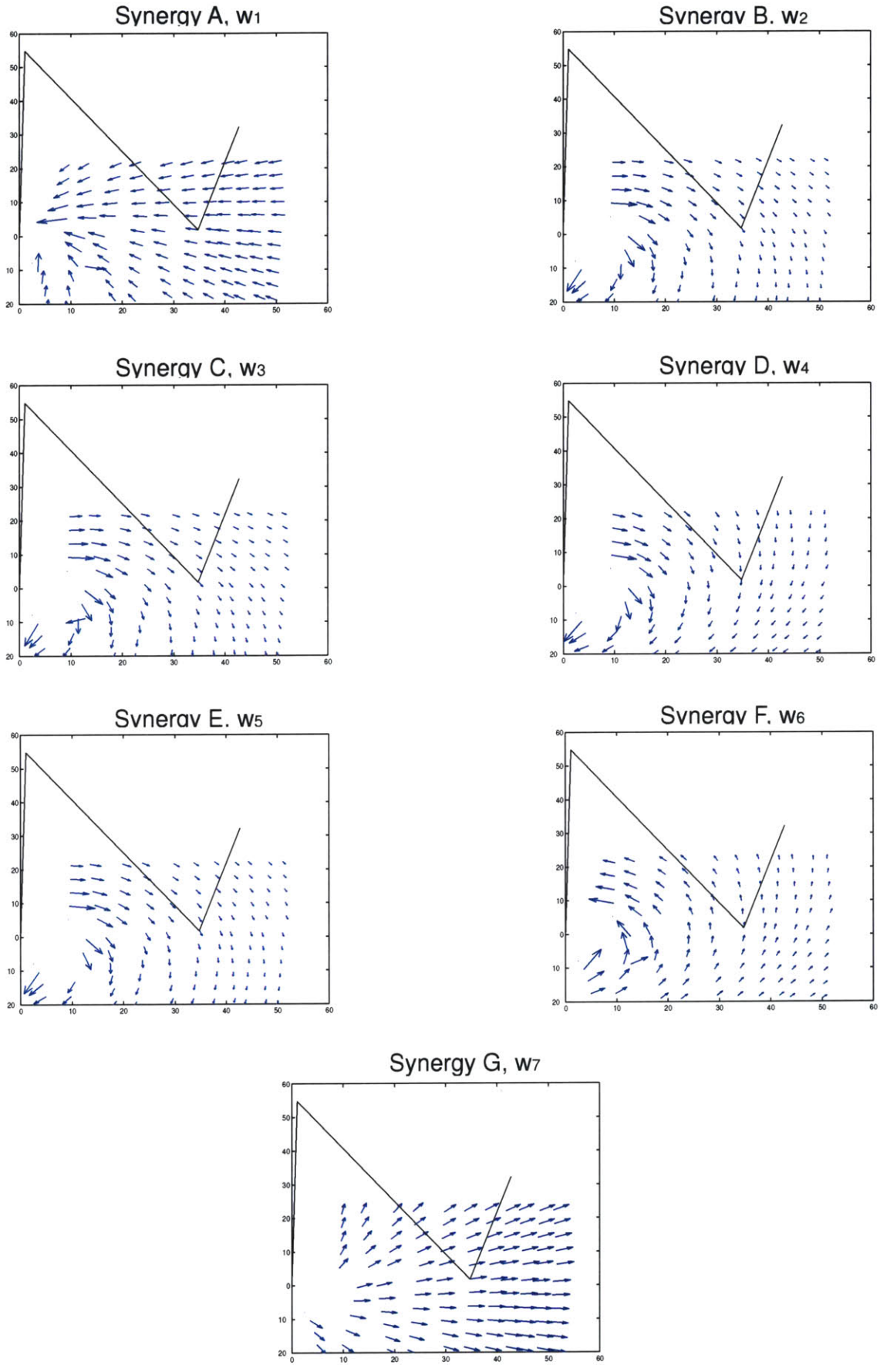

Figure 4-11: Computation of ankle force field primitives arising from each muscle synergy. The mapping from EMG to muscle force was computed with Equation 4.4

Chapter 5

Kinematic Control Synergies

In this Chapter, we demonstrate the control benefits of reorganizing the muscle synergies set derived in [36] into synergistic groups with simple, orthogonal kinematic functions. Subsequently, we present a linear optimization whereby these Kinematic Control Synergies (KCS) can be obtained, and illustrate the synthesis of a few typical ranine behaviors as simple linear combinations of these control synergies. Reorganization of muscle synergies into these KCS (or a similar reorganization) by spinal interneurons would be potentially beneficial from a control perspective for two reasons. First, it would allow for the specification of movement in terms of the movement goals (*i.e.* specification of what the limb should do, not how it should do it). Second, incoming sensory information (in world coordinates, such as detection of an obstacle) could be used by the spinal cord to directly recruit a KCS which will move the limb away from the obstacle.

5.1 Functional Hindlimb Control

Although the muscles synergies identified by Saltiel *et al.* effectively constitute a basis for the space of all EMGs producible by the bullfrog, the kinematic effects of two synergies may be similar, while others may not be particularly useful for controlling certain types of movements (although possibly useful for others!). Given that the hindlimb of the bullfrog is constrained to the horizontal plane in our model, we seek

the simplest reorganization of the Saltiel *et al.* synergies that will allow the formation of a wide range of behaviors within this constrained workspace. Additionally, we impose the constraint that these reorganizations should allow for the control signals to be specified in terms of functional kinematic goals, instead of individual muscle activations.

From a limb control perspective, it is precisely this type of representation that is required if movement is to be coordinated from linear combinations of muscle synergies within the spinal cord. For instance, if the frog wanted to produce a caudally directed wipe, which muscle synergies would it need to activate, in what ratios, and during which movement phases? Alternatively, if a neuroprosthetic device were being designed to actively control the hindlimb, which muscle groups would it need to activate in order to reproduce a caudally directed wipe in a natural fashion? In order to answer such questions it becomes necessary to look at the muscular synergies in the context of the entire spinal/musculoskeletal system. Such an approach is essential because information such as relative muscle strengths, moment arms, and muscle stiffness and viscosities are completely absent from the muscle synergy representation due to the manner in which the synergies were obtained (through the characterization of produced EMG arising from spinal stimulation). By viewing the Saltiel *et al.* synergies in terms of their kinematic functions, it will become possible to obtain the representation we seek.

An optimization algorithm is developed in order deduce a reordering of the Saltiel *et al.* synergies in terms of their kinematic function, and demonstrate the utility of these KCS in movement formation. If a kinematic decomposition of the muscle synergies could be obtained, it would seem most beneficial for the decomposition to yield synergies whose kinematic effects are orthogonal in workspace coordinates. We believe that such an orthogonal decomposition of spinal muscle synergies would be advantageous for higher-level movement formation for a number of reasons. First, an orthogonal control basis in workspace coordinates would allow for the simple forma-

tion of behaviors. To illustrate, suppose that it was possible to recombine the available muscular synergies into groups that controlled the azimuthal angle and radial extent of the hindlimb. Such a polar representation of the workspace would reduce the control of a multi-joint limb to the specification of only two control signals (compared to seven individual synergy drives, or twelve individual muscle drives) that are directly related to the desired kinematic role.

Second, an orthogonal kinematic decomposition of the spinal muscle synergies would present a simple mechanism for behavioral learning whereby kinematic error in workspace coordinates (from sensory afferents) could be used (as real-time feedback) to correct errors that arise in the movement while it is being performed. In addition, since the kinematic error and the control synergies would be in the same coordinate system, it would become possible to use the error information to tune the interneurons responsible for movement formation (*i.e.* learning the appropriate interneuronal weights to perform a movement correctly). If an executed movement resulted in an overshoot of the desired azimuthal angle of the limb, for example, the synapse strength of the interneurons controlling the azimuthal angle could be reduced to decrease future overshoot errors.

5.1.1 Formulation of Linear Optimization

Motivated by the above discussion, we describe a method in which an orthogonal recombination of the Saltiel *et al.* muscle synergies can be found. Specifically, we seek a decomposition that allows for the specification of a single vector summarizing the desired limb behavior,

$$\mathbf{b}(t) = \begin{pmatrix} b_{hipflex}(t) \\ b_{hipextend}(t) \\ b_{radialflex}(t) \\ b_{radialextend}(t) \end{pmatrix} \tag{5.1}$$

where $b_{hipflex}(t)$ specifies the desired amount of hip flexion, $b_{hipextend}(t)$ the amount of hip extension, $b_{radialflex}(t)$ the amount of radial hindlimb flexion, and $b_{radialextend}(t)$

the amount of radial extension. Note that these four signals specify the desired behavior of the limb in polar coordinates. Because muscles activation signals are required to be positive, we require four activation signals instead of two to fully describe the polar coordinate position of the limb. These signals would be used to specify the limb's displacement about its passive equilibrium position.

Recalling from Chapter 2 that the muscle forces are related to the muscle torques via the moment arm matrix, $\mathbf{M}$, as

$$\tau = \mathbf{M}\mathbf{F}^m \tag{5.2}$$

and substituting Equation (2.9) into 5.2, we obtain

$$\tau = \mathbf{M}\mathbf{K}_{ce}(\mathbf{act})\lfloor C_{atl}\mathbf{act} - (\mathbf{l} - \mathbf{l}_o)\rfloor_+ + \mathbf{B}_{cv}(\mathbf{act})\lfloor \dot{\mathbf{l}}\rfloor_+ \tag{5.3}$$

$$\tau = \mathbf{M}\mathbf{K}_{ce}(\mathbf{act})\lfloor C_{atl}\mathbf{act} - (\mathbf{l} - \mathbf{l}_o)\rfloor_+ \tag{5.4}$$

Equation (5.4) is obtained by neglecting transient viscous effects. Note that the multiplicative activation dependance of $\mathbf{K}_{ce}$ from Equation (2.9) is implicitly shown by making $\mathbf{K}_{ce}$ a function of activation. It follows that, focusing on the component of muscle force due to neuromuscular activation and imposing the constraint that $act = \mathbf{W}\xi$, we obtain

$$\tau = \mathbf{M}\mathbf{K}_{ce}C_{atl}(\mathbf{W})^2(\xi)^2 \tag{5.5}$$

where $()^2$ implies element-wise squaring of each of the elements of the matrix or vector. Here $\mathbf{W}$ is the matrix whose columns are the seven synergies in Table 2.4, and ξ represents the corresponding combination of the muscular synergies that yields the desired vector of joint torques. The squaring of the elements of $\mathbf{W}$ is required because of the nonlinear dependance of muscle force on neuromuscular activation.

Using the above equations, the problem of obtaining the desired KCS is then reduced to finding the vectors, ξ_i (note that ξ points in the same direction as ξ^2), that yield torques corresponding to pure hip flexion ($\tau_i = [1 \quad 0 \quad 0]^\top$), hip extension ($\tau_i = [-1 \quad 0 \quad 0]^\top$), radial flexion($\tau_i = [0 \quad -1 \quad 0]^\top$), and radial extension

($\tau_i = [0 \quad 1 \quad 0]^\top$). These torque values were chosen because they would yield motions in the required directions. This problem could also be formulated in terms of obtaining a set of desired joint angular acceleration directions, $\ddot{\mathbf{\Theta}}$, instead of joint torques. If $\ddot{\mathbf{\Theta}}$ was the control parameter of interest, Equation (5.5) would be preceded by $\mathbf{H}^{-1}$, the inverse of the system inertia matrix. Using torque as the desired control variable, the problem can be formulated as the following linear optimization problem:

$$\xi_i = \min_{\mathbf{v}}(\tau_i - \mathbf{M}\mathbf{K}_{ce}C_{atl}(\mathbf{W})^2\mathbf{v}) \tag{5.6}$$
$$s.t. \qquad 0 \leq \mathbf{W}\xi_i \leq 1$$

where the linear constraint on ξ_i arises from the fact that we constrain the neuromuscular activations, *act* (and EMG, $m(t)$) to be $\in [0, 1]$.

Performing the optimization in Equation (5.6) and defining the control synergies as

$$\mathcal{K} = \mathbf{W}[\xi_{hipflex} \quad \xi_{hipextend} \quad \xi_{radialflex} \quad \xi_{radialextend}] = \mathbf{W}\xi \tag{5.7}$$

we are able to reorganize the Saltiel *et al.* synergies into four groups (the four columns of $\mathcal{K}$) that control orthogonal directions in hindlimb workspace coordinates. We refer to the columns of the matrix $\mathcal{K}$ as Kinematic Control Synergies (KCS). As a side note, it was found by this same method that there is no combination of muscle synergies which result in the production of EMG but and no net joint torques (*i.e.* $\tau_i = [0 \quad 0 \quad 0]^\top$). A result that suggests that the ability to cocontract (increase stiffness isometrically) at a joint is not possible as a combination of the muscle synergies, w_i.

Figure 5-1 summarizes the ξ_i vectors obtained from the linear optimization in terms of their corresponding synergies ratios. The letters along the horizontal axis correspond to the synergy labels in Table 2.4 and Figure 2-10. It is important to note that the results of this optimization coincide with some of the preferred synergy combinations in [36]. The preferred combinations that resulted from the optimization are ADF (11), ACG (9), and CF (25). The number of times that each combination was

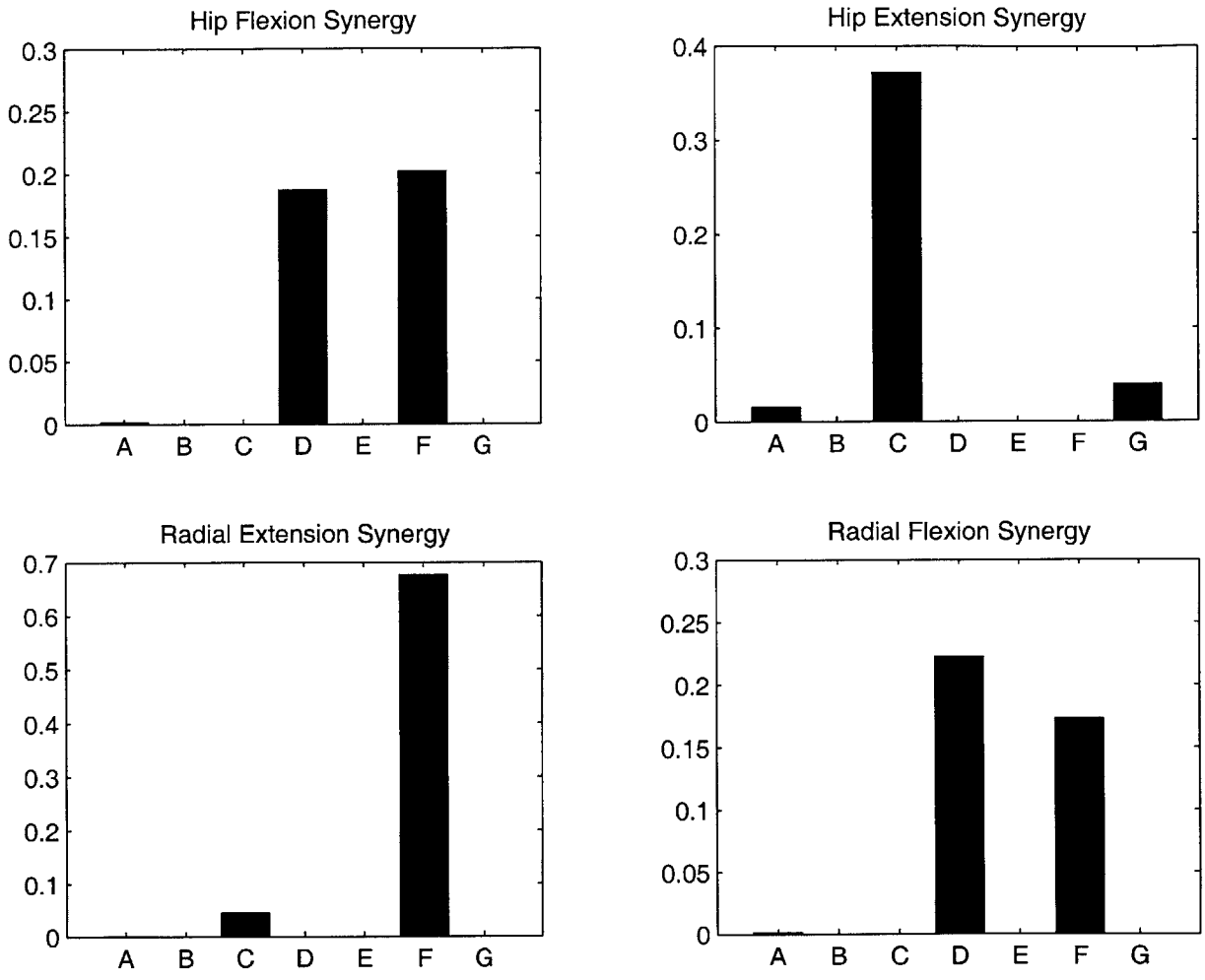

Figure 5-1: Functional Primitives in terms of Saltiel *et al.* Synergies.

observed in [36] is included in parenthesis. Note that ADF combination is used in both hip flexion and radial extension but in slightly different ratios. All of the ratios obtained from the optimization algorithm were observed in [36]. It is also important to note that not all of the seven synergies vectors, w_i, are used to form the KCS. It is therefore likely that these synergies help to control either variations of movements within the horizontal plane, movements out of the plane, or a reorientation of the plane itself.

Using the KCS vectors obtained via the described optimization, it is possible to define the simulated vector of EMG signals, $\mathbf{m}(t)$, in terms of the new descending command vector, $\mathbf{b}(t)$, as

$$\begin{aligned} \mathbf{m}(t) &= \mathbf{u}_{desc}(t) + \mathbf{u}_{reflex}(t) = \mathbf{W}[\xi_{hipflex} \quad \xi_{hipextend} \quad \xi_{radialflex} \quad \xi_{radialextend}] \begin{pmatrix} b_{hipflex}(t) \\ b_{hipextend}(t) \\ b_{radialflex}(t) \\ b_{radialextend}(t) \end{pmatrix} \\ \mathbf{m}(t) &= \mathcal{K}\mathbf{b}(t) + \mathbf{u}_{reflex}(t) \end{aligned} \tag{5.8}$$

where $\mathcal{K}$ is the matrix whose columns are the four KCS and $\mathbf{d}(t)$ is the control vector specifying the hindlimb commands in polar coordinates.

5.2 Hindlimb Control using Control Synergies

In this section we illustrate the control benefits of having obtained a orthogonal reorganization of the Saltiel *et al.* synergies by reproducing a variety of typical frog behaviors using a simple set of pulse like control signals as might be generated by brainstem, cerebellum, or spinal locomotive generators.

5.2.1 Kick Reproduction

Because all of the kinematic data available for this study consisted of a wide range of kicks in the horizontal plane, we focus our first example on this type of kinematic

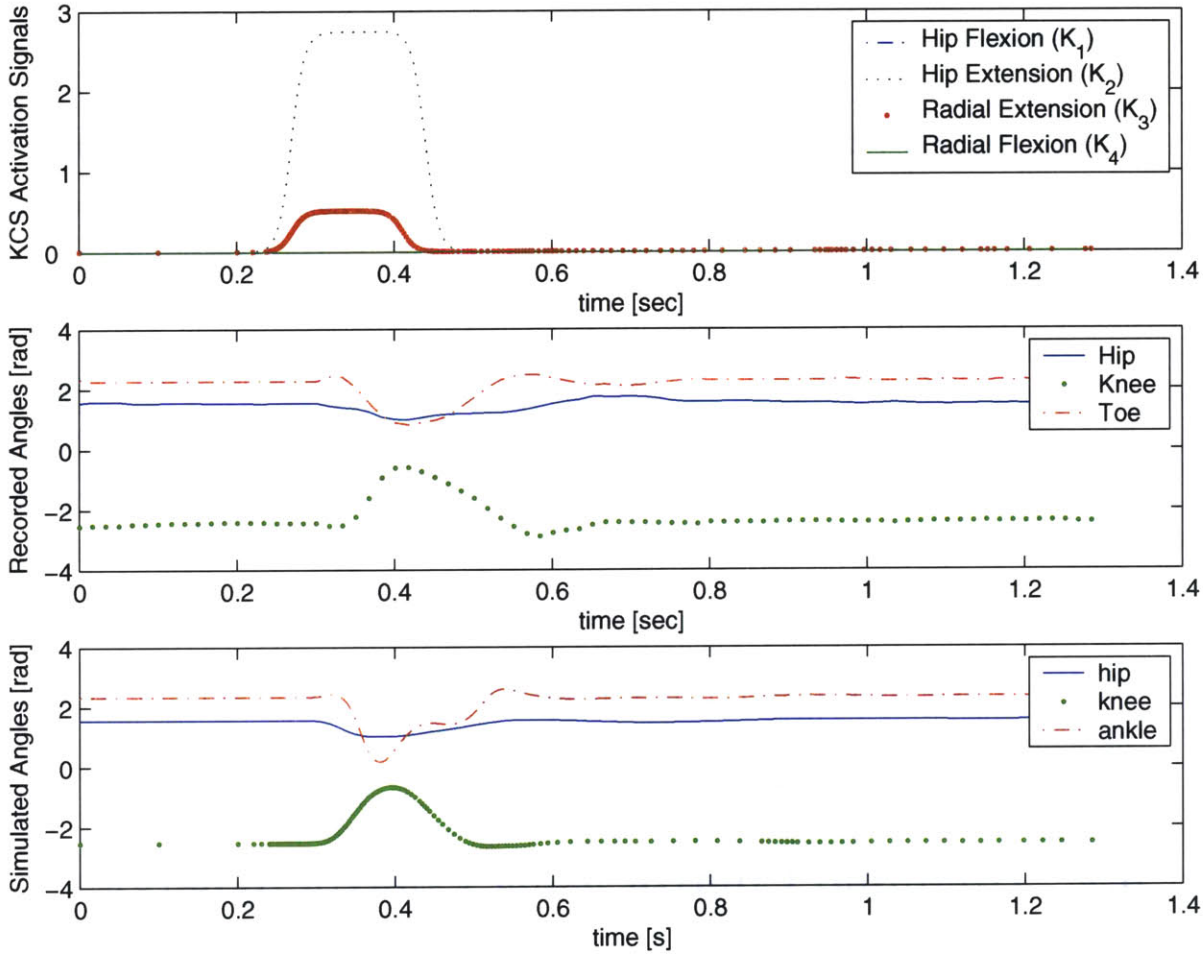

Figure 5-2: Kick Reproduction Using Control Synergies (Trial 63)

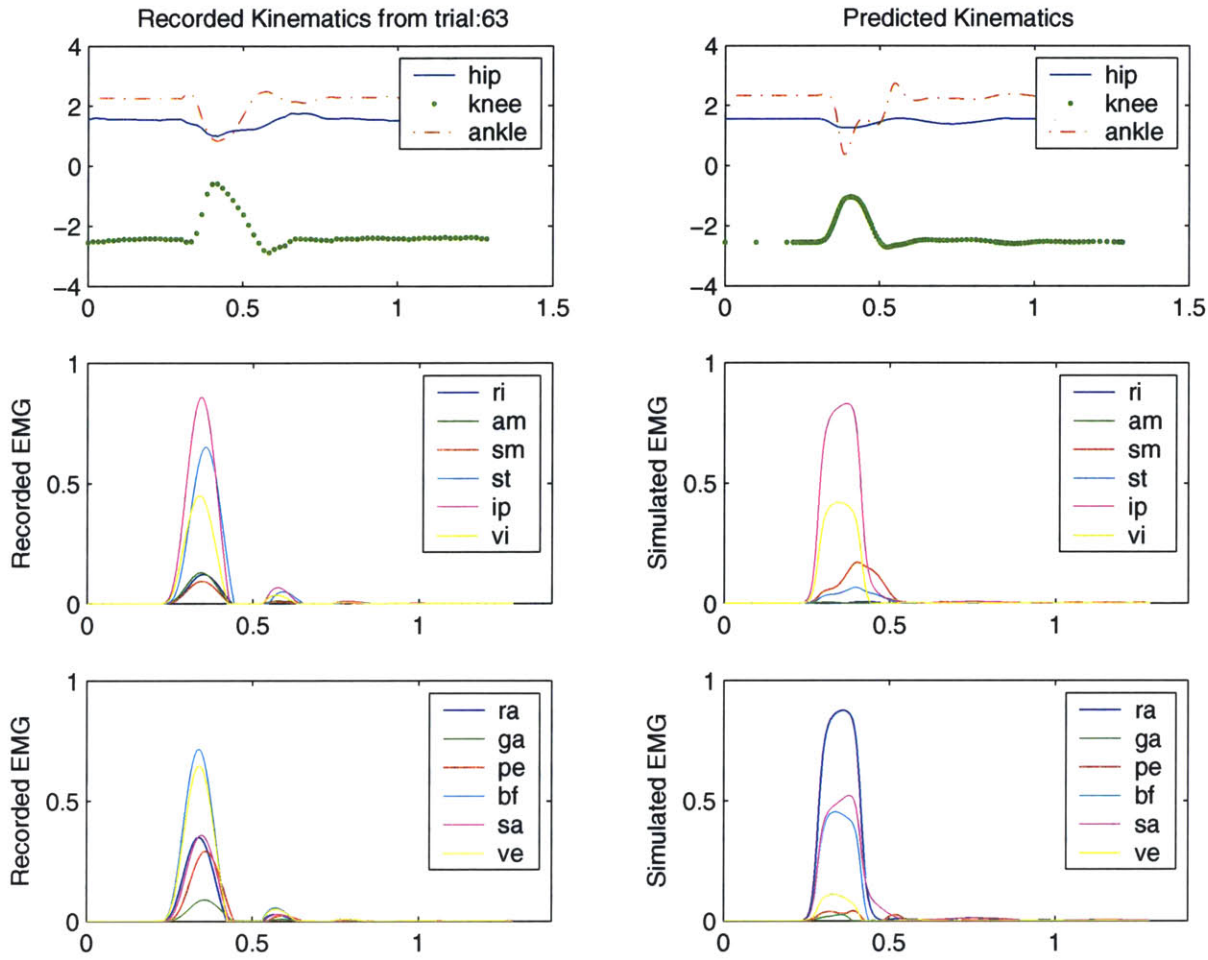

Figure 5-3: Actual vs. Recorded EMGs and Kinematics (Trial63) for the same kick as in Figure 5-2

behavior. Using the control synergies described above, the kick observed in Figure 5-2 was reproduced by activating the radial extension and hip extension synergies. The command signal essentially directed the hindlimb to actively extend radially from passive equilibrium, while the hip was extended slightly to obtain the appropriate kick direction. Once the command signals cease, the hindlimb returns passively to the body.

Figure 5-3 shows both the actual and simulated kinematics and EMGs for Trial 63. Note the similarity between both the EMGs and kinematics between the simulated

and recorded trials. The small secondary burst of EMG in the simulated kick is due to the spinal stretch reflex as the limb draws back towards the body. Because the spindles are no longer being activated by alpha-gamma coactivation, their stretch as the limb draws back to the body causes a small burst of firing to occur. This burst of spindle firing helps the limb settle at its equilibrium position as it passively returns towards the body.

As can be seen in Figure 5-3, both simulation kinematics and EMG line up quite closely with the actual recorded signals. However, there are two major differences between the actual and simulated EMGs. The first is that while the actual EMG has a large component of ST activation, the simulated EMG does not. Given the similarity between the two kicks it is quite possible that the small extra activation of SM in the simulated kick is able to compensate for the absence of ST activation. That is, because the two muscles are quite similar (in both size and mechanical action), it is possible that one redundant muscle performs the function of the other. This discrepancy between actual and simulated EMGs is not surprising given the number of similar muscles included in the model, although it might suggest that future models deal with redundant muscle by combining them into one equivalent muscle. Combining muscles in this fashion may have predicted the correct EMG level for the aggregate ($SM + ST$) muscle.

The second difference between the EMGs is that while VE is very strongly activated in the actual EMG, it is minutely recruited in the simulated kick. Accordingly, it appears that two other kinematically redundant muscles, RA and SA, are activated at a higher intensity. This slightly higher activation of VE and SA apparently compensate for the absence of VE in the simulated EMG because the resulting kinematics are very similar. Again, the finding that one redundant muscles is activated more or less than observed is not surprising given that a description of how muscles are recruited is not included within our model. Physiologically, kinematically redundant muscles have a number of important differences that may lead to their preferential

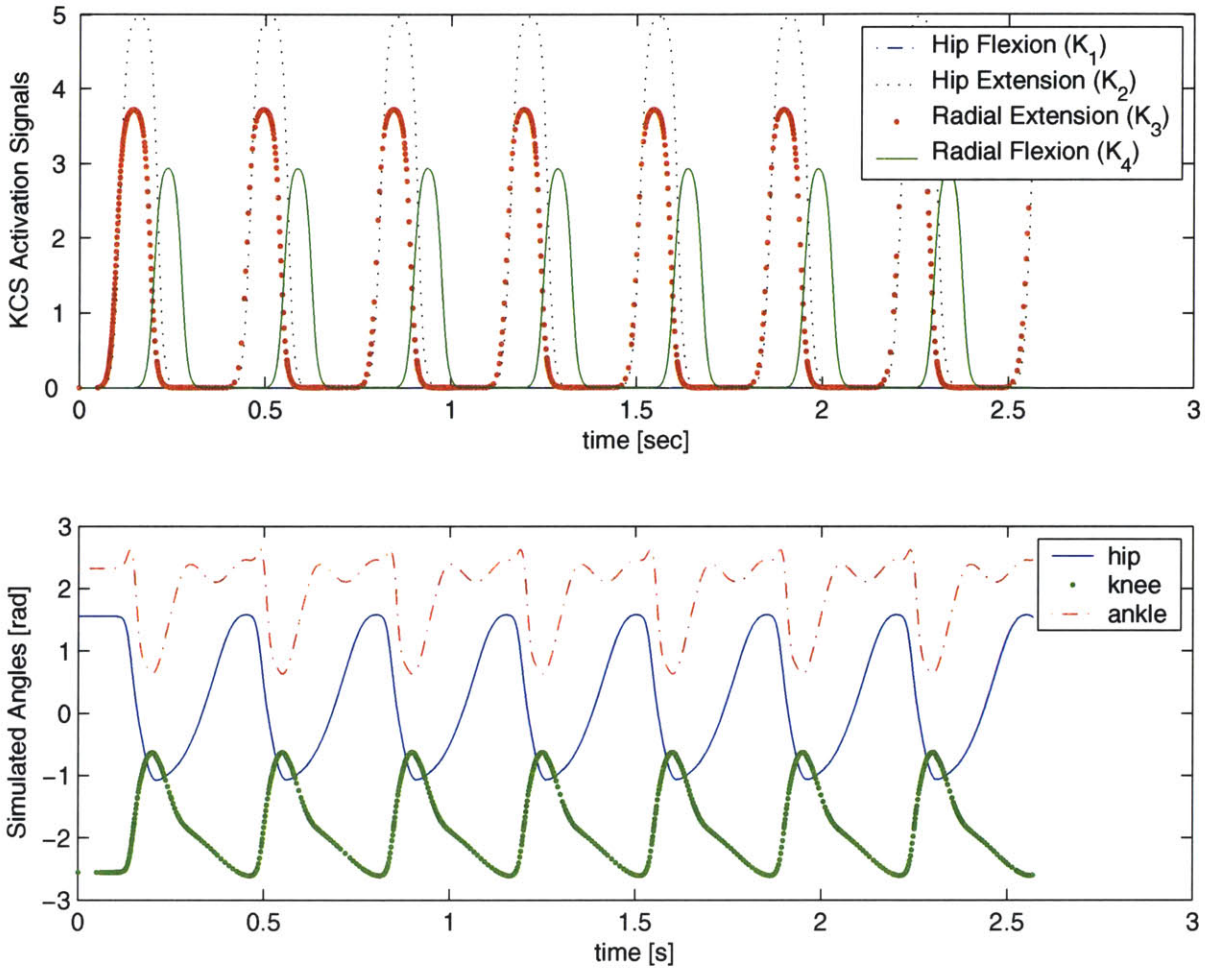

Figure 5-4: Swim Commands

recruitment for certain types of movement such as different types of fibers (fast twitch vs. slow twitch) and varying moment arms that allow certain muscles to operate more optimally than others within some workspace locations.

5.2.2 Swimming Pattern Generation

Having shown that realistic kicks can be reconstructed as simple linear combinations of our derived KCS, we now demonstrate another typical frog behavior, swimming. Figure 5-4 illustrates the control of a swimming pattern by simply toggling the radial extension and hip extension synergies (a small amount of radial flexion is done at the end of the extension phase of the kick). It remains to be seen how accurately

the simulated kinematics describe an actual swimming movement (as well as other common behaviors) in the frog.

5.3 Kinematic Control Synergy Ankle Force Fields

Figure 5-6 shows the ankle force fields resulting from the activation of each of the Kinematic Control Synergies. For the fields presented in Figure 5-6, the nonlinear mapping from EMG to muscle force from Equation (4.3) was used. Using this nonlinear mapping, the KCS force fields are convergent. Also, as seen in Figure 5-6, for increasing levels of activation (*i.e.* increasing $b_i(t)$) the equilibrium point of each of the ankle force fields moves in either the radial or azimuthal directions. As with the synergy force fields computed with Equation 4.3 in Chapter 4, the KCS force fields do not scale linearly with activation ($b_i(t)$) and lack an activation invariant structure. The location of the KCS force field equilibrium points depends on the magnitude of *act*, while the amplitude of the force fields scales as the square of *act* (see Equation 5-6 in Chapter 2.

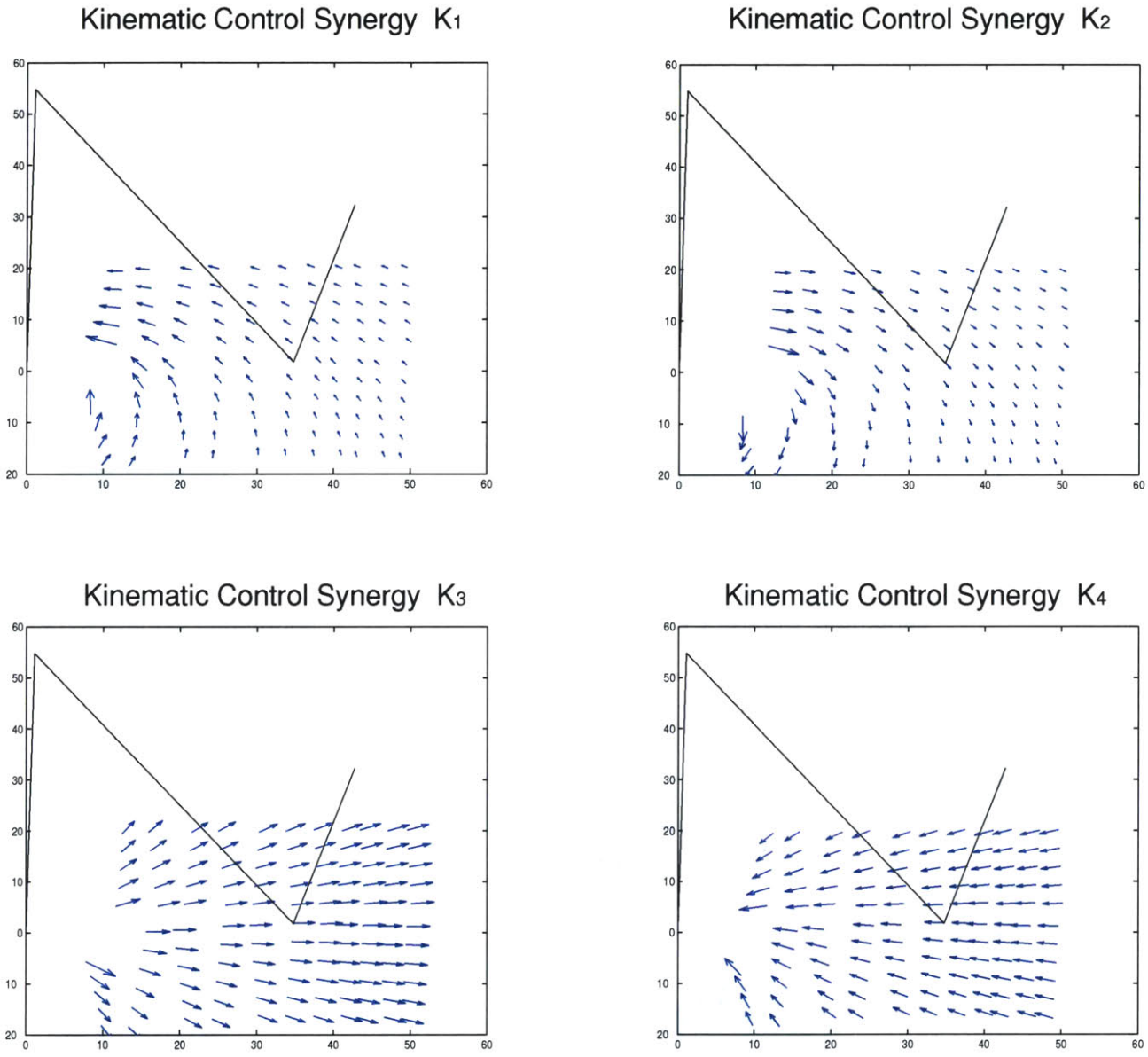

Figure 5-5: Kinematic Control Synergy Ankle Force Fields. Equation 4.3 was used the nonlinear mapping from EMG to muscle force. $b_i(t) = 1$ for each of the force fields shown.

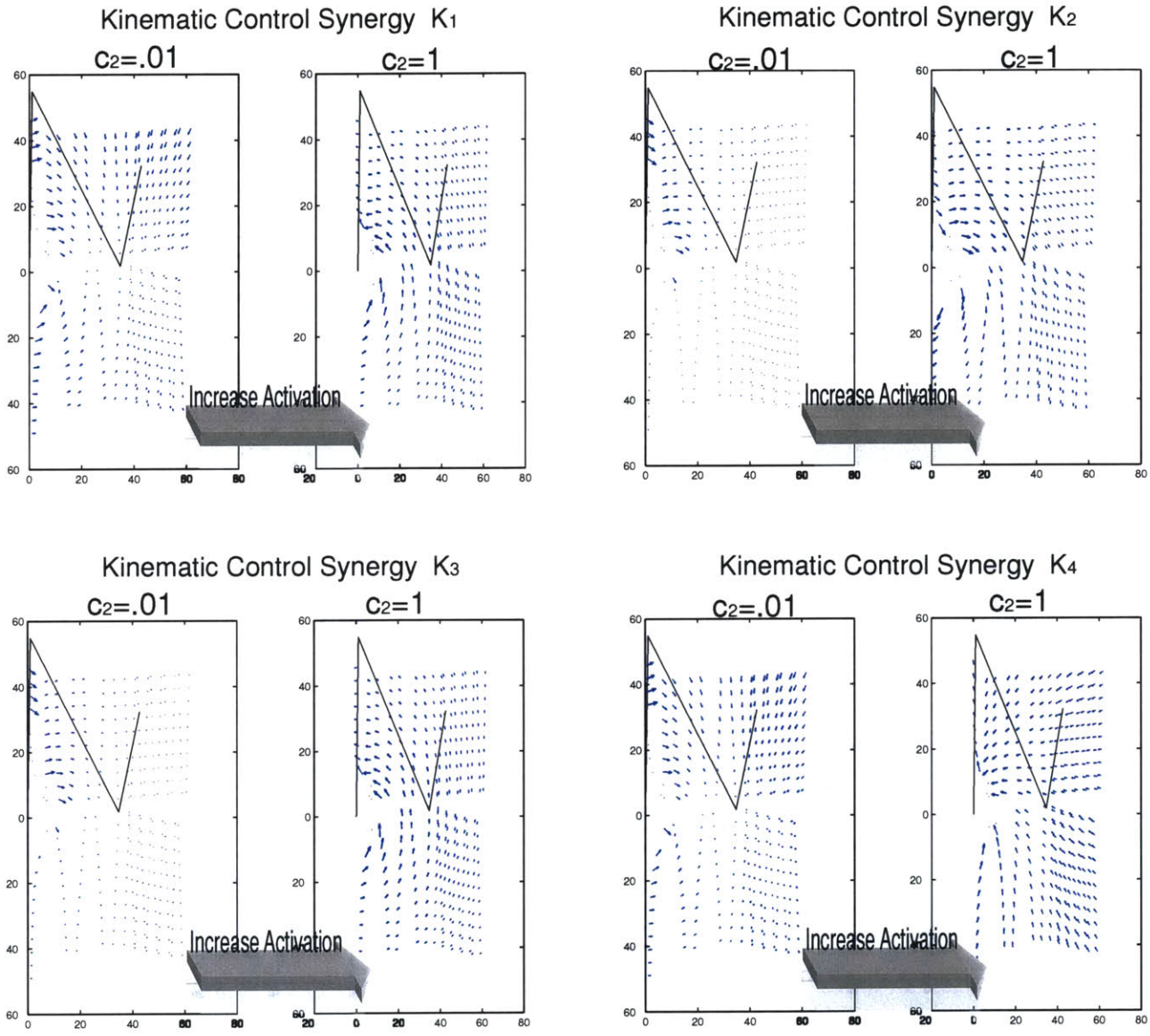

Figure 5-6: Change Kinematic Control Synergy Ankle Force Fields with activation

Chapter 6

Discussion

In this section we present a brief summary of the main results of this thesis. Several important features of the results from Chapters 4 and 5 are then presented, summarized, and their implications explained. Finally, we elaborate on some potential applications of this work and present suggestions for future research.

6.1 Summary of Results

In this thesis we have described a model of the spinal cord/hindlimb system of a bullfrog including the full nonlinear skeletal dynamics, 12 hindlimb muscles, spinal reflexes, and muscle synergies encoded within the spinal cord (Chapter 2). The implemented model was assessed by demonstrating its ability to recreate realistic kinematics when driven with EMG signals recorded from intact bullfrogs (Chapter 4). Additionally, the primitives of Giszter *et al.* and Saltiel *et al.* were discussed and some possible connections considered. In particular, under the assumption that both the synergy and force field experiments stimulated identical spinal sites, the force field primitives associated with each synergy were shown (Chapter 4). It was demonstrated that when the transformation from EMG to muscle force, $\mathbf{\Gamma}'$, was linear: 1) the primitive synergy force fields were shape-invariant with increased activation, and 2) the magnitude of the primitive synergy force vectors increased linearly with activation. However, the synergy force fields showed no fixed position equilibrium,

an observation inconsistent with the findings of Giszter *et al.*. The linearity of $\mathbf{\Gamma}'$ is thus a *sufficient* condition for the ankle force fields to be invariant in shape, although the *necessity* of this condition for force field shape invariance remains to be shown. It was also shown that if $\mathbf{\Gamma}'$ was nonlinear, all of the resulting ankle force fields showed a convergent equilibrium point. However, resulting fields showed neither a fixed position equilibrium nor linear scaling with activation. Because the force fields scaled approximately as the square of the descending activation, it is possible that over a small range of activation the force fields appear to be scaling linearly.

In Chapter 5, it was shown that muscle synergies, $\mathbf{w}_i$, from [36] can be reorganized into a set of Kinematic Control Synergies, $\mathcal{K}_i$, defined as synergistic muscle groups with simple, orthogonal kinematic functions. The reorganization of muscle synergies in this manner allows for the synthesis of a wide range of ranine behaviors from simple pulse-like signals that specify the radial extent and azimuthal angle of the limb. Physiologically, such a formulation is plausible because such simple pulse-like neural activation signals could easily be generated by higher-level CNS structures such as the brainstem or cerebellum. Moreover, reorganization of the muscle synergies into KCS allows for both descending synergy recruitment signals and proprioceptive signals to be encoded with the same limb coordinate frame. Thus KCS allow for a simple mechanism whereby sensory information (such as collision with an obstacle) could be used by spinal interneurons to recruit the muscle groups required to correct the limb's movement (*i.e.* by activating a synergy that moves the limb away from the obstacle) (Chapter 5). To demonstrate the control benefits of the KCS, it was shown that ranine kicks can be recreated quite accurately at both the level of muscle EMG and limb kinematics using linear combinations of the KCS.

6.1.1 Mapping Muscle Synergies to Ankle Force Fields

An important issue addressed in this thesis has been whether the convergent, linearly scaling, and activation invariant ankle force fields observed by Giszter *et al.* could be directly explained in terms of the muscle synergies found by Saltiel *et al.*.

In Chapter 1, it was demonstrated that if Equation (1.6) is found to be true experimentally, then the mapping from muscle EMG to muscle force, $\mathbf{\Gamma}'$, must necessarily be linear. Under this supposition of linearity, it was then demonstrated in Chapter 4 that the resulting ankle force fields were structurally invariant with activation. That is, increasing the level of synergy activation only changed the magnitude of the ankle force field vectors but not their directions. This finding thus implies that the linearity of $\mathbf{\Gamma}'$ is a sufficient condition for the ankle force fields to exhibit the invariant behavior with activation observed by Giszter *et al.*. At this time, however, it cannot be shown whether linearity of $\mathbf{\Gamma}'$ is also a necessary condition for ankle force field invariance.

In order to demonstrate the necessity of this condition, one would need to show that there exists no nonlinear transformation from EMG to muscle force such that the resulting ankle force fields are invariant. A demonstration that requires testing *all* nonlinear transformations from EMG to muscle force before the conclusion can be reached. Alternatively, it could be demonstrated that force field shape invariance with activation implies that the mapping between EMG and force is linear. At this time, neither of these conditions could be shown. In fact, it is quite likely that neither of them can be shown, since the mapping from muscle EMG to muscle force is quite nonlinear as discussed in Chapter 2. But how then are activation invariant ankle force fields achieved? One possibility is that the nervous system has found a (or *the*) nonlinear mapping from EMG to muscle force that preserves the structure of the ankle force fields as spinal activations are varied.

Already it has been demonstrated in Chapter 4, that when the nonlinear contractile element force equation is used as the mapping from EMG to muscle force, the resulting ankle force fields change orientation with increasing activation. However, the resulting fields now show a convergent equilibrium point and linearity of force field scaling may be observed over a small range of muscle activations.

Together, these findings suggest a number of possibilities for how the invariant ankle force fields are achieved. First, it is possible that our muscle model is not

sufficiently accurate and that when these simulations are repeated with the full Hill muscle model as the mapping from EMG to muscle force, the ankle force fields that arise are in fact invariant with activation. This would imply that the muscles are built in such a manner that ankle field invariance arises simply from their structure.

Second, it is possible that additional spinal networks (not captured by synergy extraction method) are actually actively compensating for the changing orientation of the ankle force fields, by either recruiting individual muscles or muscle synergies in such a manner that the end result is an invariant ankle force field. If this is the case, however, it is quite surprising that invariant force fields were observed in deafferented preparations [13]. One possibility is that active feedback from Renshaw cells (or other cells that receive efferent motor commands) is being used to preserve the invariant force field structures. Such cells would remain intact even after deafferentation. Renshaw cells have already been implicated by Bullock and Grossberg [3] as implementing spinal circuits which factor the specification of muscle force and muscle length. Therefore, future work should focus on modelling the function of the Reshaw cells within the spinal cord/hindlimb system.

Last, it is possible that the spinal sites stimulated in the experiments of Giszter *et al.* actually stimulated neuronal networks that restricted the levels by which muscle synergies were activated. If the levels of synergy activation are restricted enough by these networks, it is possible that the resulting net change in the ankle force field orientations may have been interpreted as experimental variability in the data rather than an actual change in the force field orientation. At this moment, the exact mechanism leading to the activation invariance of ankle force fields cannot be determined.

6.1.2 Identifying the Source of Ankle Force Field Convergence

By contrasting the equations used as the linear and nonlinear mappings from EMG to force (Equations (4.4) and (4.3) respectively), it can be hypothesized that convergent force fields arise as a result of the activation dependent muscle rest length term: $\lfloor C_{atl}act - (l_o - l)\rfloor_+ = \lfloor (l - (l_o - C_{atl}act))\rfloor_+$. At a given level of act the equilibrium length of the muscle is given by

$$l_{eq} = l_o - C_{atl}act \tag{6.1}$$

Any displacements of the hindlimb from the equilibrium workspace position implied by the activation of several muscles would then cause a restoring force in the direction of this activation dependance equilibrium point. In light of this observation, it is not surprising that CFFs were observed by Giszter *et al.* in both afferented and deafferented preparations.

6.1.3 Possible Interpretation of Activation Invariant, Linearly Scaling, Fixed Equilibrium Ankle Force Fields

Another interesting property of the force fields characterized by Giszter *et al.* [13], Mussa-Ivaldi *et al.* [24], and Lemay *et al.* [31] was that a large number of the active force fields found had the following properties: 1) They were linearly scalable with activation, 2) showed a fixed position equilibrium within the workspace, and 3) were invariant in shape with activation. Contrary to experimental findings, the force fields predicted by our model show: 1) a nonlinear (squared) force magnitude scaling with activation, 2)an activation dependant equilibrium point, and 3) a variation in shape with activation. The following section attempts to reconcile some of our findings with the known experimental observations.

In regards to the linear scaling of ankle force fields with activation observed by Lemay *et al.*, our results suggest two possible interpretations. First, it is possible

that ankle force fields do not scale linearly with activation. Instead, due to the low activation range tested in [31], it is possible that the scaling *appeared* to be linear. Since within our model, the scaling relation goes as the square of the activation, over a small range of activations ankle forces would indeed appear to scale in a linear fashion. Alternatively, it is possible that spinal interneuronal networks (not modelled here) make the transformation from spinal activation to muscle force a linear function even though the transformation from muscle force to EMG is nonlinear.

In regards to the last two observations, there exists the exciting possibility that activation dependant force fields with activation dependant shapes are functionally equivalent to the static, activation invariant force fields observed by Giszter *et al.*. In the formulation of Giszter *et al.*, a set of static activation invariant force fields are located at different sites of the workspace and ankle movement results from the recruitment of these by the coefficients $c_i(t)$. The resulting force field at the ankle is then the vector sum of the scaled position invariant force fields and will have a convergent equilibrium point somewhere in the middle of the primitive force fields.

In our model, however, the KCS force fields have an activation dependant equilibrium position which starts at the limbs passive equilibrium and moves in the direction which the KCS controls. As activation increases, the shape of the individual KCS force fields changes such that the limb is drawn in the particular direction specified by $b_i(t)$. In the limiting case that only one $b_i(t)$ is stimulated to maximum (and all others are zero) the limb will be drawn towards one particular workspace direction. As illustrated in Figure 6-1, the KCS force field at this location, Φ_i, will be convergent. When the $b_i(t)$ are activated in unison, the limbs equilibrium point will be drawn to a location between the activated Φ_i. Therefore, by defining the KCS force fields at their maximum activation values, they become "position-invariant" convergent force fields like the active force fields of Giszter *et al.*. Further theoretical studies must be performed in order to fully verify the functional relationship presented here between the KCS force fields and those observed by Giszter *et al.*, Mussa-Ivaldi *et al.*, and

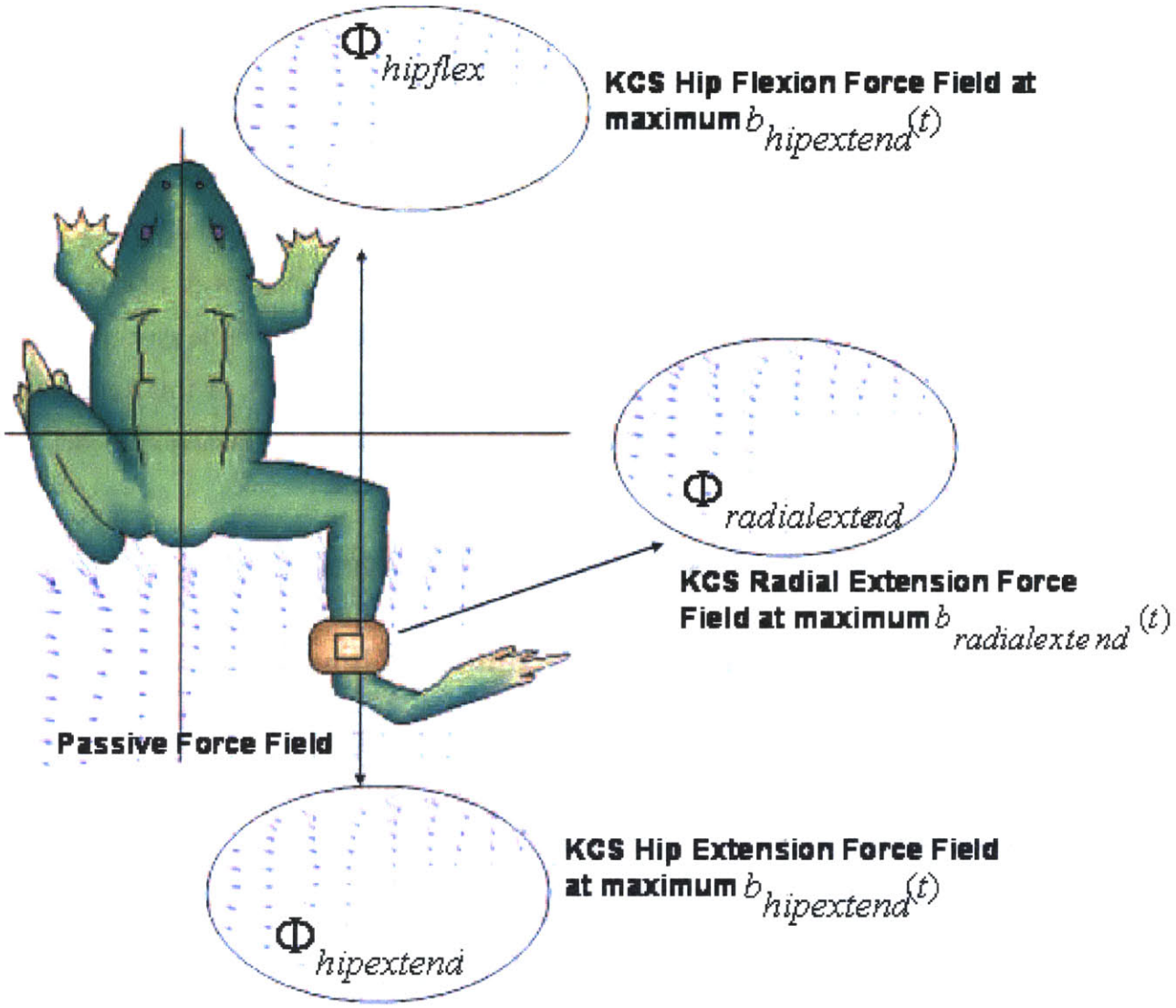

Figure 6-1: Position Invariant and Convergent Force Fields result when the KCS Force Fields are defined as the field arising from their maximum activation. Note that the radial flexion force field is not shown since it would be located under the body of the frog. The arrows indicate the direction of limb movement as each Φ_i is increasingly activated.

Lemay *et al.*and determine if both concepts are indeed equivalent interpretations of the same experimentally observed phenomena.

6.1.4 Muscle Synergies Lack Cocontractive Effects

Along with yielding a reorganization of muscle synergies into Kinematic Control Synergies, the optimization algorithm in Chapter 5 allowed us to conclude that there is no combination of the muscle synergies, w_i, that leads to the production of muscle EMG and no net limb movement. This finding suggests that the ability to actively cocontract at a joint is not encoded within the muscle synergies of Saltiel *et al.*. Therefore, either the frog is unable to cocontract at a joint (if muscle synergies summarize all of the net behaviors that the frog is able to produce), or this finding is a direct result of the the experimental protocol used for synergy extraction in [36].

6.2 Possible Research Implications

6.2.1 Structure of Spinal Locomotor Generators

The physiological decomposition of the muscle synergies encoded within the spinal cord into groups of control synergies has strong implications for the structure of spinal locomotor generators. As was noted from Figure 5-4, control synergies allow for rhythmic locomotor patterns to be generated using a simple set of pulses. Pulses such as these could represent the net activity of a population of neurons in the spinal cord, with the amplitude corresponding to the number of active neurons, and the duration to the length of time the majority of the neuron pool is active. In this manner, a variety of rhythmic locomotor behaviors may be encoded by simple reverberatory circuits within the cord.

6.2.2 Implications for Understanding Human Spinal Injury

The absence of the corticospinal tract in frogs presents the interesting possibility that the entire behavioral repertoire of the frog might be summarized by our sim-

ple set of control synergies. That is, since higher-level CNS structures lack a direct pathway to the $\alpha - motorneuron$ pool, it is most likely that these structures synthesize movement through direct interaction with muscle synergies encoded within the cord. Therefore, since our control synergies represent a reorganization of the muscle synergies identified by Saltiel *et al.* into orthogonal kinematic groups in workspace coordinates, they represent an efficient way in which a large set of behaviors may be constructed. It still remains to be determined whether the EMG and kinematic predicted by using KCS for movement formation corresponds to the actual EMG signals generated in vivo during similar tasks.

In the big picture, our work also suggests the tantalizing possibility that mammalian spinal cord functions like the frogs' but has added input "ports" for descending commands from the cortex. The absence of the corticospinal tract in the frog might also suggest that our model may fairly accurately describe humans who have suffered corticospinal tract injury.

6.2.3 Implications of a Muscle Synergies on the Neural Coordination of Movement

From a control standpoint, the existence of only a small number of muscular synergies and the observed linearity of the spinal/musculoskeletal system may have important implications for neural circuitry required to coordinate movement [40]. The ability to control muscles as groups or synergies, rather than individually, affords the possibility of reducing the number of effective degrees of freedom of the musculoskeletal system. Equation (1.10) illustrates how the effective number of hindlimb degrees of freedom is reduced from 12 (no. of muscles) to 7 (no. of synergies). In Chapter 5, we demonstrate how this number can be further decreased to 4, by introducing a notion Kinematic Control Synergies (KCS), muscle synergies with orthogonal kinematic effects.

Equation (1.10) also has a direct implication to how supraspinal circuits might form movements. Suppose, for example, that it was the goal of the CNS to generate a particular endpoint force, $\mathbf{F}_p(x, y, t)$, using only the muscle synergies, $\mathbf{w}_i$, encoded within the spinal cord. An equivalent control problem is to find the input, $\mathbf{c}(t)$, such that the product $\mathbf{\Phi}(x, y)\mathbf{c}(t)$ comes as close to $\mathbf{F}_p(x, y, t)$ as possible. Because $\mathbf{\Phi}(x, y)$ as derived above is a 2×7 matrix, there are in general either no solutions or an infinite number of them if the input $\mathbf{c}(t)$ is unconstrained. Therefore, if solutions exist, the CNS must be (in some sense) invoking an addition criteria to select the control vector $\mathbf{c}(t)$. Although the control vector, $\mathbf{c}(t)$, is already constrained to contain nonnegative components, an infinite number of solutions may still exist. As a consequence of Equation (1.10), supraspinal circuits could form movements (*i.e.* find $\mathbf{c}(t)$) by projecting the desired control variable (endpoint force, joint torques, *etc.*), $\mathbf{F}_p(x, y, t)$, into the space of controllable directions $\mathbf{\Phi}(x, y)$, and choosing from the solutions, if any, subject to some constraint criterion.

Along with the benefit of reduced dimensionality, however, the existence of spinal synergies might also constrain the range of possible movements that can be synthesized at the spinal level. That is, if all movements were produced by the linear combination of spinal synergies, all possible movements must also lie in the subspace spanned by the synergies. Thus, if supraspinal structures could only synthesize movement via the combination of these synergies, there may be types of movements that simply cannot be achieved as described above. However, a control strategy where supraspinal circuits synthesize movement by finding the combination of spinal synergies that comes closest to the desired movement, $\mathbf{c}(t)$, and supraspinal structures independently control muscles around this "spinal trajectory", might yield a significant simplification to the role of supraspinal structures in limb control.

6.3 Future Research

This works suggests a number of possibilities for future research. First, because the available kinematic data was focused to kicking trials in the horizontal plane, we are only able to compare the simulated EMGs for kicking behaviors. If other sets of kinematic task data were available, a more comprehensive evaluation of the models' ability to generate both realistic EMG and kinematics could be carried out. It would also be of interest to record kinematic data from deafferented preparations so that the role of the beta system in the the synthesis of movement can be better understood. Specifically, due to the lack of knowledge on the function of the beta system, our model treated the beta system as functionally identical to the gamma system under alpha-gamma coactivation. Detailed studies on the function of the beta system are therefore required in order validate or invalidate this assumption.

As illustrated in Chapter 1, if Equation (1.6) can be shown to hold true experimentally, then necessarily the mapping from EMG to muscle force must be linear and as a consequence, the ankle force fields arising from synergy recruitment will be activation invariant. Otherwise, as explained in Section 6.1.1, there are a number of scenarios that need to be considered in order to determine the mechanism whereby ankle force fields are made activation invariant.

Lastly, our findings demonstrate that a wide range of movements can be synthesized as linear combinations of muscle synergies or KCS. Additionally, our findings suggest that movement formation as linear combinations of KCS may be equivalent to linear combinations of position invariant, convergent ankle force fields hypothesized by Giszter *et al.*. Future work should be directed toward demonstrating if both formulation for movement formation are indeed equivalent.

Appendix A

Limb Parameter Estimates

A.1 Limb Physical Parameters

In order to estimate the link masses and lengths for the bullfrog from data published [28] for the *Rana Pipiens*, we make a simple physical scaling argument. First, we assume that the mass of individual segments scales linearly with the size, *i.e.*

$$m_{bf,i} = m_{rp,i}\frac{m_{bf}}{m_{rp}} \tag{A.1}$$

where $m_{bf,i}$ is the mass of the ith link of bullfrog, $m_{rp,i}$ is the mass of the ith link of the *Rana Pipiens*, m_{bf} is the total mass of the bullfrog ($\sim 240 grams$), and m_{rp} is the total mass of the *Rana Pipiens* ($\sim 28 grams$).

Next, in order to estimate the link lengths for the bullfrog, we note that $mass \sim Volume \sim (length)^3$. Therefore, we obtain the relation that

$$l_{bf,i} = l_{rp,i} \cdot (\frac{m_{bf}}{m_{rp}})^{\frac{1}{3}} \tag{A.2}$$

where $l_{bf,i}$ is the length of the bullfrog's ith link, $l_{rp,i}$ is the length of the*Rana Pipiens'* ith link, m_{bf} is the total mass of the bullfrog, and m_{rp} is the total mass of the *Rana Pipiens*. Tables A.1 and A.2 summarize the link masses, lengths, and inertias as computed with Equations (A.1), (A.2), and (2.1).

	Length $[cm]$	Mass $[grams]$	I_z $[grams \cdot cm^2]$
Femur	2.68	2	2.3
Tibia/Tibiofibula	3.07	1.4	1.4
Tibiale/Fibulare	1.54	.4	.2

Table A.1: *Rana Pipiens* physical parameter data obtained from [28]

	Length $[cm]$	Mass $[grams]$	I_z $[grams \cdot cm^2]$
Femur	5.48	17.1	42.9
Tibia/Tibiofibula	6.28	12.0	39.4
Tibiale/Fibulare	3.15	3.40	2.8

Table A.2: Bullfrog physical parameter data estimated from Equations (A.1), (A.2), and (2.1).

Appendix B

Skeletal Dynamics - Equations of Motion

Note: This section closely follows the notation of Chapter 6 in [39]. The interested reader is referred to this text for a more complete treatise of rigid body mechanics.

In this section we present the derivation of the equations of motion (EOM) for a three-link rigid body with revolute (rotary) joints as shown in Figure B-1. For completeness and validation purposes we assume the rigid body is in the vertical plane and include the effects of gravity. The EOM in the horizontal plane can then be obtained by setting gravity to zero.

B.1 Lagrangian Method in Analytical Mechanics

A variety of systematic methods exist in analytical mechanics for deriving the EOM for arbitrary open-kinematic chains of rigid bodies. As with most things in engineering, the particular application determines which type of method is the most appropriate or conceptually simplest to apply. For the particular configuration in Figure B-1 we use the Lagrangian formulation.

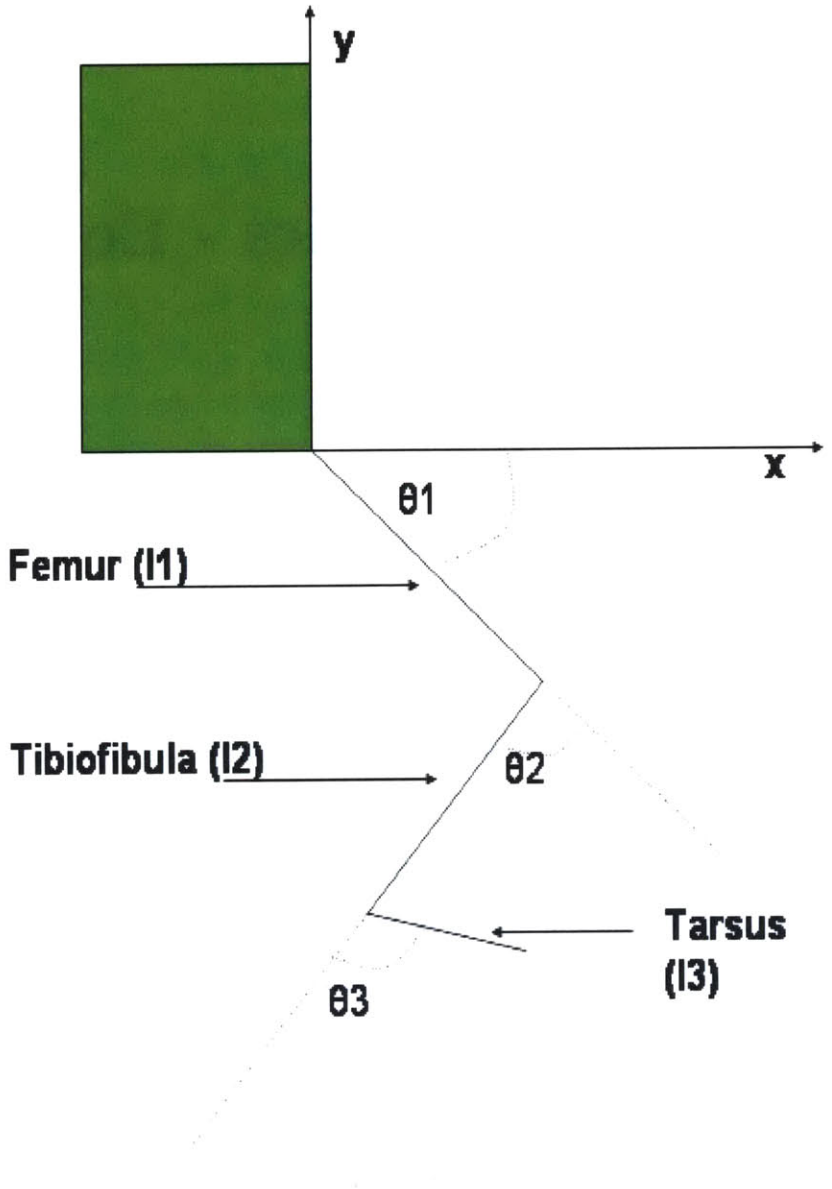

Figure B-1: Hindlimb reference diagram for derivation of equations of motion

The Lagrangian method consists of writing down the system's Lagrangian, L, in terms of the generalized coordinate vector, $\mathbf{q} = [\theta_1, \theta_2, \theta_2]^\top$, and the generalized velocity vector, $\dot{\mathbf{q}}$. The general form of the system's Lagrangian is

$$L(\mathbf{q}, \dot{\mathbf{q}}) = K(\mathbf{q}, \dot{\mathbf{q}}) - V(\mathbf{q}) \tag{B.1}$$

where K is the kinetic energy of the system and V is the potential energy. Once the Lagrangian has been obtained, the equations of motion of the system are then found by application of the Euler-Lagrange equations defined as

$$\frac{d}{dt}\frac{\partial L}{\partial \dot{q}_i} - \frac{\partial L}{\partial q_i} = \tau_i \tag{B.2}$$

where q_i is the ith component of the generalized coordinate vector and τ_i is the generalized torque acting about the ith joint. Our task is then reduced to finding expressions of the system's kinetic and potential energies in terms of the generalized coordinates and velocities.

B.2 Kinetic Energy

Let us denote the radius vectors from the origin of the inertial frame to the center of mass of each of the links by r_{ci} where $i = 1, 2, 3$, *i.e.*

$$\begin{aligned}
\mathbf{r}_{c1} &= \begin{bmatrix} 1/2\, l_1\, c_1 \\ 1/2\, l_1\, s_1 \\ 0 \end{bmatrix} \\
\mathbf{r}_{c2} &= \begin{bmatrix} l_1\, c_1 + 1/2\, l_2\, c_{12} \\ l_1\, s_1 + 1/2\, l_2\, s_{12} \\ 0 \end{bmatrix} \\
\mathbf{r}_{c3} &= \begin{bmatrix} l_1\, c_1 + l_2\, c_{12} + 1/2\, l_3\, c_{123} \\ l_1\, s_1 + l_2\, s_{12} + 1/2\, l_3\, s_{123} \\ 0 \end{bmatrix}
\end{aligned} \tag{B.3}$$

where

$$c_{ijk} = \cos(\sum_{n=i}^{k} \theta_n) \tag{B.4}$$
$$s_{ijk} = \sin(\sum_{n=i}^{k} \theta_n)$$

Next, let us define the jacobian, $J_{v_{ci}}$, of each of the r_{ci} (i=1,2,3) with respect to the generalized coordinate vector $\mathbf{q}$.

$$\mathbf{J}_{v_{c1}} = \begin{bmatrix} -1/2\, l_1\, s_1 & 0 & 0 \\ 1/2\, l_1\, c_1 & 0 & 0 \\ 0 & 0 & 0 \end{bmatrix} \tag{B.5}$$

$$\mathbf{J}_{v_{c2}} = \begin{bmatrix} -l_1\, s_1 - 1/2\, l_2\, s_{12} & -1/2\, l_2\, s_{12} & 0 \\ l_1\, c_1 + 1/2\, l_2\, c_{12} & 1/2\, l_2\, c_{12} & 0 \\ 0 & 0 & 0 \end{bmatrix}$$

$$\mathbf{J}_{v_{c3}} = \begin{bmatrix} -l_1\, s_1 - l_2\, s_{12} - 1/2\, l_3\, s_{123} & -l_2\, s_{12} - 1/2\, l_3\, s_{123} & -1/2\, l_3\, s_{123} \\ l_1\, c_1 + l_2\, c_{12} + 1/2\, l_3\, c_{123} & l_2\, c_{12} + 1/2\, l_3\, c_{123} & 1/2\, l_3\, c_{123} \\ 0 & 0 & 0 \end{bmatrix}$$

The velocity of the center of mass of the ith link, v_{ci}, is then

$$\mathbf{v}_{ci} = \mathbf{J}_{v_{ci}} \dot{\mathbf{q}} \tag{B.6}$$

Hence the translational part of the kinetic energy is

$$K_{trans} = \frac{1}{2} m_1 \mathbf{v}_{c1}^{\top} \mathbf{v}_{c1} + \frac{1}{2} m_2 \mathbf{v}_{c2}^{\top} \mathbf{v}_{c2} + \frac{1}{2} m_3 \mathbf{v}_{c3}^{\top} \mathbf{v}_{c3} \tag{B.7}$$

$$K_{trans} = \frac{1}{2} \dot{\mathbf{q}}^{\top} \{ m_1 \mathbf{J}_{v_{c1}}^{\top} \mathbf{J}_{v_{c1}} + m_2 \mathbf{J}_{v_{c2}}^{\top} \mathbf{J}_{v_{c2}} + m_3 \mathbf{J}_{v_{c3}}^{\top} \mathbf{J}_{v_{c3}} \} \dot{\mathbf{q}} \tag{B.8}$$

We deal next with the rotational kinetic energy of the system. First, because of the particular arrangement of links, it is clear that the angular velocity, ω_i, of each

of the links about their center of masses are

$$\begin{aligned} \omega_1 &= [0 \quad 0 \quad \dot{q}_1]^\top \\ \omega_2 &= [0 \quad 0 \quad \dot{q}_1 + \dot{q}_2]^\top \\ \omega_3 &= [0 \quad 0 \quad \dot{q}_1 + \dot{q}_2 + \dot{q}_3]^\top \end{aligned} \tag{B.9}$$

Moreover, since ω_i is aligned with the z-axis, the triple product $\omega_i^\top I_i \omega_i$ reduces to $(I_{3,3})_i$ times the square of the magnitude of the angular velocity. The quantity $(I_{3,3})_i$ is the inertia of the ith link about an axis located at the center of mass and pointing out of the page in Figure B-1. Since only one moment of inertia is relevant to the rotational energy expression, we shall refer to $(I_{3,3})_i$ as I_i. The rotational kinetic energy of the overall system is then

$$K_{rot} = \frac{1}{2}\dot{\mathbf{q}}^\top \{ I_1 \begin{pmatrix} 1 & 0 & 0 \\ 0 & 0 & 0 \\ 0 & 0 & 0 \end{pmatrix} + I_2 \begin{pmatrix} 1 & 1 & 0 \\ 1 & 1 & 0 \\ 0 & 0 & 0 \end{pmatrix} + I_3 \begin{pmatrix} 1 & 1 & 1 \\ 1 & 1 & 1 \\ 1 & 1 & 1 \end{pmatrix} \} \dot{\mathbf{q}} \tag{B.10}$$

The total kinetic energy of the system is then simply

$$K_{total} = K_{tran} + K_{rot} \tag{B.11}$$

$$K_{total} = \frac{1}{2}\dot{\mathbf{q}}^\top \{ m_1 \mathbf{J}_{v_{c1}}^\top \mathbf{J}_{v_{c1}} + m_2 \mathbf{J}_{v_{c2}}^\top \mathbf{J}_{v_{c2}} + m_3 \mathbf{J}_{v_{c3}}^\top \mathbf{J}_{v_{c3}} + \begin{pmatrix} I_1 + I_2 + I_3 & I_2 + I_3 & I_3 \\ I_2 + I_3 & I_2 + I_3 & I_3 \\ I_3 & I_3 & I_3 \end{pmatrix} \} \dot{\mathbf{q}}$$

$$K_{total} = \frac{1}{2}\dot{\mathbf{q}}^\top \mathbf{H}(\mathbf{q}) \mathbf{q} \tag{B.12}$$

where the matrix $\mathbf{H}(\mathbf{q})$ is referred to as the system inertia matrix.

B.3 Potential Energy

The expression for the potential energy is simply the sum of the potential energies of each of the individual links, *i.e.* the mass of each link multiplied by the gravitational acceleration and the height of its center of mass. Thus

$$V = m_1 g\frac{l_1 s_1}{2} + m_2 g\{l_1 s_1 + \frac{l_2 s_{12}}{2}\} + m_3 g\{l_1 s_1 + l_2 s_{12} + \frac{l_3 s_{123}}{2}\} \tag{B.13}$$

B.4 Equations of Motion

With expressions for the kinetic and potential energies of the system obtained, the EOMs can be derived by applying the Euler-Lagrange equations to the Lagrangian according to Equation (B.2). The resulting equations can be written in matrix form as

$$\mathbf{H}(\mathbf{q})\ddot{\mathbf{q}} + \mathbf{C}(\mathbf{q}, \dot{\mathbf{q}})\dot{\mathbf{q}} + \mathbf{g}(\mathbf{q}) = \tau \tag{B.14}$$

where $\mathbf{H}$ is the system inertia matrix (as defined in Equation (B.12)), $\mathbf{C}$ is the matrix consisting of the Corioli and centrifugal terms, and $\mathbf{g}(\mathbf{q})$ consists of the terms arising from differentiation of the potential energy. There is a direct relation between the elements of the $\mathbf{H}$ and $\mathbf{C}$ matrices as demonstrated in [39]. The k, j-th element of the $\mathbf{C}$ matrix is defined as

$$c_{kj} = \sum_{i=1}^{3} \frac{1}{2}\{\frac{\partial h_{kj}}{\partial \dot{q}_i} + \frac{\partial h_{ki}}{\partial \dot{q}_j} - \frac{\partial h_{ij}}{\partial \dot{q}_k}\} \tag{B.15}$$

This relation between the $\mathbf{C}$ and $\mathbf{H}$ matrices presents an alternative method whereby the EOMs may be derived once Equations (B.12) and (B.13) were obtained.

Bibliography

[1] BIZZI, E., TRESCH, M.C., SALTIEL, P., D'AVELLA, A. New Perspectives on Spinal Motor Systems *Nature Reviews — Neuroscience* 1:101-108, 2000.

[2] BROWN, I.E., SCOTT, S.H., LOEB, G.E., Mechanics of feline soleus: II Design and validation of a mathematical model, *Journal of Muscle Research and Cell Motility* Vol. 17:221-233, 1995

[3] BULLUCK, D., GROSSBERG, S. Spinal Network Computation Enable Independent Control of Muscle Length and Joint Compliance, *Advanced Neural Computers* 349:356, 1990

[4] BULLOCK, D., GROSSBERG, S., GUENTHER, F.H. A Self-Organizing Neural Model of Motor Equivalent Reaching and Tool Use by a Multijoint Arm *J Cognitive Neuroscience* 4:408-435, 1993.

[5] CHENG, E., BROWN, I., LOEB, J., Virtual Muscle 3.1.5: Muscle Model For Matlab User's Manual, *The Alfred E. Mann Institute*, 2001

[6] CRAGO, P. E., MEMBERG, W. D., USEY, M. K., KEITH, M. W., KIRSCH, R. F., CHAPMAN, G. J., KATORGI, M. A., PERREAULT, E. J., An Elbow Extension Neuroprosthesis for Individuals with Tetraplegia *IEEE Transactions on Neural Systems and Rehabilitation Engineering* Vol. 6, 1:1-6,1998

[7] D'AVELLA, A., BIZZI, E. Low dimensionality of supraspinally induced force fields *National Academy of Sciences* 95:7711-7714, 1998.

[8] D'AVELLA, A., SALTIEL, P., BIZZI, E., Combinations of muscle synergies in the construction of a natural motor behavior *Nature Neuroscience* Vol. 6, 3:300-308,2003

[9] FIELD, E.C., STEIN, P.S.G. Spinal Cord coordination of hindlimb movements in the turtle: intralimb temporal relationships during scratching and swimming *J Neurophysiology* 78:1394-1403, 1997.

[10] FUGLEVAND, A.J., MACEFIELD, V.G., BIGLAND-RITCHIE, B., Force-Frequency and Fatigue Properties of Motor Units in Muscles That Control Digits of the Human Hand, *Journal of Neurophysiology* 81: 1718-1729, 1999

[11] FUGLEVAND, A.J., ZACKOWSKI, K.M., HUEY, K.A., ENOKA, R.M., Impairment of neuromuscular propagation during human fatiguing contractions at submaximal forces, *Journal of Physiology* 460: 549-572, 1993

[12] GALAGAN, J.E., LEMAY, M.A., LOEB, E.P., BIZZI, E. EMG activity during vector summation of spinal force field primitives *27th Annual Meeting Soc. Neuroscience, New Orleans, LA* 1997.

[13] GISZTER, S.F., MUSSA-IVALDI, F.A., BIZZI, E. Convergent Force Fields Organized in the Frog's Spinal Cord *J Neuroscience* 2:467-491, 1993.

[14] GUIFFRIDA, J.P., CRAGO, P.E., Reciprocal EMG Control of Elbow Extension by FES *IEEE Transactions on Neural Systems and Rehabilitation Engineering* Vol. 9, 4:338-345, 2001.

[15] GUYTON, A.C., Textbook of Medical Physiology *W.B. Saunders Company* 606-618.

[16] HASAN, Z., A Model of Spindle Afferent Response to Muscle Stretch, *Journal of Neurophysiology* Vol. 49:989-1006, 1983

[17] HERR, H., ¡hherr@ai.mit.edu¿ "RE: Muscle Stiffness/Cross-sectional Area" 20 March 2003. Personal e-mail (20 March 2003).

[18] HILL, A.V., The heat of shortening and the dynamic constants of muscle, *Proceedings of the Royal Society of London (Series B)* 126:136-195, 1938

[19] HOGAN, N., An organizing principle for a class of voluntary movements, *Journal of Neuroscience* 4:2745-2754, 1984

[20] HOGAN, N., The mechanics of multi-joint posture and movement control, *Biological Cybernetics* 52:315-331, 1985

[21] HUXLEY, A.F., Muscle structure and theories of contraction, *Progress in Biophysics and Biophysical Chemistry* 7:255318,1957

[22] MUSSA-IVALDI, F.A. Nonlinear Force Fields: A Distributed System of Control Primitives for Representing and Learning Movement *IEEE Proceedings of CIRA '97* 1997.

[23] MUSSA-IVALDI, F.A., BIZZI, E. Motor learning through the combination of primitives *The Royal Society* 355:1755-1769, 2000.

[24] MUSSA-IVALDI, F.A., GISZTER, S.F., BIZZI, E. Linear combinations of primitives in vertebrate motor control. *Proc. Nat. Acad. Sci.* 91:7534-7538, 1994.

[25] MUSSA-IVALDI, F.A., HOGAN, N., BIZZI, E. Neural, Mechanical, and Geometric Factors Subserving Arm Posture in Humans *J Neuroscience* Vol. 5, 10:2732-2343, 1985.

[26] KANDEL, E. R., SCHWARTZ, J. H., JESSEL, T. M., Principles of Neural Science, *McGraw-Hill*, 2000

[27] KARGO, W.J., GISZTER, S.F. Rapid Correction of Aimed Movements by Summation of Force-Field Primitives *J Neuroscience* 1:409-426, 2000.

[28] KARGO, W.J., NELSON, F., ROME, L.C., Jumping in frogs: assessing the design of the skeletal system by anatomically realistic modeling and forward dynamic simulation *The Journal of Experimental Biology* 205:16831702,2002.

[29] KARGO, W.J., ROME, L.C., Functional morphology of proximal hindlimb muscles in the frog Rana pipiens *The Journal of Experimental Biology* 205:19872004,2002.

[30] KATAYAMA, M., KAWATO, M., Virtual trajectory and stiffness ellipse during multijoint arm movement predicted by neural inverse models, *Biological Cybernetics* Vol. 69: 353-363,1993

[31] LEMAY, M.A., GALAGAN, J.E., HOGAN, N., BIZZI, E. Modulation and Vectorial Summation of the Spinalized Frog's Hindlimb End-Point Force Produced by Intraspinal Electrical Stimulation of the Cord *IEEE Transactions on Neural Systems and Rehabilitation Engineering* 1:12-23, 2001.

[32] LOEB, E.P., GISZTER, S.F., SALTIEL, P., MUSSA-IVALDI, F.A., BIZZI, E. Output units of motor behavior: an experimental and modeling study *J Cognitive Neuroscience* 12:78-97, 2000.

[33] MASSAQUOI, S.G., Introduction to Sensorimotor Neuroengineering Class Notes, Spring 2002

[34] MCMAHON, T.A., Muscles, Reflexes, and Locomotion, *Princeton University Press*, 1984

[35] PERREAULT, E.J., CRAGO, P.E., KIRSCH, R.F., Postural Arm Control Following Cervical Spinal Cord Injury *IEEE Transactions on Neural Systems and Rehabilitation Engineering* Vol. 9, 4:369-377,2001.

[36] SALTIEL, P., WYLER-DUDA, K., D'AVELLA, A., TRESCH, M.C., BIZZI, E. Muscle Synergies Encoded Within the Spinal Cord: Evidence From Focal Intraspinal NMDA Iontophoresis in the Frog *American Physiological Society* 2001.

[37] SALTIEL, P., TRESCH, M.C., BIZZI, E. Spinal cord modular organization and rhythm generation: an NMDA iontophoretic study in the frog *J Neurophysiology* 80:2323-2339, 1998.

[38] SCOTT, S.H., LOEB, G.E., The mechanical properties of the aponeurosis and tendon of the cat soleus muscle during whole-muscle isometric contractions, *Journal of Morphology*, 1995

[39] SPONG, M.W., VIDYASAGAR, M., Robot Dynamics and Control, *John Wiley & Sons, Inc.*, 1989

[40] SOECHTING, J.F., LACQUANITI, F., Am assessment of the existance of muscle synergies during load pertubations and intentional movements of the human arm *Exp. Brain Res* 74:535-548, 1989.

[41] TRESCH, M.C. Discreteness in Spinal Motor Systems in the Rat and Frog *Doctoral Thesis - Massachusetts Institute of Technology* 1997.

[42] TRESCH, M.C., SALTIEL, P., BIZZI, E. The construction of movement by the spinal cord *Nature Neuroscience* 2: 162-167, 1999.

[43] WINTER, D.A., Biomechanics and Motor Control of Human Movement, *Wiley-Interscience Publication* 1990

[44] WINTERS, J.M., CRAGO, P.E., Biomechanics and Neural Control of Posture and Movement, *Springer-Verlag*, 2000

[45] WINTERS, J.M., STARK, L., Muscle Models: What is Gained and What Is Lost by Varying Model Complexity, *Biological Cybernetics*, 1987